NASA Grant #NAG5-9642
National Aeronautics and Space Administration

KINEMATIC, MICROPHYSICAL AND LATENT HEATING ASPECTS OF TWO MESOSCALE CONVECTIVE SYSTEMS OBSERVED DURING TRMM-LBA

by Andrea G. Williams

Colorado State University

DEPARTMENT OF ATMOSPHERIC SCIENCE

PAPER NO. 718

KINEMATIC, MICROPHYSICAL AND LATENT HEATING ASPECTS OF TWO MESOSCALE CONVECTIVE SYSTEMS OBSERVED DURING TRMM-LBA

by

Andrea G. Williams
Department of Atmospheric Science
Colorado State University
Fort Collins, CO 80523

Research Supported by
National Aeronautics & Space Administration
under Grant NAG5-9642

Spring 2002

Atmospheric Science Paper No. 718

COLORADO STATE UNIVERSITY

January 29, 2002

WE HEREBY RECOMMEND THAT THE THESIS PREPARED UNDER OUR SUPERVISION BY ANDREA G. WILLIAMS ENTITLED KINEMATIC, MICROPHYSICAL AND LATENT HEATING ASPECTS OF TWO MESOSCALE CONVECTIVE SYSTEMS OBSERVED DURING TRMM-LBA BE ACCEPTED AS FULFILLING IN PART REQUIREMENTS FOR THE DEGREE OF MASTER OF SCIENCE.

Committee on Graduate Work

Advisor

Department Head

ABSTRACT

KINEMATIC, MICROPHYSICAL AND LATENT HEATING ASPECTS OF TWO MESOSCALE CONVECTIVE SYSTEMS OBSERVED DURING TRMM-LBA

Dual-Doppler and multiparameter radar data were used to study the environmental atmospheric conditions, kinematics, microphysics and latent heating characteristics for two tropical mesoscale convective systems (MCSs) observed in the Amazon during the TRMM-LBA field campaign. Each MCS occurred in a different meteorological regime as classified by the low-level zonal wind direction; 17 February 1999 occurred during a period of easterly wind and 23 February 1999 during a period of westerly wind. The data were objectively partitioned into convective and stratiform components and the water and ice masses were determined via the difference reflectivity method. Temporal changes in these quantities allowed for an observationally based diagnosis of latent heating rates for each case.

Tropospheric parameters such as larger CAPE, drier air aloft and stronger shear likely contributed to the more intense and more organized system of 17 February 1999. This easterly case contained strong updrafts (> 20 m s^{-1}), differential reflectivity columns extending 1-2 km above the freezing level, and some linear depolarization ratio "caps" above those columns indicating active mixed phase regions. Riming occurred in these mixed phase regions when trends in the mean convective vertical velocities approached local maximums. Approximately twice the

amount of total water mass was found in the easterly case compared to the westerly case, in part because there was more convective echo associated with that storm. The westerly case also contained intense convection, strong updrafts (> 15 m s^{-1}), differential reflectivity columns extending slightly above the freezing level, and some weak linear depolarization ratio "caps." Volume total masses involved in riming processes in the westerly case were approximately 75% less than in the easterly case.

The latent heating rates for both case studies were dominated by the condensation term throughout most of their life cycles. Latent heating rates due to deposition (sublimation) for both cases were of similar magnitude during their growth (decline) stages. The heating rates due to freezing, melting and riming were inconsequential as their values were 2-3 orders of magnitude smaller. The convective latent heating rates were positive throughout the troposphere while the systems were mature. The stratiform components had much smaller values and less interpretable signals. However, the deposition sub-component for the westerly case remained positive showing that stratiform processes did heat the troposphere above 6.5 km AGL throughout the event. Bulk profiles of the latent heating rates in degrees day^{-1} per cm day^{-1} yielded maximums between 4-6 km with shapes very similar to several modeling and budget studies that examined Q_1, the apparent heat source term dominated by latent heating.

Andrea G. Williams
Atmospheric Science Department
Colorado State University
Fort Collins, CO 80523
Spring 2002

ACKNOWLEDGEMENTS

I would like to thank Dr. Steven Rutledge for his guidance and encouragement over the last 2 ½ years. Committee members Drs. Christian Kummerow, Derek Lile and Carmen Menoni provided helpful insights to this work. The radar meteorology group at CSU made this work possible via thoughtful discussions, especially with Drs. Robert Cifelli, Larry Carey and Walt Petersen. Sharing ideas with Paul Hein, Margi Cech, Julie Demuth, Sarah Tessendorf, Crystal Pettet, Dan Lindsey and Katie Walters were also very helpful. This research was supported by NASA Grant NAG5-9642 and an American Meteorological Society Fellowship.

TABLE OF CONTENTS

LIST OF TABLES

LIST OF FIGURES

CHAPTER ONE

Introduction

1.1 Motivation

A key objective of the Tropical Rainfall Measuring Mission (TRMM) is to measure tropical rainfall and infer the latent heating released by the convection (Simpson et al., 1988). Tropical convection has been of much interest for several decades as its deep convection drives the global circulation. Riehl and Malkus (1958) discussed how deep cumulonimbus clouds transport high-energy air from the boundary layer in the tropics to the upper troposphere, and therefore effect the global circulation. Hartmann et al. (1984), DeMaria (1985), Gandú and Silva Dias (1998) also discussed these "hot towers" and their substantial impact on the global circulation. In order to more effectively model the global circulation, tropical convection in both the horizontal and vertical must be examined in detail.

The kinematics and microphysics of convective towers have also been studied (Houze, 1982; Houze, 1989; Rogers and Yau, 1989 and others). Houze (1989) describes a conceptual model of a mature tropical mesoscale convective system (MCS) and the interaction between convective and stratiform components. First the drops condense below the freezing level in an updraft region and they grow by condensation and collision-coalescence processes. The precipitation ice is created as those drops are lofted and freeze above the 0° C level. In this so-called mixed phase region (0° to -20° C), the ice can grow by accreting supercooled water (riming), if such water is available, or by deposition. The ice particles too heavy for the updraft to suspend, fall out, melt and become convective rain. The remaining particles continue to grow by riming and deposition, or spread horizontally into stratiform regions of the storm. The stratiform region has moderate (i.e., < 1 m s^{-1}) upward vertical motion above the freezing level and downward below. When the ice enters the aloft portion of the stratiform region, it grows by vapor deposition. Between the temperatures of 0° and -12° C, the particles grow by aggregation to form large snowflakes. Once the aggregates are heavy enough to fall through the moderate updraft and reach the 0° C level, they begin to melt and yield locally high reflectivities that are seen on radar as a bright band signature. Below this point, they melt completely and reach the surface as rain. This process of seeding the stratiform portion with snow from the convective region is very important. Rutledge and Houze (1987), using a 2-D steady state numerical model, could not reproduce significant stratiform rain without including seeding from the convective region. Knowledge of the kinematic and microphysical development of each storm is crucial to understanding the types of hydrometeors present.

The heating in tropical MCSs primarily comes from changes in phase called latent heating (Hartmann et al., 1984; DeMaria, 1985; Houze, 1989; Cifelli et al., 2001). In the convective region of a MCS, liquid water could change phase to ice by a strong updraft taking it to colder conditions in the storm as described above. Heat is released during the phase change at a constant temperature until the water has completely turned to ice. Explicitly, it releases 3.34 x 10^5 J of energy for every kilogram of water that is frozen. Conversely, in the stratiform region, a parcel of ice crystals could fall below the freezing level and begin to melt. This phase change requires heat and hence cools the surrounding air. Houze (1997) noted that these stratiform regions cool the atmosphere at low levels by melting and evaporation, but warm it aloft by vapor diffusional growth. Convective regions of the storm generally heat the environment at all levels (i.e. Fig. 3; Houze, 1997). Table 1.1 shows the specific latent heats for all phase changes involving water. In order to estimate the total latent heating, it is obvious that bulk hydrometeor types and their changes with time must be identified. Depending on the location and length of time the phase change occurred, the appropriate multiplication is done to find the observationally based estimate of the latent heating rate. The relative contributions from various hydrometeor types can become clearer by partitioning the data into convective and stratiform elements.

There have been a number of radar-based experiments in the low latitudes to examine the structure of tropical convection. The GARP Atlantic Tropical Experiment (GATE) was conducted during the summer of 1974. Four C-band shipborne radars among other instrumentation collected data in this tropical oceanic environment in the Atlantic basin (Hudlow, 1979). North of Australia, the Equatorial Monsoon Experiment (EMEX) was conducted to investigate MCSs in the monsoon flow with airborne and ground based Doppler radars, other aircraft instrumentation and an upper-air sounding network (Webster and Houze, 1991). The Down Under Doppler and Electricity Experiment (DUNDEE) used two 5-centimeter Doppler radars and a wind profiler to examine the wind structure of the convection near

Darwin, Australia (Rutledge et al., 1992; Cifelli and Rutledge, 1994). The Amazon Boundary Layer Experiment (ABLE) used one non-coherent X-band radar, mesonet stations, rawinsondes and satellite data in the Amazon basin to study Amazon coastal squall lines (Greco et al., 1994). TOGA-COARE took ship-borne measurement of convection over the warm pool in the western Pacific with two C-Band Doppler Radars and aircraft instrumentation (Petersen et al., 1999). None of these studies utilized instrumentation with polarimetric capabilities.

Two studies in the tropics have used polarimetric radars to study oceanic and continental convection. The Maritime Continent Thunderstorm Experiment (MCTEX) studied life cycles of storms over the Tiwi Islands near Austrailia in 1995 using the Bureau of Meteorology Research Centre (BMRC) C-band (5.33 cm) dual-polarimetric radar, C-Pol (Keenan et al., 1994). The South China Sea Monsoon Experiment (SCSMEX) also used C-Pol, but had the added advantage of a second C-band Doppler radar. These instruments, among many others, were used to study the key physical processes for the beginning and evolution of the summer monsoon in Southeast Asia (Lau et al., 2000).

1.2 TRMM-LBA Overview

The Tropical Rainfall Measuring Mission-Large Scale Biosphere-Atmosphere Experiment (TRMM-LBA) field campaign was conducted in southwestern portions of the Amazon from 10 January 1999 to 28 February 1999 (Rutledge et al., 1998). The LBA portion of TRMM was one of several ground validation experiments. This field campaign offered a suite of instruments, including both remote and in situ sensors. The National Aeronautics and Space Administration (NASA) Tropical Oceans Global Atmosphere (TOGA) C-band radar and the National Center for Atmospheric Research (NCAR) S-Pol S-band radar were deployed in the state of Rondônia in Northern Brazil. The S-Pol radar has polarimetric capabilities and can therefore give more insight into the hydrometeors' shape, size, orientation, and thermodynamic phase of hydrometeors in a bulk sense. Other instrumentation not specifically used in this study included a dual-wavelength profiler, a rain gauge and disdrometer network, sounding network and lightning detection equipment. Figure 1.1 shows the locations of the previously described instrumentation. Two aircraft also flew during the campaign sampling the atmosphere. The University of North Dakota Citation II collected in situ cloud data from cloud particle imager and a high volume precipitation spectrometer, while the NASA-ER2 flew above most of the convection carrying an X-band radar (EDOP) and several radiometers, among other instruments.

During the field observations, two different environmental regimes were identified. The prevailing direction of the low-level wind switched back and forth from easterly to westerly for periods of several days to over a week (Halverson et al., 2001; Petersen et al., 2001). The two regimes varied markedly in their precipitation and convective characteristics. The easterly regime consisted of more intense, electrified, robust convection with more rainfall being contributed by convective precipitation than stratiform. It also had relatively high convective available potential energy (CAPE; averaging 1530 J kg^{-1} during the easterly phase studied in this thesis), low humidity in the middle and lower atmosphere and large convective inhibition

(CIN; averaging –21 J kg^{-1}). The westerly regime was more monsoon-like in nature with mainly stratiform regions with embedded convection. Its CAPE averaged 1165 J kg^{-1}, was very moist throughout the troposphere and had CIN values averaging –11 J kg^{-1} (Cifelli et al., 2001; Halverson et al., 2001; Rickenbach et al., 2001). Halverson et al. (2001) proposed that the greater |CIN| values for the easterly case allowed more explosive convection to occur once there was enough heating or a triggering mechanism to provide the energy to begin convection. Cifelli et al. (2001) found maximum convective fractions to be near 63% in the easterly case of 26 January 1999 and near 57% in the westerly case of 25 February 1999 (Figure 1.2). Rickenbach et al. (2001) stated that compared to the easterly regime, the westerly regime had a larger fraction of stratiform precipitation and more cloud cover.

Carey et al. (2001) examined a number of observed polarimetric and derived microphysical quantities for each regime from 16 January 1999 to 28 February 1999 during TRMM-LBA (Figure 1.3). Figure 1.3-a shows that the easterly regime has a higher frequency of occurrence of reflectivity > 25 dBZ. In contrast, the westerly regime has a higher occurrence of the lower reflectivities (< 25 dBZ). This agrees with the higher stratiform rain fraction found in the westerly regime (Cifelli et al., 2001; Rickenbach et al, 2001). Figure 1.3-b shows that a higher occurrence of large D_o values are found in the easterly regime, while smaller drops are more often found in the westerly regime. Significant values of K_{dp} are also found more often in the easterly regime (Figure 1.3-c), which agrees with the frequency of higher rain rates also in that regime (Figure 1.3-d). For more information on K_{dp}, see Sec. 2.2.3. These statistical findings agree well with the observed regime-dependent characteristics described above. Similar regime-dependent convection was also found in other tropical locations including Darwin, Austrailia (Rutledge et al., 1992; Williams et al., 1992; Cifelli and Rutledge, 1994).

Because surface rainfall represents the vertically integrated effect of latent heating, these differing characteristics of convection and rainfall for each regime have important implications for the sub-grid parameterization in global circulation models. This study attempts to quantify the latent heating of various hydrometeor types by examining the kinematic and microphysics of one MCS from each regime sampled during TRMM-LBA. The 17 February 1999 case was in the easterly regime while the 23 February 1999 case occurred in the beginning of a westerly period.

1.3 Scientific Objectives and Organization of this Thesis

The scientific objectives of this thesis are threefold:

1) To investigate the kinematic and microphysical structures of two MCSs observed during the easterly and westerly regimes in TRMM-LBA;

2) Obtain an observationally based estimate of the latent heating rates of each system;

3) Compare all results with similar studies from other tropical locations.

This thesis is organized into five chapters. Chapter Two discusses the data and analysis methods used. Chapters Three and Four focus on the case studies 17 February 1999 and 23 February 1999, respectively. Chapter Five compares the findings with previous research and offers suggestions for future work.

Table 1.1: Shows the latent heats of possible phase changes of water.

Latent Heat of Vaporization (at 0º C)	Condensation/Evaporation	2.5×10^{6} J kg^{-1}
Latent Heat of Fusion	Freezing/Melting	3.34×10^{5} J kg^{-1}
Latent Heat of Deposition	Deposition/Sublimation	2.834×10^{6} J kg^{-1}

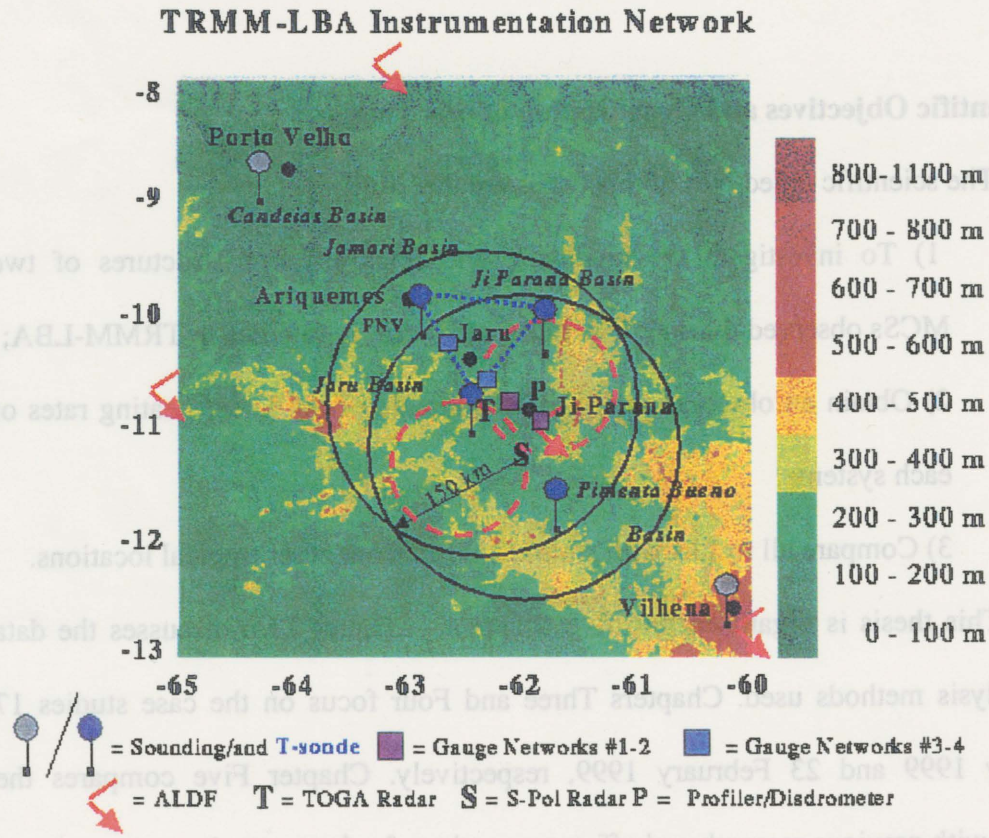

Figure 1.1: TRMM-LBA instrumentation network.

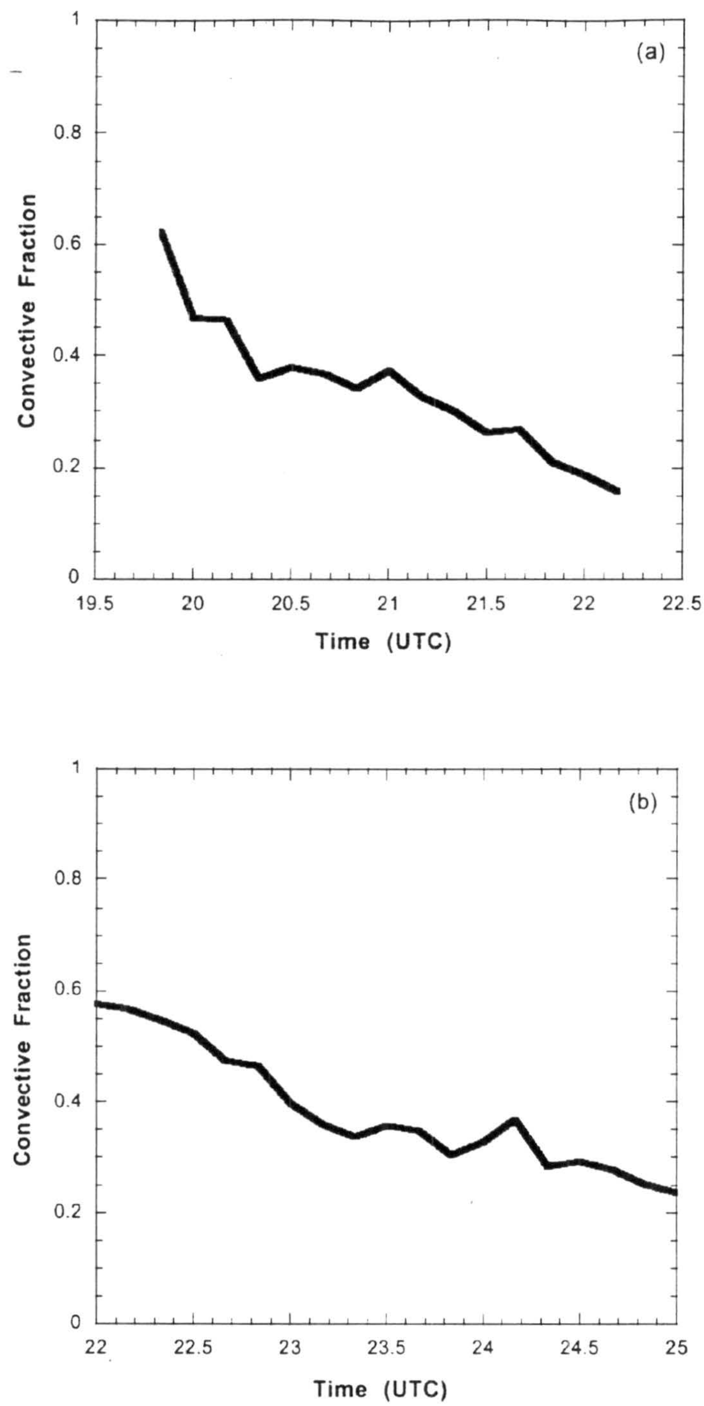

Figure 1.2: Convective fractions for (a) 26 January 1999 easterly case and (b) 25 February 1999 westerly TRMM-LBA case (from Cifelli et al., 2001).

(a)

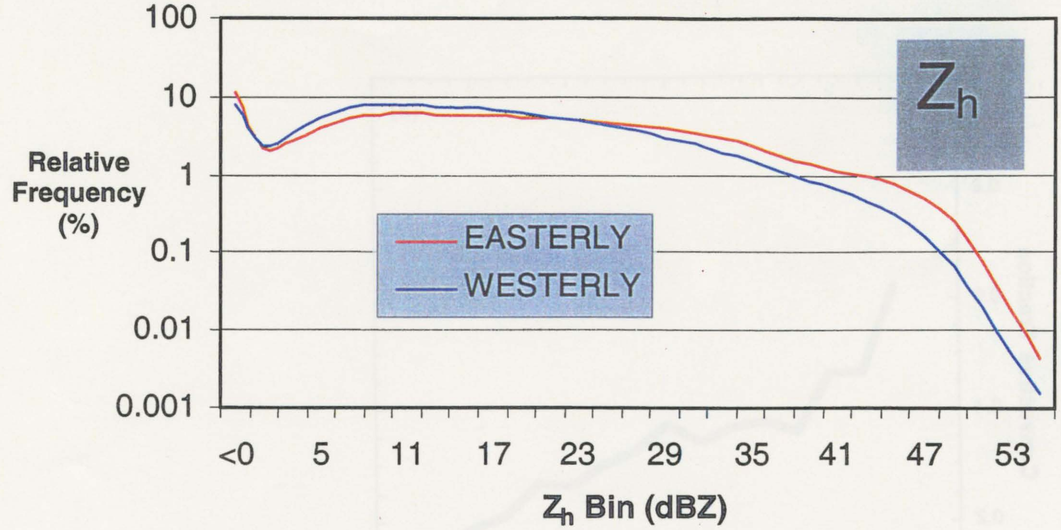

(b)

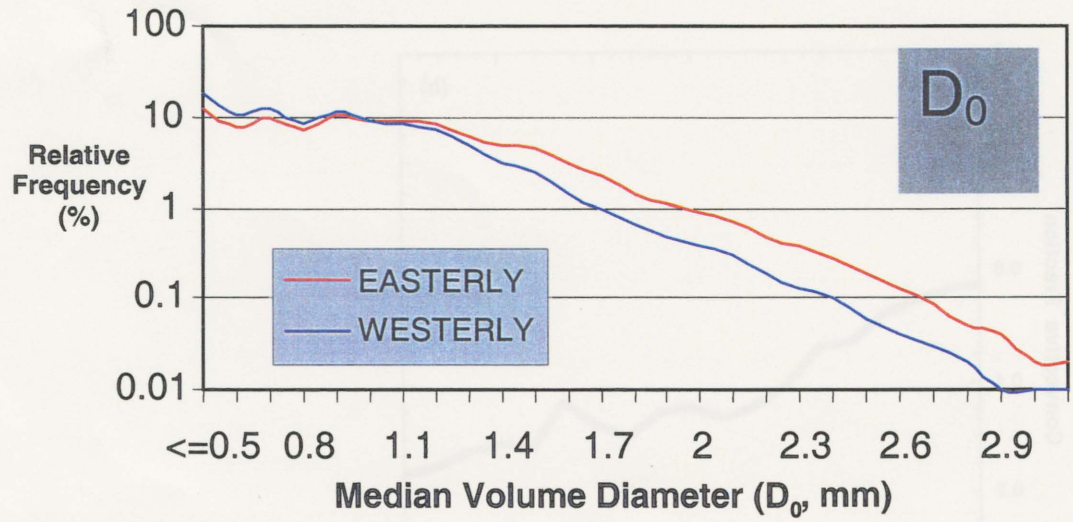

Figure 1.3: Relative frequency of regime dependent variables (From Carey et al., 2001). (a) Reflectivity and (b) median volume drop diameter.

(c)

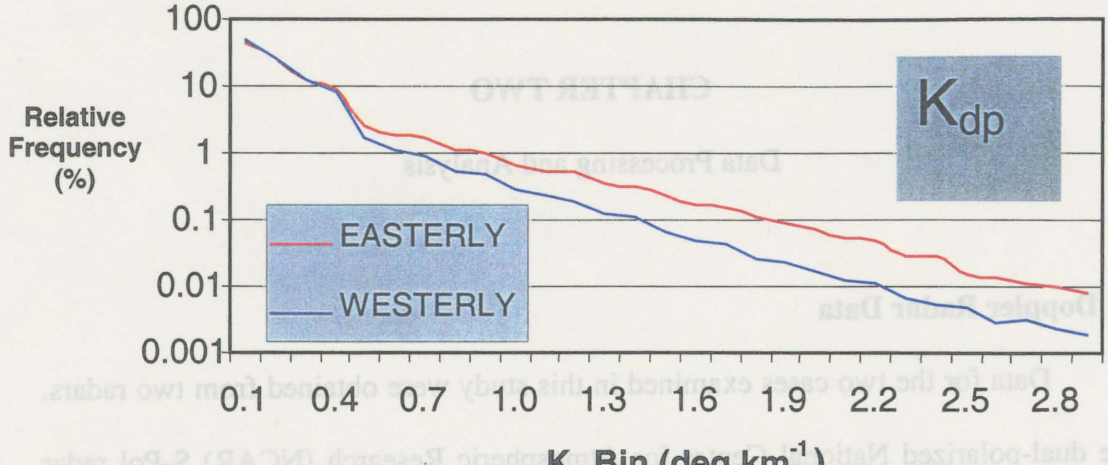

(d)

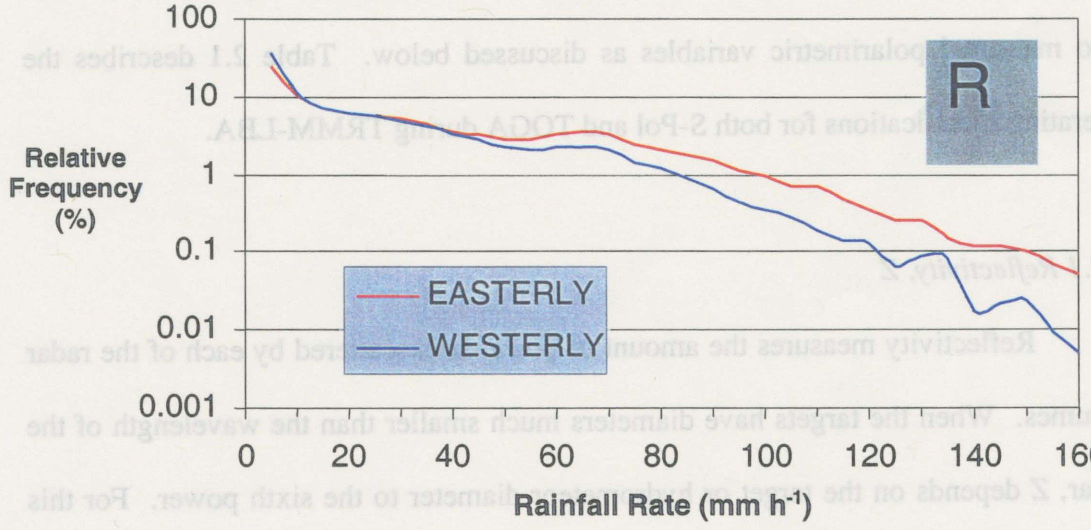

Figure 1.3: Results for (c) specific differential phase and (d) rainfall rate.

CHAPTER TWO

Data Processing and Analysis

2.1 Doppler Radar Data

Data for the two cases examined in this study were obtained from two radars. The dual-polarized National Center for Atmospheric Research (NCAR) S-Pol radar operated at S-band (11 cm), and the NASA TOGA radar operated at C-band (5.33 cm). Both of these radars recorded reflectivity and radial velocity while the S-Pol also measured polarimetric variables as discussed below. Table 2.1 describes the operating specifications for both S-Pol and TOGA during TRMM-LBA.

2.1.1 Reflectivity, Z

Reflectivity measures the amount of power backscattered by each of the radar volumes. When the targets have diameters much smaller than the wavelength of the radar, *Z* depends on the target or hydrometeor diameter to the sixth power. For this Rayleigh approximation, the equivalent reflectivity factor can be expressed as

$$Z_e = \int_0^\infty N(D)D^6 dD \qquad [\mathrm{mm^6 m^{-3}}], \qquad (2.1)$$

where N(D) is the number density and D is the diameter of the targets. Since the values of this reflectivity factor commonly span orders of magnitude, meteorologists use this logarithmic scale:

$$dBZ = 10\log_{10} Z_e \qquad [\text{dBZ}]. \tag{2.2}$$

This scale proves more useful as it ranges from a value near zero in cumulus congestus clouds to values greater than 60 dBZ for intense rain or hail storms (Doviak and Zrnić, 1993).

Reflectivity also depends on the physical composition of the hydrometeor. The general radar equation for a "no loss" system is written as

$$P_r = C\left(\frac{1}{r^2}\right)|K|^2 Z_e. \tag{2.3}$$

P_r is the power received by the radar, C is a radar constant that contains constants and engineering terms related to the radar, r is the range in meters to the target, K is the dielectric factor and Z_e is the equivalent reflectivity factor in mm^6m^{-3}. The dielectric factor depends on the real and complex indices of refraction for ice or water. The standard value used for $|K|^2$ is 0.93, as this corresponds to the assumption that all targets are comprised of pure water. Pure ice targets have a value of 0.197 for $|K|^2$ which results in the correction from Chandrasekar et al. (1991) of

$$dBZ_{ice} = 7.2dB + dBZ_e. \tag{2.4}$$

2.1.2 Radial Velocity, V_r

The radial velocity measures the speed of the targets, but only along the radial direction (i.e., away from or toward the radar). This variable is determined through standard Doppler radar techniques (Doviak and Zrnić, 1993).

2.2 S-Pol Multiparameter Doppler Radar Data

The S-Pol radar can transmit and receive horizontally and vertically polarized electromagnetic radiation. Some of the multiparameter variables measured by the S-Pol radar included horizontal and vertical reflectivity factor ($Z_{h,v}$), differential reflectivity (Z_{dr}), linear depolarization ratio (LDR), and total differential phase (Ψ_{dp}). Other statistical variables are recorded in the full backscattering covariance matrix (Doviak and Zrnić, 1993), but these are not utilized in this study. All these multiparameter variables yield information on the size, shape, orientation, and thermodynamic phase of hydrometeors in a bulk sense (Carey and Rutledge, 1998).

2.2.1 Differential Reflectivity, Z_{dr}

Differential reflectivity is defined using the ratio of the horizontal and vertical reflectivity factors:

$$Z_{dr} = 10\log_{10}\left(\frac{Z_h}{Z_v}\right) \qquad \text{[dB]}. \tag{2.5}$$

Differential reflectivity gives a measure of the oblateness and orientation of the hydrometeors. When a raindrop with diameter greater than 1 mm falls, it becomes an oblate spheroid with the diameter in the horizontal direction greater than in the vertical because of aerodynamic forces (Pruppacher and Beard, 1970). These falling raindrops yield positive values of Z_{dr} with its magnitude increasing with drop diameter. Hail or graupel particles give Z_{dr} values near zero resulting from their quasi-spherical shapes, weak dielectric response to electromagnetic waves, or their tumbling fall modes (Aydin et al., 1984). Negative values of Z_{dr} can occur when the vertical axis is longer than the horizontal axis (Zrnić et al., 1993; Hubbert et al., 1997). For S-band radars like S-Pol, non-Rayleigh scattering by large, wet, oblate hail can give negative values for Z_{dr} (Aydin and Zhao, 1990), although no such values were found in this study.

2.2.2 Linear Depolarization Ratio, LDR

Linear depolarization ratio measures the ratio of the cross-polar received power to the co-polar received power. LDR is defined as

$$LDR_{hv} = 10\log_{10}\left(\frac{P_{hv}}{P_{hh}}\right) \qquad \text{[dB]}, \qquad (2.6)$$

where P_{hv} is the cross-polar return power (transmit v, receive h) and P_{hh} is the co-polar return power (transmit h, receive h). The cross-polar signal, P_{hv}, only occurs if the sphere-like hydrometeors fall with their major or minor axis not aligned nor perpendicular to the electric field. When there is no cross-polar signal, LDR tends toward negative infinity. However, most oblate spheroids wobble during their fall and therefore yield an assortment of canting angles, increasing LDR. The more irregular their shape or higher their dielectric strength, the higher LDR. Values less than or equal to –27 dB generally indicate rain while values higher than that are normally associated with graupel or hail (Doviak and Zrnić, 1993).

2.2.3 Specific Differential Phase, K_{dp}

Specific differential phase, K_{dp}, is not measured directly by the radar. Rather, it is calculated via the total differential phase, Ψ_{dp}:

$$\psi_{dp} = \phi_{dp} + \delta \qquad \text{[degrees]} \tag{2.7}$$

where ϕ_{dp} is the differential propagation phase and δ is the backscatter differential phase. For S-band radars like S-Pol, δ is negligible in rain situations (Jameson, 1985). K_{dp} is calculated from a range derivative of ϕ_{dp} using a finite difference method (after sufficiently filtering ϕ_{dp}).

$$K_{dp} = \left(\frac{1}{2}\right)\left(\frac{d\phi_{dp}}{dr}\right) \approx \frac{\left|\phi_{dp}(r_2) - \phi_{dp}(r_1)\right|}{2(r_2 - r_1)} \tag{2.8}$$

K_{dp} is not affected by isotropic hydrometeors such as hail because such particles make equal phase shifts for the horizontally and vertically polarized electromagnetic waves. K_{dp} is only affected by anisotropic particles, such as oblate raindrops, even in mixed phase environments. This makes K_{dp} a very useful tool in estimating rainfall, especially at high rain rates (Chandrasekar et al., 1990).

2.3 Data Processing

2.3.1 Radar Data Quality Control

S-Pol radar data were edited using the Research Data Support System (RDSS) software developed at NCAR (Oye and Carbone, 1981). An automated program removed most ground clutter and anomalous propagation by thresholding on Z_h, the correlation coefficient and the standard deviation of ϕ_{dp} (Ryzhkov and Zrnić, 1998). The program sufficiently filtered the total differential phase and then used equation 2.8 to calculate K_{dp}. Additional clutter, clear air echo and radial velocity folds were removed manually using RDSS. The program also eliminated data recorded during the movement of the radar when switching between scan types. The TOGA radar data were only manually edited using the RDSS software to remove clutter, clear air echo and many radial velocity folds.

2.3.2 Gridding to Cartesian Coordinates

All variables were interpolated to a Cartesian grid using the REORDER software package, which also was developed at NCAR. The gridding scheme was customized for the each of the two cases analyzed in this study although both used a Cressman weighting scheme (Cressman, 1959). A variable radius of influence was used for the 17 February 99 case, with the delta-azimuth and delta-elevation components of the gridding beam size set between the actual beamwidths of the S-Pol and TOGA radars (see Table 2.1). A fixed radius of influence was used for the 23 February 99 case study with the radius of influence set to 1.5 km in the horizontal and 1 km in the vertical. The variable radius of influence gridding method was also tested, but it caused excessive smoothing of the data especially at high altitudes due to the storm's distance from the radars. Grid resolution for both cases was set at 1.0 km in both horizontal directions and 0.5 km in the vertical.

Storms were gridded to include, as best as possible, all echo from the cells of interest as they progressed through the specified time frame. Some cells that were not directly connected to the MCS under study, but still remained in the grid space were not deleted, as they would still effect the MCS' development and heating. The entire life cycle of the 17 February 99 case was basically captured by the dual-Doppler network. The 23 February case however, could not be entirely covered both spatially and temporally due to the great distance it was away from the S-Pol radar (>125 km).

Full volume radar coverage began approximately mid-way through the storm's evolution. Hence, the beginning volumes only contained the most robust leading edge of the MCS. Later, more of the storm advected into the grid domain and subsequently affected the analysis.

2.3.3 Dual-Doppler

The S-Pol and TOGA radars were positioned effectively to obtain dual-Doppler observations inside the dual-Doppler lobed denoted by the red-dashed circles in Figure 1.1. This study used temporally matched volume PPI (plan position indicator) scans approximately every ten minutes. Taking the radial velocity measurements from both radars, one can solve for the three dimensional air motions inside the dual-Doppler lobes. The outermost parts of the dual-Doppler lobes are defined by a minimum beam-crossing angle from the radars. The more orthogonal the crossing angle, the smaller the error variance as described in the following equation:

$$\csc^2 \beta = \frac{\sigma_u^2 + \sigma_v^2}{\sigma_1^2 + \sigma_2^2} \qquad (2.9)$$

where β is the beam-crossing angle, σ_u^2 and σ_v^2 are the x and y component velocity error variances in the dual-Doppler estimate, respectively, and σ_1^2 and σ_2^2 are the velocity error variances from each radar.

The wind synthesis was done using the NCAR developed Custom Editing and Display of Reduced Information in Cartesian space (CEDRIC) program (Mohr and Miller, 1983). The 17 February 99 winds were synthesized in two groups, 1720-1852

UTC and 1900-2000 UTC, because of the obvious change in storm direction and speed. The edited velocity fields were entered from both radars, but reflectivity was used from S-Pol because of reduced effects from attenuation and/or side lobes. A generous thirty-degree beam-crossing angle was used for the easterly case. In order to solve the dual-Doppler synthesis equations with two radars, one must estimate the fallspeed of the hydrometeors. A simple Z_h-V_t relationship above and below the melting level is widely accepted for these estimates. To find the vertical velocities, CEDRIC must first assume them to be zero and then compute the convergence and divergence fields. Next a downward integration of the mass continuity equation was used to retrieve realistic vertical velocity fields and the horizontal winds were re-computed. Downward integration was chosen because density decreases exponentially with height and this reduces the residual errors at the surface (Bohne and Srivastiva, 1975). The program iterates until the solution converges. CEDRIC was run similarly for the 23 February 99 case, although the beam-crossing angle was relaxed to twenty degrees in order to extend the wind field as far as the reflectivity field. This relaxation of the angle caused some smoothing of the data at distances far from the S-Pol radar. This storm did not make any notable direction or speed changes and therefore the program was run using one set of values for the advection correction.

2.3.4 Convective / Stratiform Partitioning

Next the data were partitioned into convective and stratiform components using a method based on Steiner et al. (1995). The method was further developed by

Dr. Tom Rickenbach at JCET/NASA GSFC. This technique examines the spatial uniformity and intensity of a low level map of radar reflectivity to delineate areas of horizontally variable precipitation (convective rainfall) from weaker, horizontally uniform precipitation (stratiform rainfall). A horizontal cross section of reflectivity is examined at 2 km AGL for local maxima in the reflectivity field. Any local maximum greater than or equal to 40 dBZ was identified as a convective cell. A weaker reflectivity point could be labeled convective if its reflectivity was larger than the surrounding values (within an 11 km radius circle) by 4.5 dB. This roughly corresponds to a factor of two in rainfall difference (Churchill and Houze, 1984). Then a circular "cell" surrounding the convective point is also placed in the convective category to simulate a convective cell. The radius of this cell is directly proportional to the reflectivity value of the core, and varies between 1 km and 5 km. Once a reflectivity map at the 2 km height level is partitioned, all points in the column above and below each convective grid point is considered to be convective. Finally, because the thresholding is performed at low levels and extrapolated upwards, the algorithm may produce spurious results in regions of large vertical shear. No regions of large vertical shear were observed in this study.

2.4 Water and Ice Analysis

2.4.1 Water and Ice Partitioning

In order to objectively discriminate between water and ice in mixed phase environments, Golestani et al. (1989) utilized the difference reflectivity defined as

$$Z_{dp} = Z_h - Z_v \qquad [\mathrm{mm^6 m^{-3}}]. \qquad (2.10)$$

When $Z_v < Z_h$ or in the case of rain hydrometeors, Z_{dp} is positive, and one can rewrite the equation in terms of decibels.

$$Z_{dp} = 10\log_{10}(Z_h - Z_v) \qquad [\text{dB}]. \tag{2.11}$$

Z_h and Z_v are reflectivity factors in mm^6m^{-3}. Ice is assumed to contribute to reflectivity equally in the horizontal and vertical dimensions, so values of Z_{dp} other than zero are solely due to rain. When ice is not purely spherical, the tumbling and wobbling will make it appear so (Knight and Knight, 1970).

In pure rain situations, Z_h and Z_{dp} have a linear relationship for near gamma drop size distributions. Natural variations in raindrop size has been shown to follow a gamma model of the form

$$N(D) = N_o D^{\mu} e^{-\Lambda D} \tag{2.12}$$

where N(D) is the number density, N_o is 8 x 10^3 m^{-3} mm^{-1} and

$$\Lambda = \frac{3.67 + \mu}{D_o} \tag{2.13}$$

where D_o is the median drop diameter (Ulbrich, 1983). Using data sure to be in rain regions of each MCS (1-2 km above ground level; AGL), an overall relationship was found for the entire lifespan of each storm (Figure 2.1). Limiting the data for the linear relationship to reflectivities > 35 dBZ and differential reflectivities > 0.5 dB ensures oblate spheroid raindrops with strong Z_{dp} signatures. The direct variation equation, now called the "rainline," and the standard error found for the plot relate well to published relationships (Conway and Zrnić 1993; Golestani et al. 1989; Carey and Rutledge, 1996), although all those equations were computed from data in the middle latitudes (Table 2.2). Table 2.2 also shows unpublished work done in the tropics that agree extremely well to those found in this study (L. D. Carey, personal communication, 2001). Sensitivity tests were done to examine if the relationship was sensitive to the chosen reflectivity threshold of 35 dBZ. Hence the Z_{dp} versus Z_h plots were done for individual volumes of Z_h beginning at 35 dBZ and increasing by 5 dBZ steps. No significant bias was found. In a mixed phase region, points fall vertically off the line giving a measurable delta Z_h in dB. This delta Z_h can be used to compute the fraction of reflectivity due to rain and ice, $Z_{h,rain}$ and $Z_{h,ice}$ from the following equations:

$$f = 1 - 10^{-0.1(\Delta Z_h)} = \frac{Z_{h,ice}}{Z_h} \tag{2.14}$$

$$Z_{h,rain} = Z_h(1 - f) \tag{2.15}$$

where f is the ice fraction, or fraction of reflectivity due to ice. For more information on the statistical properties of Z_{dp}, see Tong et al. (1998).

2.4.2 Calculating the Mass of Water and Ice

A Fortran program as used in Carey and Rutledge (2000) was modified to calculate the mass of water and ice associated with these storms. The statistics from the Z_h-Z_{dp} correlation were put into the code. Instead of using equations 2.14 and 2.15 to find $Z_{h,rain}$ and $Z_{h,ice}$, this study used the more statistical approach as in Carey and Rutledge (2000). If the pulse volume's delta Z_h away from the "rainline" is large enough (at least greater than the standard error of the line), it is labeled as ice. If not, it is considered to be rain. A multiplicative factor determines exactly how far the Z_h-Z_{dp} point needs to be away from the "rainline" to be considered ice. This factor has a linear relationship with height above and below the freezing level. For example, the further below the freezing level the point is, the larger the delta Z_h must be from the "rainline" to assume that the reflectivity is due to ice. The multiplicative factor was tuned to match the observed characteristics of the tropical convection during TRMM-LBA. The mass of ice was then calculated based on the Rayleigh approximation using a relationship from Carey and Rutledge (2000):

$$M_{ice} = 1000\pi\left(\frac{\rho_i}{\rho_a}\right)N_o^{3/7}\left(\frac{5.28x10^{-18}Z_h^{ice}}{720}\right)^{4/7} \quad [\text{g kg}^{-1}], \qquad (2.16)$$

where ρ_i is the ice density (kg m^{-3}), ρ_a is the air density (kg m^{-3}), N_o ($4x10^6$ m^{-4}) is an intercept parameter taken from a bulk-microphysical cloud modeling study done over the Tiwi Islands (Petersen, 1997). The ρ_i used for these cases was 917 kg m^{-3}. The mass of water was calculated using two relationships. Most often the Ryzhkov and Zrnić (1995) relationship was employed:

$$M_{water} = 3.44x10^{-3}(Z_{water})^{4/7} \quad [\text{g m}^{-3}], \qquad (2.17)$$

where Z_{water} is the reflectivity factor due to water in mm^{6}m^{-3}. For reflectivities exceeding 35 dBZ and Z_{dr} greater than 0.4 dB, the following relationship was used to take advantage of the measurements in the horizontal and vertical polarizations:

$$M_{water} = 0.7x10^3\left(\frac{Z_v^{4.159}}{Z_h^{3.273}}\right) \quad [\text{g m}^{-3}], \qquad (2.18)$$

where Z_h and Z_v are the respective reflectivity factors in mm^6m^{-3} (Bringi and Chandrasekar, 2000). The mass of ice and water were calculated at every grid point in every volume for each of the storms. The program was also run for the divided convective and stratiform grid points using the Z_h-Z_{dp} statistics from the entire storms.

2.4.3 Latent Heating Rates

The latent heating rates were calculated using water and ice budgets similar to Tong et al. (1998), although the present study included the effects of deposition, sublimation, and riming. The water and ice budgets can be expressed as

$$\left.\frac{dM}{dt}\right)_{volume} = C - E - R - F + Me - Rim \tag{2.19}$$

$$\left.\frac{dI}{dt}\right)_{volume} = F - Me + D - S + Rim\,, \tag{2.20}$$

where dM/dt is the time rate of change of the volume total liquid water content, dI/dt is the time rate of change of the volume total ice content, C is the condensation rate, E is the evaporation rate, R is the rain rate, F is the freezing rate of liquid water to ice, Me is the melting rate of ice to liquid water, Rim is the rate that supercooled raindrops freeze onto ice or mixed phase particles, D is the deposition rate and S is the sublimation rate.

Changes of water and ice mass were computed using a finite difference method over the dual-Doppler time periods using the masses calculated as in section 2.4.2. The rain rate was found at 1 km using polarimetrically tuned Z-R relationships specifically created for TRMM-LBA (Carey et al., 2001). The easterly (westerly) relationship created for rain rates greater than 10 mm hr^{-1} was used for the easterly (westerly) convective grid points. The only other regime dependent Z-R relationship calculated was for all rain rates; these were used for the stratiform grid points for each regime. For exact equations used, see Table 3.2.

Next, the method to determine where the supercooled drops were riming was required. To do this, the ice mass concentrations were plotted versus reflectivity (Figure 2.2-a). Most points fell along a curve since both concentration and reflectivity depend on the diameter of the hydrometeor. But a fraction of points were situated off the curve on the side of higher reflectivity. When the water mass concentrations are overplotted, it is obvious that the ice points that fall off the "ice curve" lie along the curve relating water mass concentration to reflectivity (Figure 2.2-b). These points were labeled as mixed phase locations because the points are categorized as ice by their shape (according to the Z_{dp} method), but have a much higher reflectivity due to the presence of water. Note also that Figure 2.2-b shows the water plots to be somewhat bimodal. This is because the plot's abscissa is mass concentration. For the same mass concentration, two different reflectivities could be obtained based on the diameters of the hydrometeors involved. The final criteria for the presence of riming was that the grid point updraft exceeded 3 m s^{-1} and $dI/dt > 0$. Pruppacher and Klett (1997) find 3 m s^{-1} to be an adequate updraft to carry graupel. These criteria eliminated the points that were also mixed phase, but only contained melting drops. Upon close inspection, the horizontal and vertical locations, and polarimetric signatures of these riming grid points seem reasonable. Hence, the loss of water mass and gain in ice mass in these regions was attributed to riming.

The remaining values for dI/dt were divided into two groups. Any change in ice for temperatures > -10° C was attributed to freezing or melting processes. Similarly, for T < -10° C, deposition or sublimation processes were assumed. The deposition category included the dry growth of graupel.

The previously described variables were derived from radar data leaving C-E as the residual. The latent heating rate due to condensation and evaporation from these terms was obtained by multiplying by the latent heat of vaporization, $L_v = 2.50 \times 10^6$ J kg^{-1}. The heating rate from the F-Me terms is derived by multiplying the associated dI/dt by the latent heat of fusion, $L_f = 3.34 \times 10^5$ J kg^{-1}. Likewise, the D-S heating rate uses the latent heat of deposition, $L_d = 2.834 \times 10^6$ J kg^{-1} and the associated dI/dt, as riming grids use L_f and associated dM/dt values. It is obvious that the latent heating rates due to freezing, melting and riming will be small in comparison to the others as L_f is an order of magnitude smaller compared to the other latent heating terms.

Table 2.1: Operating specifications for radars during TRMM-LBA campaign.

Operating Specification	**S-Pol Radar**	**TOGA Radar**
Transmitter	11 cm	5.33 cm
Pulse Width	0.3 – 1.4 μsec – tapered	0.5 μsec
PRF	0 – 1300 Hz	0-1000 pulse/sec
Peak Power	> 1 Mw	260-270 kW
Receivers	H & V simultaneously	H only
Radar Noise Figure	2.9 dB	4.3 dB
Dynamic Range	90 dB	80 dB
Antenna	Parabolic, center feed	Parabolic, center feed
Beamwidth	0.91 degrees	1.55 degrees
First sidelobe	Better than –30 dB	Better than –23 dB
Scan Rate	Up to 18 °/sec each axis; 30 °/sec with pulley change	17-18 °/sec
Wind limit for operation	30 ms^{-1}; 60 ms^{-1} (no radome)	Has radome

Table 2.2: Equations from this study and others relating Z_h and Z_{dp} and their statistical properties.

Source	Equation	Standard Error (dB)	Corr. Coeff.
This study: 17 Feb 99 Easterly Case	$Z_h = 0.77Z_{dp} + 14.5$	1.015	0.959
This study: 23 Feb 99 Westerly Case	$Z_h = 0.76Z_{dp} + 15.2$	0.881	0.965
Golestani et al, 1989	$Z_h = 0.83Z_{dp} + 12.8$	-	-
Conway and Zrnić, 1993	$Z_h = 0.88Z_{dp} + 8.05$	-	-
Carey and Rutledge, 1996	$Z_h = 0.91Z_{dp} + 8.55$	-	-
TRMM-LBA – Carey 01 Entire Easterly Regime	$Z_h = 0.77Z_{dp} + 14.5$	1.1	-
TRMM-LBA – Carey 01 Entire Westerly Regime	$Z_h = 0.74Z_{dp} + 15.95$	0.8	-

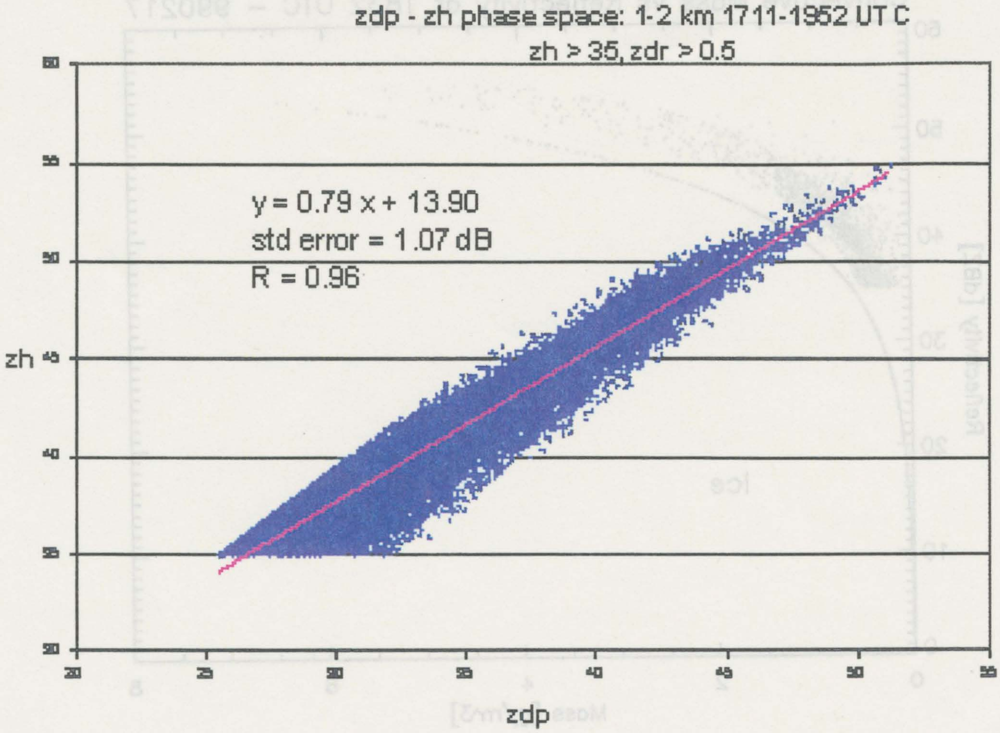

Figure 2.1: Example plot of Z_{dp} versus Z_h in a pure rain situation for the 17 February 1999 case.

(a)

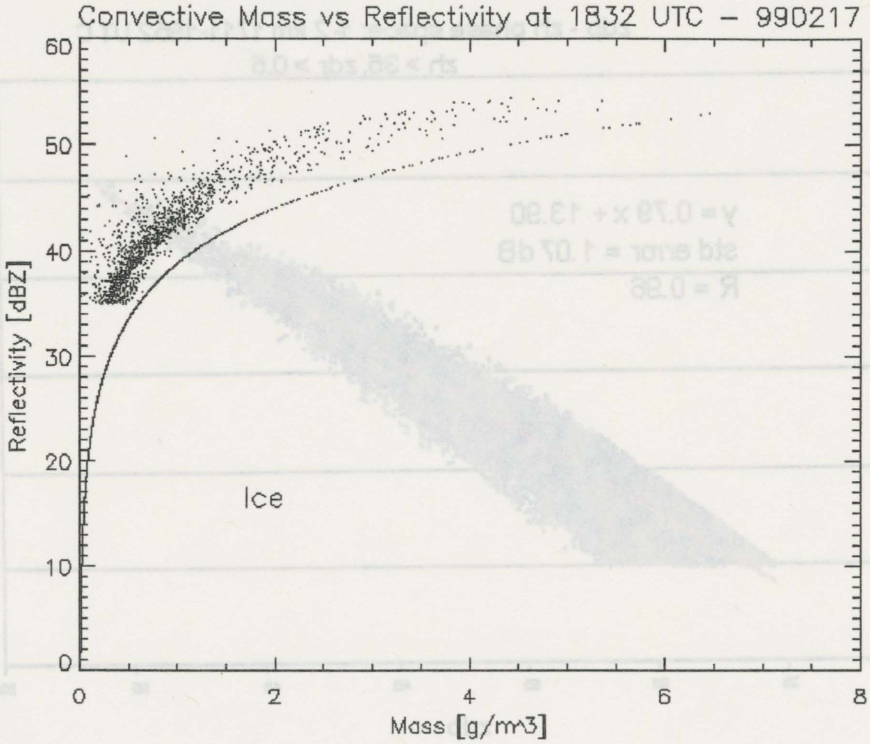

(b)

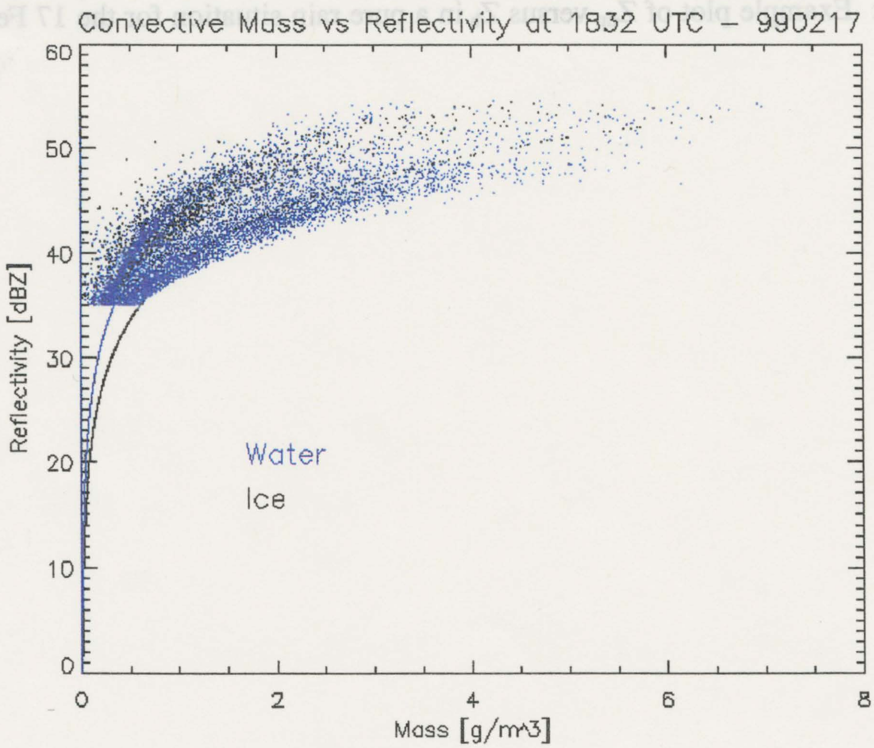

Figure 2.2: Example plot of reflectivity vs (a) ice mass concentration and (b) ice and water mass concentrations for one volume scan of the 17 February 1999 case.

CHAPTER THREE

17 February 1999 Case Study

The 17 February 1999 case occurred in the easterly regime of TRMM-LBA, as previously defined. This case's convection began with typical scattered, cellular convection, triggered by the heating of the surface throughout the day. From 1720 to 1952 UTC (1320 to 1552 local time), a few cells tracked into the dual-Doppler domain and merged into a mesoscale convective system. Instantaneous rain rates in excess of 150 mm hr^{-1} were observed between 1832 and 1842 UTC and nearly 60 mm of total accumulated rain occurred in some regions. An investigation of the atmospheric conditions, storm evolution, kinematics, microphysics and latent heating rates for this case follows.

3.1 Atmospheric Conditions

Figure 3.1 is a Skew-T/Log-P diagram depicting the local troposphere at 1500 UTC, prior to convective initiation. This sounding shows the low-level easterly winds that classify this storm as an easterly regime case. Note the stronger easterly winds aloft, leading to a sufficient amount of shear for thunderstorm organization. The temperature and dew point curves are close together from the surface up to approximately 830 hPa showing ample surface moisture. Above 850 hPa, the environment is drier. The easterly cases, on average, do exhibit this drier air aloft (Halverson et al., 2001).

The convective available potential energy (CAPE) reflects the integrated positive energy area between the condensation and equilibrium levels. Its value in this case is 2327 J kg^{-1}, which is higher than average for a tropical location (Halverson et al., 2001). The convective inhibition energy (CIN, or CINE as in Figure 3.1) represents the amount of energy required for an air parcel to be lifted dry-adiabatically from the surface to the condensation level. In this case, the CIN is 0 J kg^{-1}; hence there is no barrier to convection. A variable that relates the ratio of CAPE to vertical shear is the Bulk Richardson Number (R_i, or RB as in Figure 3.1) and its value at this time is 38. Modeling studies in the middle latitudes have shown that multi-cellular growth as seen in this study is consistent with R_i's greater than 30 (Weisman and Klemp, 1982).

3.2 Overview of Storm Evolution

3.2.1 Dual-Doppler Analysis

The observed S-Pol reflectivity from 17 February 1999 is shown in Figure 3.2 for five time periods during the storm spaced approximately 30 minutes apart. Figure 3.2-a shows the beginning convection as four strong cells scattered throughout the domain at 1740 UTC. The reflectivities exceed 45 dBZ, but no organization is present. This multi-cellular growth agrees with the Richardson number prediction. By 1811 UTC (Figure 3.2-b), some mesoscale organization is evident; note the T-shaped echo in the lower-right side of the domain. This group of cells moved rather quickly at approximately 7.0 m s^{-1} from 55 degrees. The cells merged together to form one main entity by 1842 UTC (Figure 3.2-c), although several separate updrafts were still found. Reflectivities peaked near this time (> 50 dBZ) and echo tops reached 17 km AGL. After the merger of the cells, the MCS moved slower (~ 4 m s^{-1}) from 45 degrees. Figure 3.2-d shows the storm at 1912 UTC. The reflectivity intensity has weakened and the storm has not moved much since the previous time. By 1952 UTC, the storm has considerably weakened with lower echo tops near 12 km (Figure 3.2-e).

Mean vertical velocities in the convective region are shown in Figure 3.7. They range from just below 0 cm s^{-1} during the system's decline to nearly 22 cm s^{-1} at its maximum (1842 UTC). Most updrafts contained maximum vertical velocities between 5 and 10 m s^{-1} (not shown). These vertical velocities are similar to other values found for tropical convection (LeMone and Zipser, 1980; Jorgensen and LeMone, 1989; Lucas et al., 1994). The probability of finding that 10 m s^{-1} vertical velocity maximum is 5% according to Jorgensen and LeMone (1989). Strong updrafts exceeded 18 m s^{-1}; Jorgensen and LeMone (1989) had the probability of finding an 18 m s^{-1} updraft maximum at less than 1%.

3.2.2 Polarimetric Analysis

To calculate rain rates from radar data, a Z-R (reflectivity and rain rate) relationship is most often used. The National Weather Service WSR-88D radars use one Z-R relationship for every operational situation. This is not always appropriate as the relationship between reflectivity and rain rate changes for different locations, times and drop size distributions. Table 3.1 shows the equations that use polarimetric variables to more accurately calculate rain rates from radar data (Bringi and Chandrasekar, 2000). Choosing the most appropriate equation depends on the ranges of the rain rates. These polarimetric-based estimates of rain rate are usually within 5-25% of gauge accumulations and therefore can be used to "tune" the traditional Z-R relationships (Carey et al., 2001). Carey et al. (2001) developed polarimetrically tuned Z-R relationships for the entire TRMM-LBA dataset. The results are shown in Table 3.2. The "all rain rates" easterly relationship was used for stratiform precipitation for this case and the easterly $R \geq 10$ mm hr^{-1} relationship was used for convective precipitation.

The volume total rain rates for each time period were then calculated using reflectivity at 1 km (Figure 3.3). The rain rates steadily built through 1822 UTC, followed by a period of rapid increase peaking at 7×10^6 kg s^{-1} (~11 mm hr^{-1} per grid space) at 1842 UTC. This increase in rain rate occurred as the cells merged into an organized system and the updrafts became stronger and more protected from the drier environmental air. Cold outflow boundaries likely flowed from the downdrafts releasing these large amounts of rain. After 1842 UTC, volume rain rates decreased quickly. This was probably due to several reasons. First, the storm's peak reflectivities were lessening as the storm was beginning to decay. Since the rain rate was calculated via reflectivity, this reason for the decrease is obvious. Another possibility is that the outflow boundaries are cutting off updrafts and the precipitation forming process. Note the mean vertical velocities do decrease after 1842 UTC

(Figure 3.7-a). Finally, the drier environmental air could be entraining into the MCS, causing evaporation of some of the water.

A vertical cross-section through one of the main updrafts at the most robust time period, 1842 UTC, is shown in Figure 3.4. Figure 3.4-a shows reflectivity greater than 40 dBZ from near the surface up to 6.5 km. The overlay of Z_{dr} has large values in this same region exceeding 2.5 dB. The combination of these two variables in the updraft indicates that there are large, oblate drops being lofted up into the storm. Figure 3.4-b shows that the strength of the updraft in this region reaches 15 m s^{-1}, which is very capable of lofting such drops (Pruppacher and Klett, 1997). Note that the Z_{dr} forms a column of heightened values inside the updraft. This feature is referred to as a Z_{dr} column (Fulton and Heymsfield, 1991; Herzegh and Jameson, 1992). Such Z_{dr} columns are common in mid-latitude convection when strong updrafts loft supercooled rain drops to sub-freezing temperatures (Fulton and Heymsfield, 1991; Herzegh and Jameson, 1992; Bringi et al., 1997 and others). Evidently, this process is also operative in strong tropical convection during the easterly phase in TRMM-LBA and other regions (Carey and Rutledge, 2000; Rutledge et al., 2000; Cifelli et al., 2001). Note that the erratic Z_{dr} signal around the outside of the echo is probably due to a low signal-to-noise ratio (Herzegh and Carbone, 1984). The maximum vertical velocity occurs at higher altitudes near 12 km AGL. This is often observed in the tropics as water "unloading" and latent heat released from condensation and freezing makes the parcel more buoyant above the freezing level (Petersen et al., 1999).

Figure 3.4-c shows the Linear Depolarization Ratio (LDR) through this cross-section with values ranging from –20 dB to less than –30 dB. However, during TRMM-LBA, it was observed that LDR values were too high by approximately 3 dB due to slightly non-orthogonal H, V polarization bases. Since the H, V polarizations were less than 90°, the effect was to increase values of LDR. Figure 3.5 shows a scatter plot of LDR values in a rain region that are too high as compared to values found in the literature (Doviak and Zrnić, 1993; Bringi and Chandrasekar, 2001). Table 3.3 shows the LDR range for rain to be –27 to -34. Thus, the maximum LDR values for this cross-section are –23 dB. No overall correction was incorporated for the entire dataset, as it was not clear if the non-orthogonality would effect every portion of the storm, spatially or temporally. So each LDR cross section should be individually analyzed in context with the other data. Directly above the Z_{dr} column, LDR values rise to around –21 dB, or –24 dB after the correction. This increase in LDR right above a Z_{dr} column is referred to as an "LDR cap." An LDR cap signifies the riming and freezing of drops in the updraft (Bringi et al., 1997; Smith et al., 1999; Bringi and Chandrasekar, 2001; Rutledge et al., 2000). Fulton and Heymsfield (1991) describe the LDR cap location as a "fountain" of tumbling, frozen drops and/or wetted aspherical ice particles such as graupel. The vertical location of this agrees well with the fact that the freezing level is also approximately 5 km (Figure 3.1). Note that this variable also gets erroneous values along the echo edge.

Specific Differential Phase (K_{dp}) is shown in Figure 3.4-d. The only real feature is the column of moderate K_{dp} (>1.0 deg km^{-1}) found in the same location as the Z_{dr} column. Since K_{dp} is only sensitive to oblate water drops, this column is indicative of the large drops being lofted into the storm (consistent with the inferences from Z_{dr}). Notice how the K_{dp} column does rise above the freezing level slightly, indicating a region of supercooled drops. Some of the water could also be falling out of the storm as precipitation, although the updraft is intense (~10 m s^{-1}).

Using the Z_{dp} technique (c.f. Sec. 2.4.1), cross-sections depicting water and ice mixing ratios can also be determined. Figure 3.4-e shows the result along the same cross section described above. An area of mixed phase can easily been seen by the overlapping contours from just below 5 km to 6 km AGL. The mixing ratio values correspond well to aircraft in situ data from another easterly case day, 26 January 1999. Stith et al. (2001) found water mixing ratios up to 4 g m^{-3} near updrafts of 13 m s^{-1}.

Bulk hydrometeor classification can also be done using a reference table (Table 3.3) adapted from Doviak and Zrnić (1993). The aforementioned updraft (from the surface around x = 5 km to approximately 5 km in the vertical) in Figure 3.4-a had values of reflectivity above 45 dBZ, Z_{dr} above 2.5 dB, LDR around –28 dB (corrected), and K_{dp} greater than 1 deg km^{-1}. The bulk hydrometeor type in this location is then determined to be rain by Table 3.3. Just above 5 km, values near the top of the Z_{dr} column and the LDR cap yield the bulk hydrometeor type to be wet graupel. This agrees with the previous discussion of lofting drops, subsequent freezing and riming just above the freezing level. Graupel was observed via in-situ measurements in tropical convection by the University of North Dakota (UND) Citation aircraft during the TRMM-LBA and Kwajalein campaigns (Stith et al., 2001). In particular, Stith et al. (2001) observed graupel in an updraft of a few m s^{-1}

at $-18°$ C (~8 km AGL) at 1810 UTC on 17 February 1999. Another region that is interesting from a polarimetric perspective in Figure 3.4-c is near x = -2 km and 12 km in the vertical. There is hardly any Z_{dr} or K_{dp} signal and the reflectivity is approximately 20 dBZ, but the LDR has decreased to –28 dB (corrected). Table 3.3 shows that with these values, the bulk hydrometeor type is high density, dry crystals. This area is in a region of overturning as seen through the wind velocity arrows in Figure 3.4-c. Crystals carried aloft from the updraft are likely mixing with other type of crystals already in the downdraft or forming nearby. This running together of different types of crystals can give such a signature in LDR.

This polarimetric analysis proves that at least this portion of the 17 February 1999 storm was capable of supporting an efficient collision-coalescence precipitation process, had strong enough updrafts to loft drops above the freezing level, and sufficient mixed phase regions to rime the graupel. Stith et al. (2001) noted other regions of this storm being driven by warm rain processes. However, those regions had weaker updrafts (< 5 m s^{-1}) and little polarimetric signals.

3.3 Water and Ice Partitioning

3.3.1 Masses of Water and Ice

The water and ice partitioning as described in Sec. 2.4.1 can provide further insights into storm structure and evolution. Figure 3.6-a shows the average mass profile for 17 February 1999 for the radar volumes available for this case subdivided into ice and water. Recalling that the data are at 0.5 km resolution in the vertical, it is easily seen that most of the ice is found between 3 and 16 km with maximum values near 1.5 x 10^8 kg. Water is found from 0.5 km to 7 km AGL with magnitudes on the order of 10^8 kg. Approximate mixing ratios for ice and water can be seen in Figure 3.4-e. Figure 3.6-b further shows the categorization of masses used to estimate the latent heating rate. The ice mass changes due to deposition and sublimation begin at 6.5 km (location of -10° C isotherm) and continue to the average storm top of 16 km. The ice mass changes due to freezing and melting occur from the layer beginning at 6 km down to 3 km on average. Water is found from the lowest resolution elevation (0.5 km) to 7 km and supercooled water available for the riming process is located between 4 and 7 km AGL. Even though text soundings show some below freezing temperatures occurring near 4.5 and 5 km AGL prior to the storm's development, it is possible that some freezing temperatures occurred near 4 km at some areas in the MCS. Stith et al. (2001) did find significant amounts of supercooled water at temperatures > -7° C (~6 km AGL) with some trace amounts up to –18° C (~8 km AGL), although the aircraft did not sample the most robust convection.

A depiction of how these masses changed as the storm evolved is shown in Figure 3.7. Clearly, the water mass (70%) dominates the ice mass (30%) at 1842 UTC. This figure also shows the mean convective vertical velocities in m s^{-1} as previously described in Sec. 3.2.1. Notice that the water and ice masses peak after an increase in mean convective vertical velocity. This is reasonable because stronger vertical velocities can support more water and ice mass in the storm. After the third peak in vertical velocity, however, the water and ice masses drop significantly. This is co-located with the maximum in rain rate (Figure 3.3). It is likely that this water "unloading" is reducing the mean vertical velocities, therefore affecting the amount of mass the storm can hold at a later time. Figure 3.7-b further shows the categorization of masses used to estimate the latent heating rate. The ice mass used for deposition and sublimation latent heating estimation grows throughout the beginning volumes and reaches its maximum of 1.6 x 10^9 kg at 1842 UTC. The "freezing/melting" curve is nearly the same shape and magnitude in the beginning, but it does not have such a strong maximum at 1842 UTC. The "riming" curve's magnitude is less than the other two ice-related curves, but it exhibits two peaks in its lifetime correlated with increases in mean vertical velocity. The first push occurs when the domain is still filled with scattered, intense cells at 1800 UTC. The second, longer, and more intense push occurs when these scattered cells have merged together to form the MCS (1832-1842 UTC). Recall this is the time when the vertical cross section in Figure 3.4 was made. That cross section showed high reflectivity, strong vertical velocities, a Z_{dr} column, a LDR cap and an active mixed phase region, all microphysically indicative of riming (Fulton and Heymsfield, 1991; Herzegh and Jameson, 1992; Bringi et al., 1997; Carey and Rutledge, 2000; Cifelli et al., 2001).

3.3.2 Associated Latent Heating Rates

The latent heating rates, estimated as described in Sec. 2.4.3, are shown in Figure 3.8 for the duration of this storm. Throughout most of the event, the condensation term dominates reaching a maximum value of 2.2 x 10^{13} J s^{-1}. There are two substantial decreases in the latent heating rate due to condensation/evaporation curve at 1811 and 1852 UTC. This is presumably related to the two periods of increased masses associated with riming at 1800 and 1832-1842 UTC. The supercooled water likely froze onto nearby ice particles therefore releasing latent heat locally. Since the saturation vapor pressure, e_s, is directly dependent on temperature, the supersaturation, e/e_s, would decrease. This would cause the condensation rate to decrease and therefore the latent heating rate due to condensation to decrease as well. Looking back at Figure 3.7, the storm did not gain much water mass between 1800 and 1811 UTC and it lost water mass after 1842 UTC supporting the previous discussion. After 1922 UTC, the storm probably entrains dry air as the updrafts weaken, and the evaporation term dominates. The latent heating rate due to deposition/sublimation follows the same pattern, but becomes negative by 1852 UTC, earlier than the condensation/evaporation. The reduction in supersaturation would also reduce ice growth by deposition. The heating from the riming and freezing/melting processes are negligible on this figure as they are on the order of 10^{10} J s^{-1}.

A bulk latent heating vertical profile is shown in Figure 3.9 for 1832 UTC, a growth stage in the MCS. The latent heating due to changes in ice mass separates into deposition and sublimation above 6.5 km, and freezing and melting below. The levels for supercooled drops, condensation and evaporation were determined by a graph similar to Figure 3.6, but for the specific time of 1832 UTC. The percentages in the figure correspond to the change(s) of phase experienced at that particular level (or series of levels). The layers are in 0.5 km resolution beginning at the level mentioned in the figure (i.e. 4-6 km would actually represent the layer beginning at 4 km and ending at 6.5 km). Note how condensation dominates at low-levels and deposition at upper levels. The riming and freezing/melting processes do not create much latent heat overall, only contributing at most 4%. Note this is a bulk profile in J s^{-1}, not in J s^{-1} km^{-1}. For example, the 2.25 x 10^{13} J s^{-1} latent heating rate on Fig. 3.9 is for the entire layer from 0.5 km to 4 km, not for each km within the layer.

Figure 3.10 shows the bulk normalized latent heating rate per layer at 1832 UTC. The values in Figure 3.9 were divided by the specific heat of dry air (C_p), the average density for each layer, and the area associated with the rainfall (2384 km^2) and then converted to the proper units to get degrees of heating day^{-1} per cm day^{-1}. The instantaneous rain rate was 22 cm day^{-1} at this time. The maximum heating occurs between 4 and 6.5 km with values exceeding 50 deg day^{-1} per cm day^{-1}. The minimum occurs between 6.5 and 7.5 km and then the heating increases above to 15 km. This is misleading, as the average density for the thin layer between 6.5 and 7.5 km is higher than for the thicker layer above it. Since the heating is divided by the average density for each layer, it seems larger for the layer aloft. If thinner layers were used to normalize the heating, the profile would not look so anomalous at 6.5 to 7.5 km. Again, this is a bulk profile for the levels described in Fig. 3.9 and the values are not for each km within the layers.

3.4 Convective / Stratiform Partitioning

3.4.1 Convective Percentages

To more clearly understand the latent heating rate results, the data was further partitioned into convective and stratiform components as described in Sec. 2.3.4. An example of how the reflectivity was partitioned is shown in Figure 3.11. At this level (1 km), the storm appears to be dominated by convection. Even when the convective percentage is computed for the entire storm (Figure 3.12), the convective fractions are still higher than previous findings in the tropics (Figure 1.2; Cifelli et al., 2001, Halverson et al., 2001). It appears the 17 February easterly case was unusually convective remaining between 55% and 65% convective throughout most of its lifetime probably due to the drier air aloft (Halverson et al., 2001). It then decreases to 35% convective during the mature stages of the storm.

3.4.2 Associated Latent Heating Rates

With this partitioning, it is now possible to more specifically diagnose the latent heating rates due to condensation, evaporation, freezing, melting, deposition and sublimation, as subdivided into convective and stratiform regions. Riming occurred only in the convective components as seen in other TRMM-LBA and Kwajalein cases (Stith et al., 2001). It must be noted that the latent heating rates in the stratiform component may be subject to a fair amount of uncertainty. The stratiform region does not contain much in the way of polarimetric signatures necessary to calculate the masses of ice and water. Therefore the estimation of these parameters may be subject to considerable error. However, the results found in both these case studies do seem reasonable as compared to aircraft in situ measurements during TRMM-LBA (Stith et al., 2001). Figure 3.13 shows the grid-size volume total latent heating rates for 17 February 1999 divided into convective and stratiform components. This set of figures does allow the reader to visualize latent heating profiles in the vertical. The average levels for each thermodynamic process were shown in Figure 3.6-b.

The volume latent heating rates due to condensation and evaporation are shown in Figure 3.13-a. The convective portion is obviously the largest in magnitude and is positive from 1730 to 1922 UTC. This indicates that condensation is dominating evaporation during this growth period and part of the decline period as well. Houze (1997) indicates that convection should heat the lower levels as found in this study. From 1922 to 1952 UTC, the convective component is dominated by evaporation. This correlates well with the way the rain rate is nearing zero during these times (Figure 3.3); a lot of the precipitation is being evaporated. The stratiform component is smaller in magnitude and switches back and forth in sign yielding non-interpretable results.

Figure 3.13-b shows the latent heating rates due to freezing and melting for this case study. Similar to the condensation/evaporation discussion, the convective component is larger than the stratiform. The values are mostly positive from 1730 to 1842 UTC and negative afterward. An outlier in the positive then negative trend is 1811 UTC. Both the convective and stratiform components are negative implying excessive melting. This is during the scattered multi-cellular stage of the storm. Each individual cell could be beginning to decay, as decaying convection tends to melt more hydrometeors than it freezes. Then by the next time period, the cells began interacting to form a more cohesive and stronger MCS and freezing becomes prevalent once again. After 1842 UTC, the convective component is largely negative implying melting processes at the midlevels of the storm, while the stratiform component wavers back and forth in sign.

The latent heating rates due to deposition and sublimation are shown in Figure 3.13-c. The convective component has two obvious spikes during the growth period: 1800 and 1832-1842 UTC. These are the exact times of the spikes in the riming process shown in Figure 3.7. This heating by deposition likely occurred on the rimed particles as they were lofted further into the storm. This heating aloft by convection agrees with Houze (1997). Right after the transition to the decline phase, sublimation was the dominant term. The stratiform component continues to yield non-interpretable results, as it is small in magnitude and changes sign frequently.

Table 3.1: Equations to calculate rain rates using polarimetric variables (Bringi and Chandrasekar, 2001).

$R(K_{dp}, Z_{dr}) = 87.6 * (K_{dp})^{0.934} * 10^{(0.1*-1.59*Z_{dr})}$ mm hr^{-1}
$R(Z_h, Z_{dr}) = 6.7x10^{-3} * (Z_h)^{0.927} * 10^{(0.1*-3.433*Z_{dr})}$ mm hr^{-1}
$R(K_{dp}) = 53.8 * (K_{dp})^{0.85}$ mm hr^{-1}

Table 3.2: Polarimetrically tuned Z-R relationships for TRMM-LBA.

Wind Regime	R Restriction	Z-R Equation
Easterly	All Rain Rates	$Z = 485R^{1.08}$
Easterly	R $\geq$ 10 mm hr^{-1}	$Z = 531R^{1.08}$
Westerly	All Rain Rates	$Z = 444R^{1.08}$
Westerly	R $\geq$ 10 mm hr^{-1}	$Z = 426R^{1.11}$
All	All Rain Rates	$Z = 465R^{1.08}$
All	R $\geq$ 10 mm hr^{-1}	$Z = 470R^{1.10}$

Table 3.3: Values of polarimetric measurements for various precipitation types (adapted from Doviak and Zrnić, 1993).

	Z_h (dBZ)	Z_{dr} (dB)	K_{dp} (deg km^{-1})	LDR (dB)
Drizzle	<25	0	0	<-34
Rain	25 to 60	0.5 to 4	0 to 10	-27 to –34
Snow, dry, low density	<35	0 to 0.5	0 to 0.5	<-34
Crystals, dry, high density	<25	0 to 5	0 to 1	-25 to –34
Snow, wet, melting	<45	0 to 3	0 to 2	-13 to –18
Graupel, dry	40 to 50	-0.5 to 1	-0.5 to 0.5	<-30
Graupel, wet	40 to 55	-0.5 to 3	-0.5 to 2	-20 to –25
Hail, <2cm, wet	50 to 60	-0.5 to 0.5	-0.5 to 0.5	<-20
Hail, >2cm, wet	55 to 70	<-0.5	-1 to 1	-10 to –15
Rain & Hail	50 to 70	-1-1	0 to 10	-20 to –10

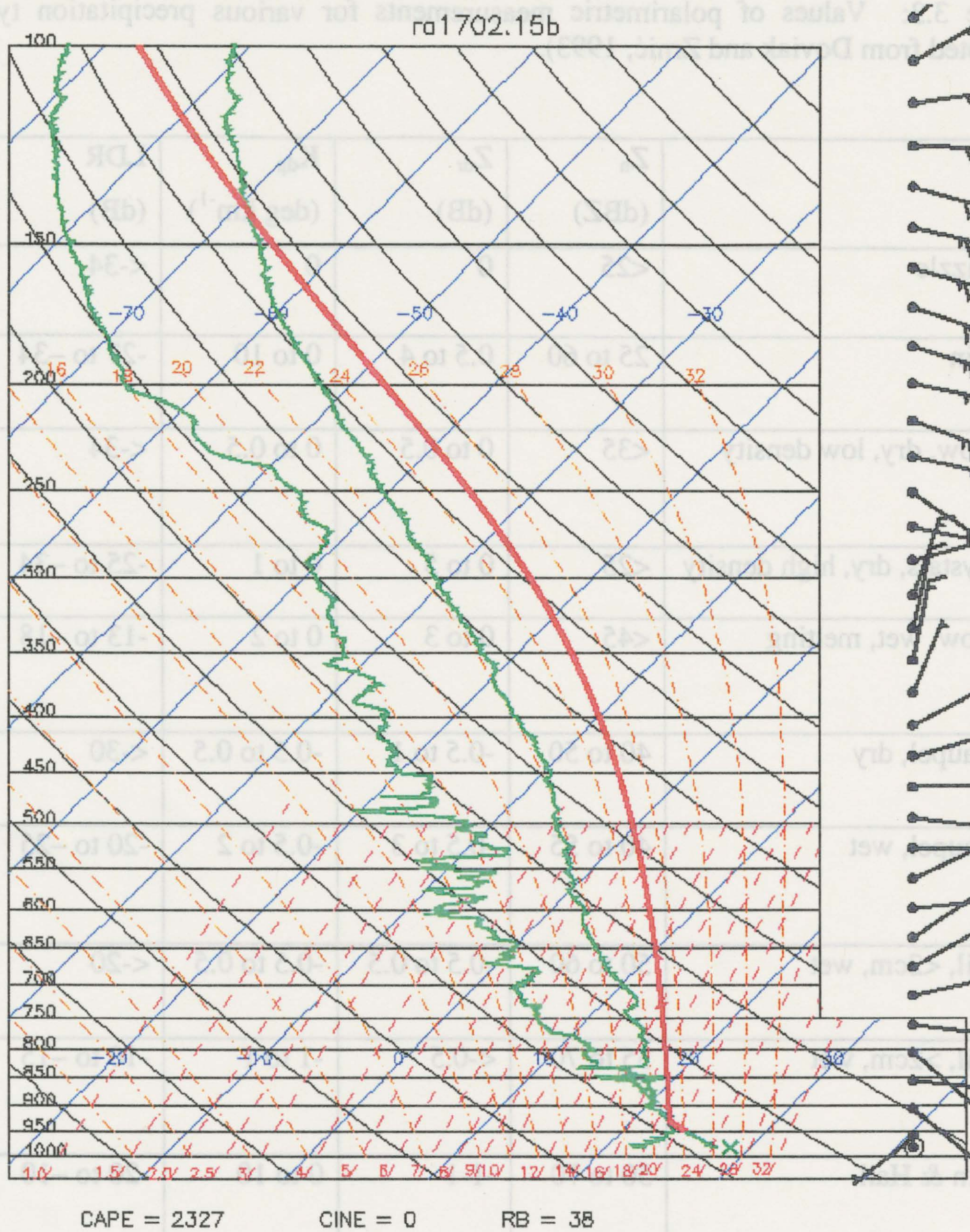

Figure 3.1: Skew-T/Log-P diagram of the troposphere at 15 UTC on 17 February 1999.

(a)

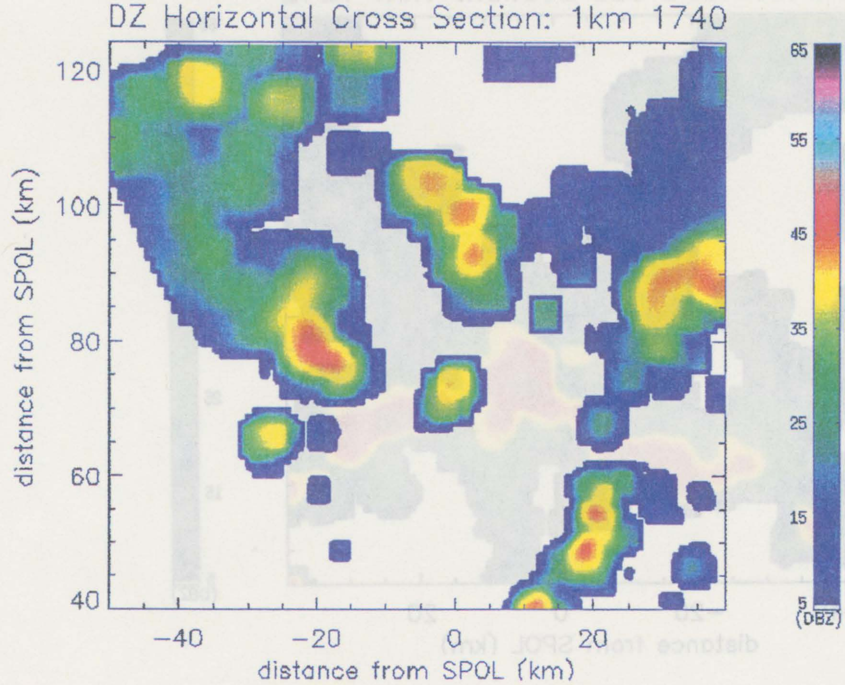

(b)

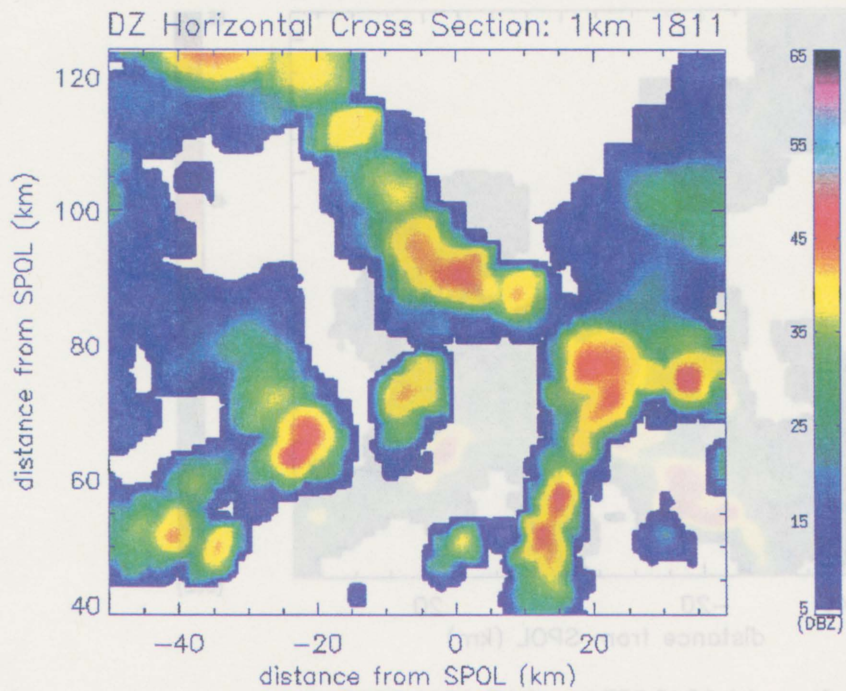

Figure 3.2: Horizontal cross-sections of reflectivity at 1 km at (a) 1740 UTC (b) 1811 UTC.

(c)

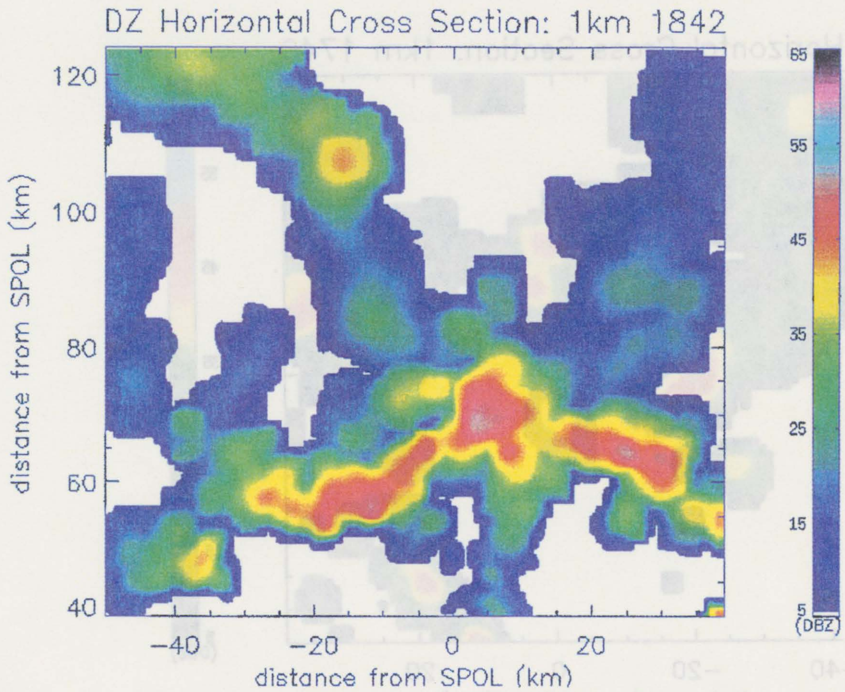

(d)

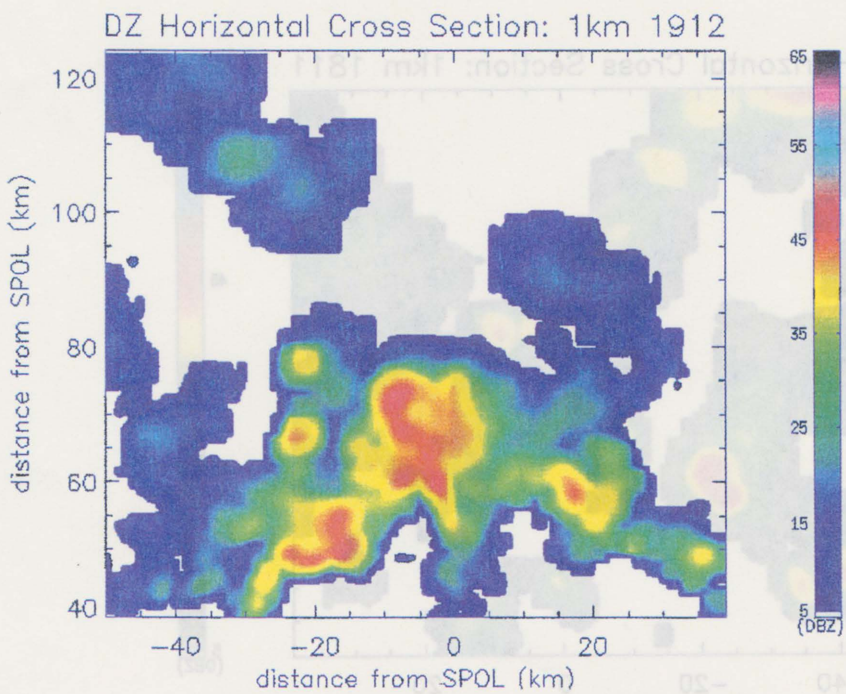

Figure 3.2: Results at (c) 1842 UTC and (d) 1912 UTC.

(e)

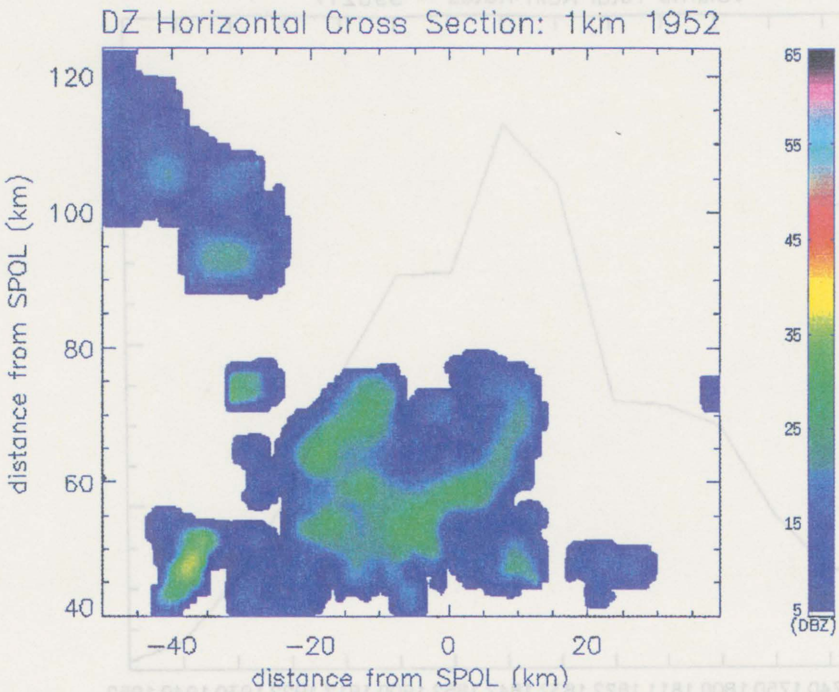

Figure 3.2: Results at (e) 1952 UTC.

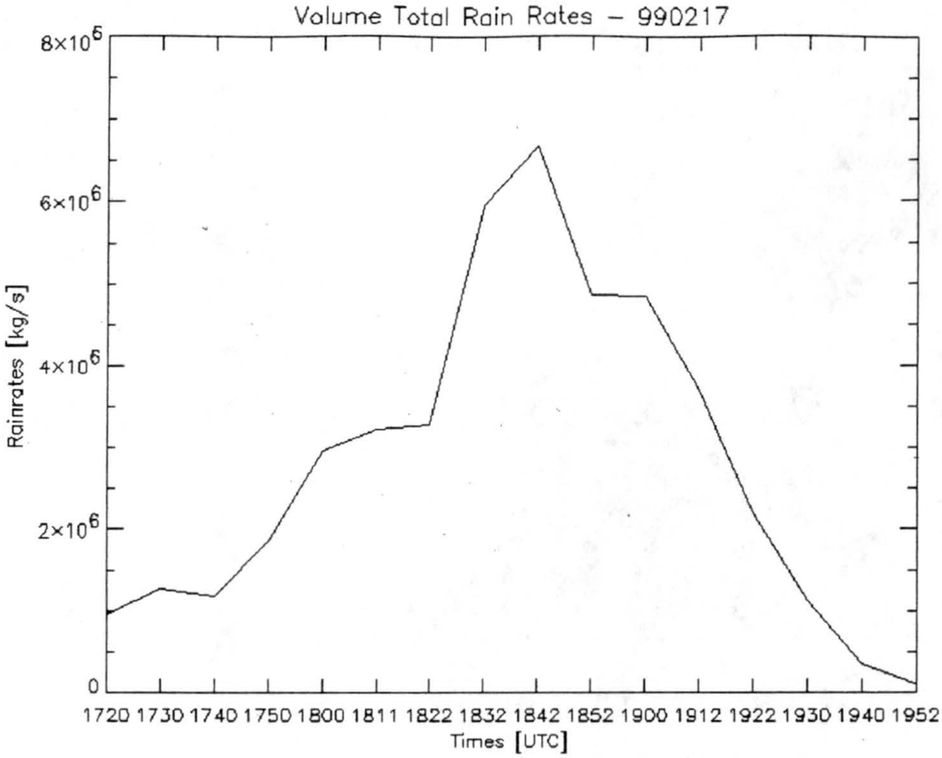

Figure 3.3: Rain rates in kg s^{-1} for each volume of 990217.

(a)

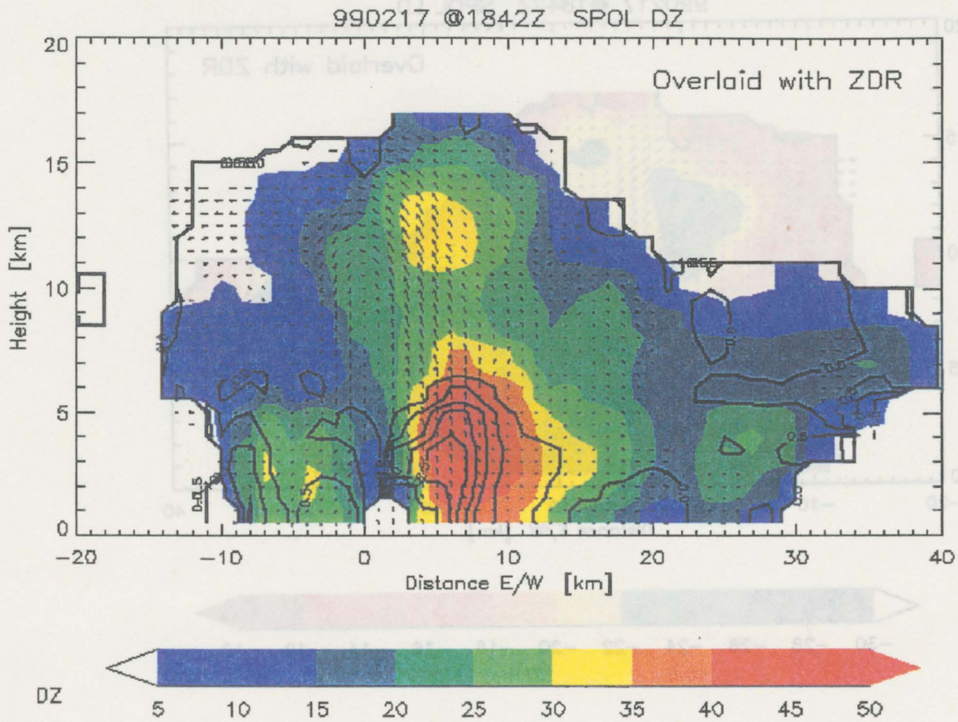

(b)

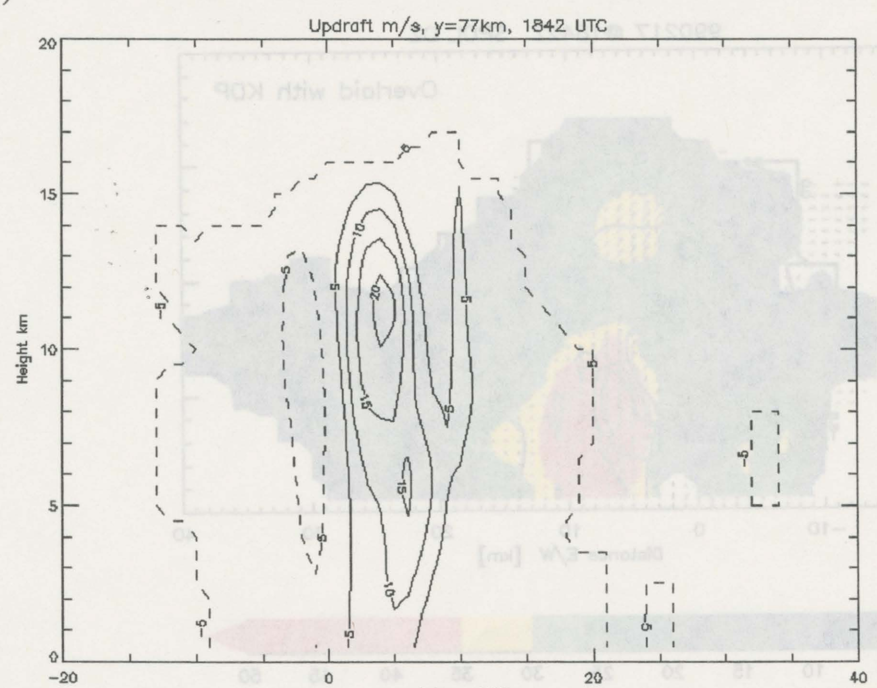

Figure 3.4: Characteristics along y = 77 km cross-section on 17 February at 1842 UTC. (a) Reflectivity in colored contours overlaid with Z_{dr} in 0.5 dB intervals; Arrows represent vertical velocities. (b) Vertical velocity in m s^{-1}.

(c)

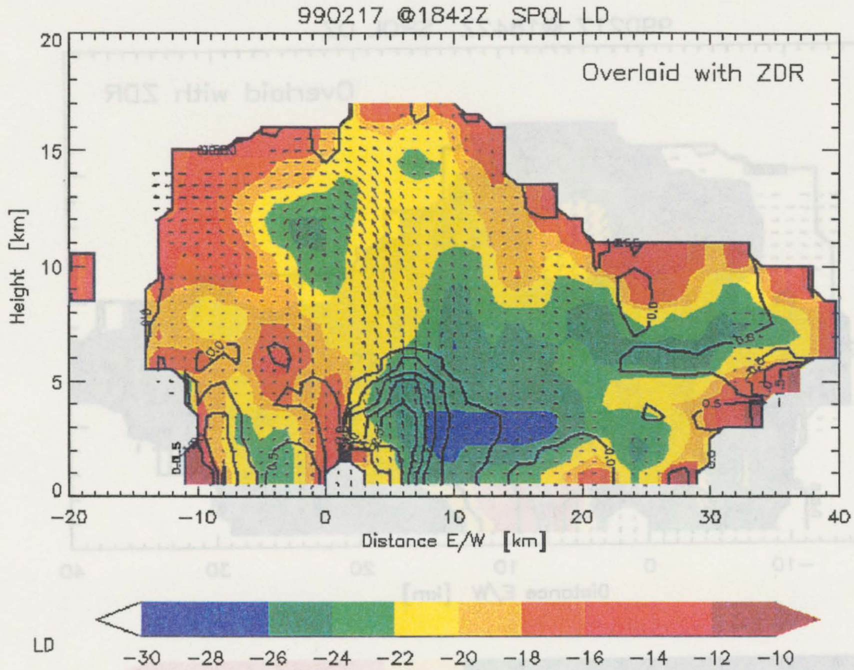

(d)

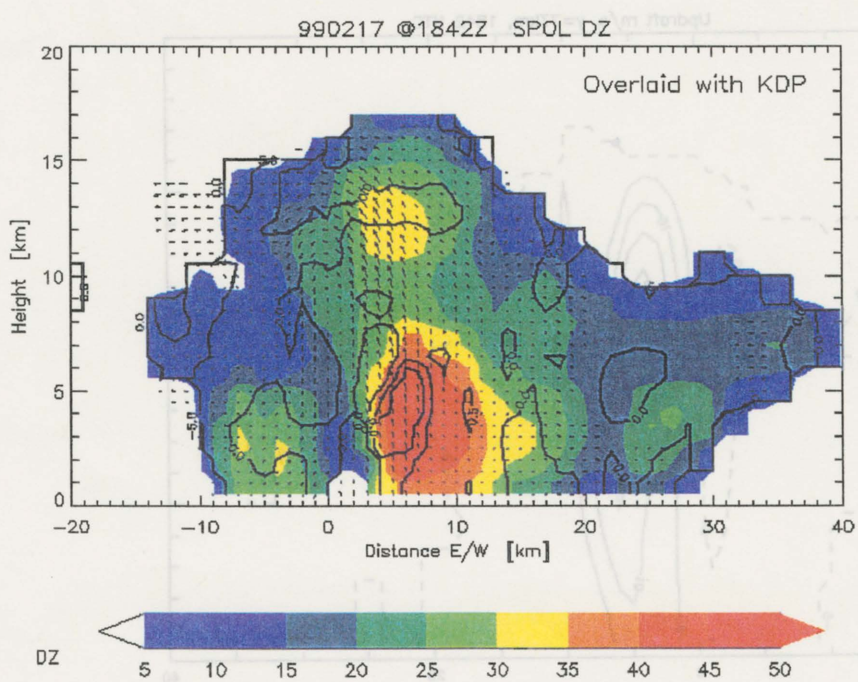

Figure 3.4: (c) LDR in colored contours overlaid with Z_{dr} in 0.5 dB intervals; Arrows represent vertical velocities. (d) Reflectivity in colored contours overlaid with K_{dp} in 0.5 deg km^{-1} intervals; Arrows represent vertical velocities.

(e)

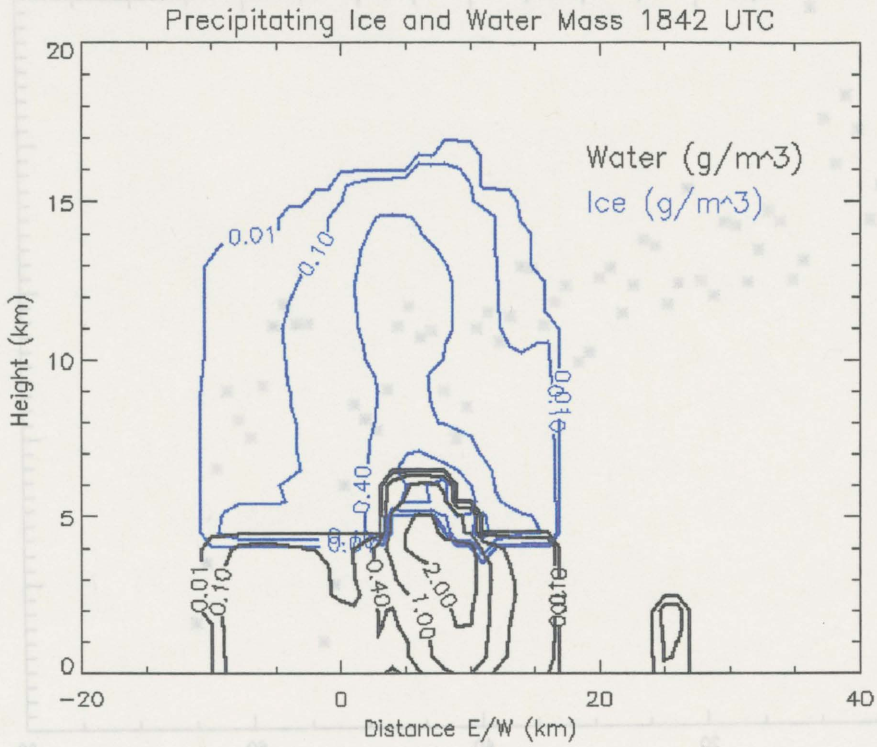

Figure 3.4: Results for (e) Precipitating ice and water masses in g m^{-3}. Contours at 0.01, 0.1, 1.0 and 2.0 g m^{-3}.

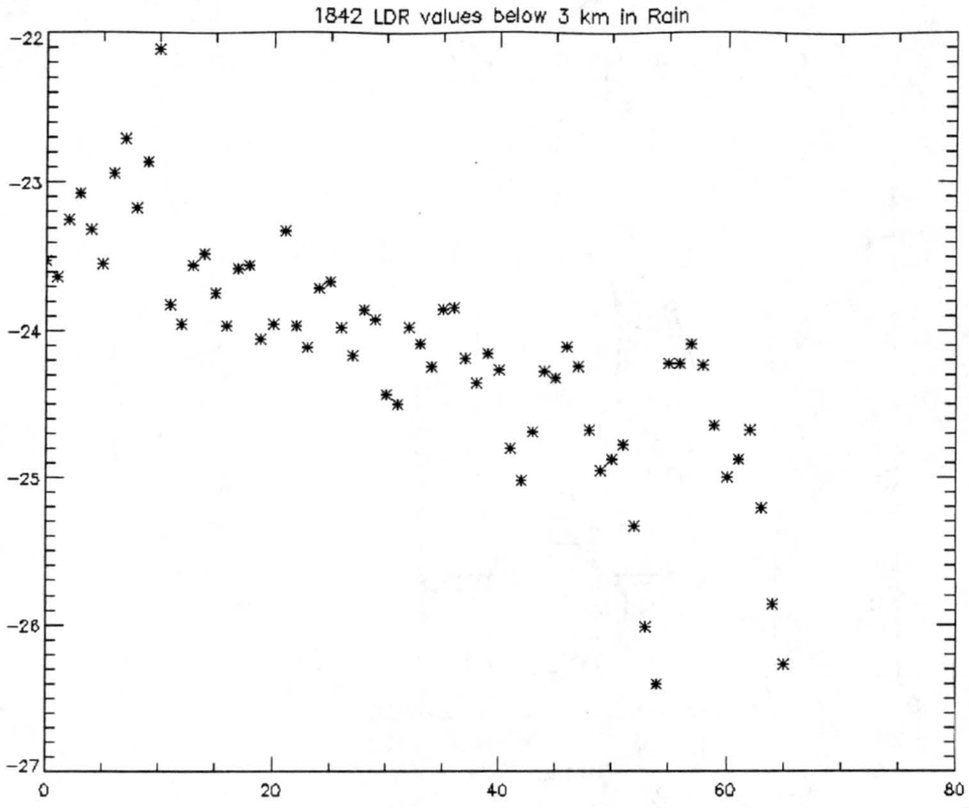

Figure 3.5: Scatter plot of LDR values below 3km in a rain region.

(a)

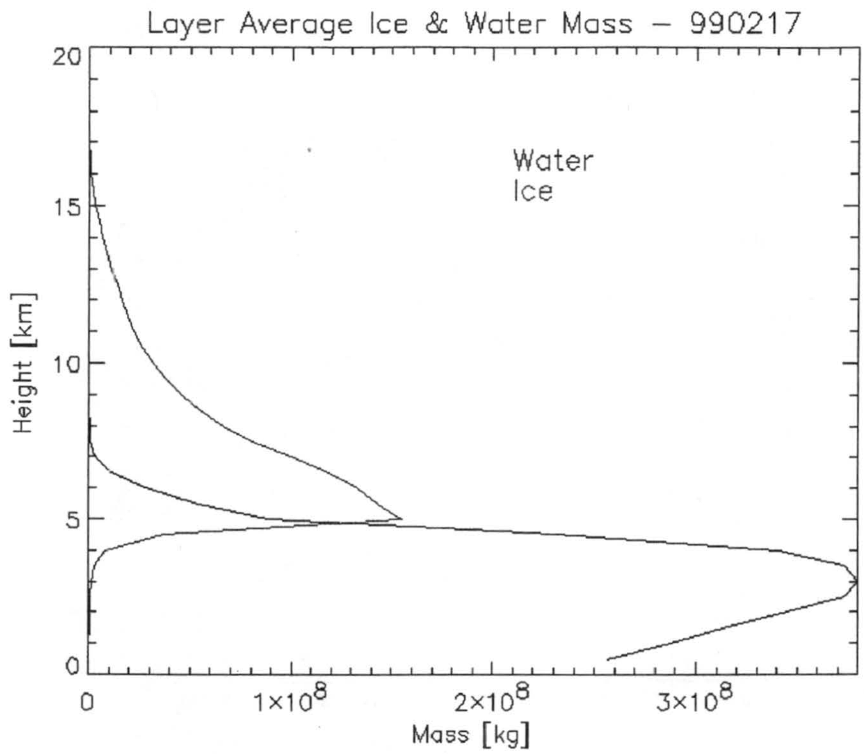

(b)

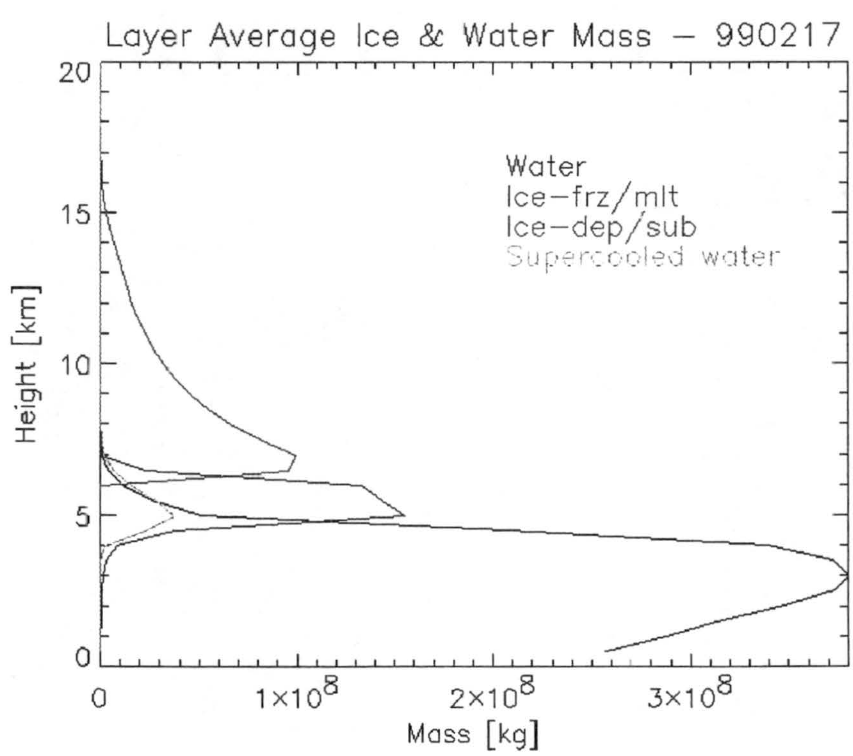

Figure 3.6: Layer average ice and water masses for all volumes of 990217. (a) Subdivided into only ice and water masses. (b) Masses associated with growth regimes previously defined.

(a)

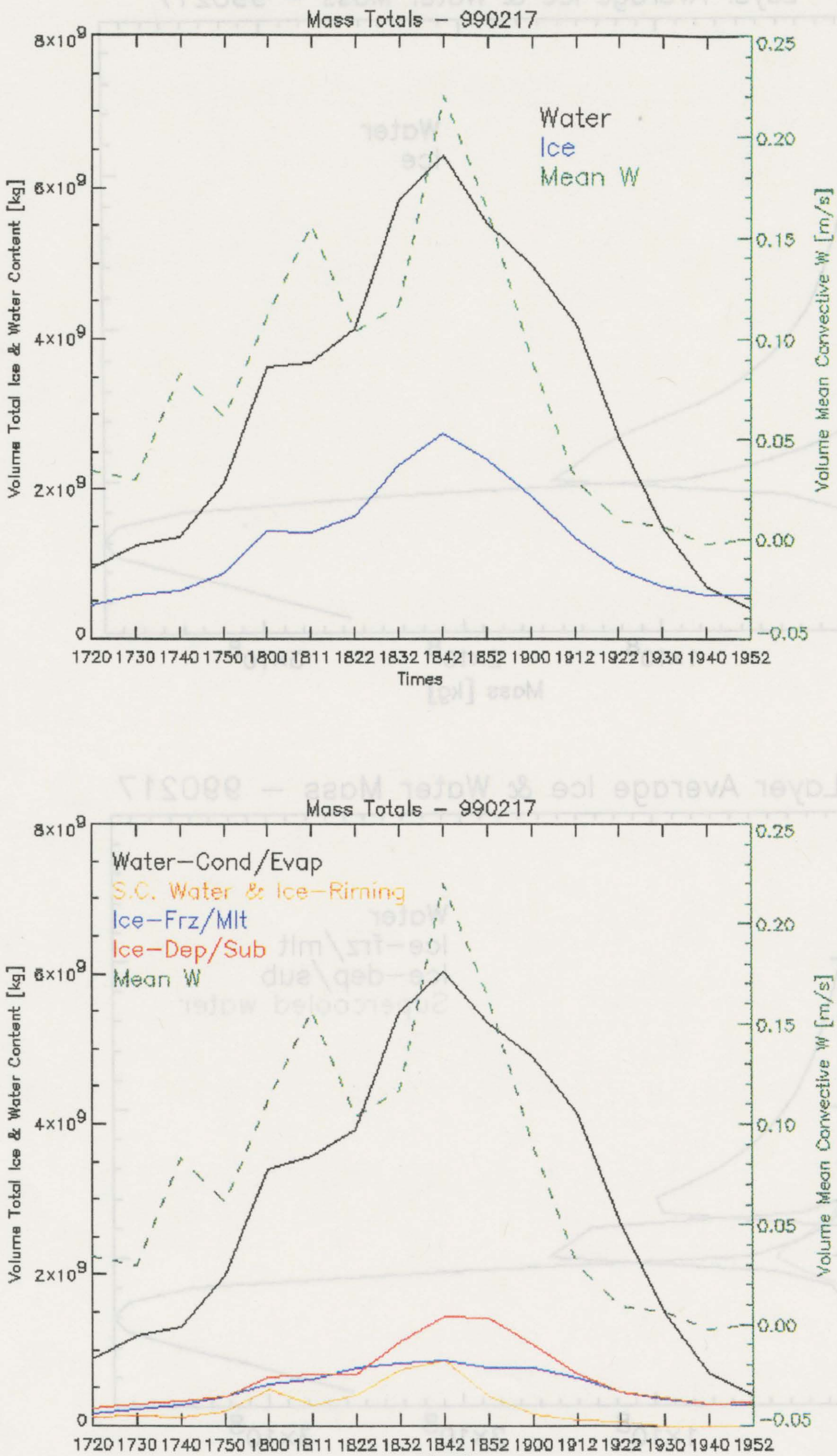

Figure 3.7: Mass totals as a function of time for 990217 overlaid with volume mean convective vertical velocity, w. (a) Subdivided into ice and water masses. (b) Masses associated with growth regimes as previously defined.

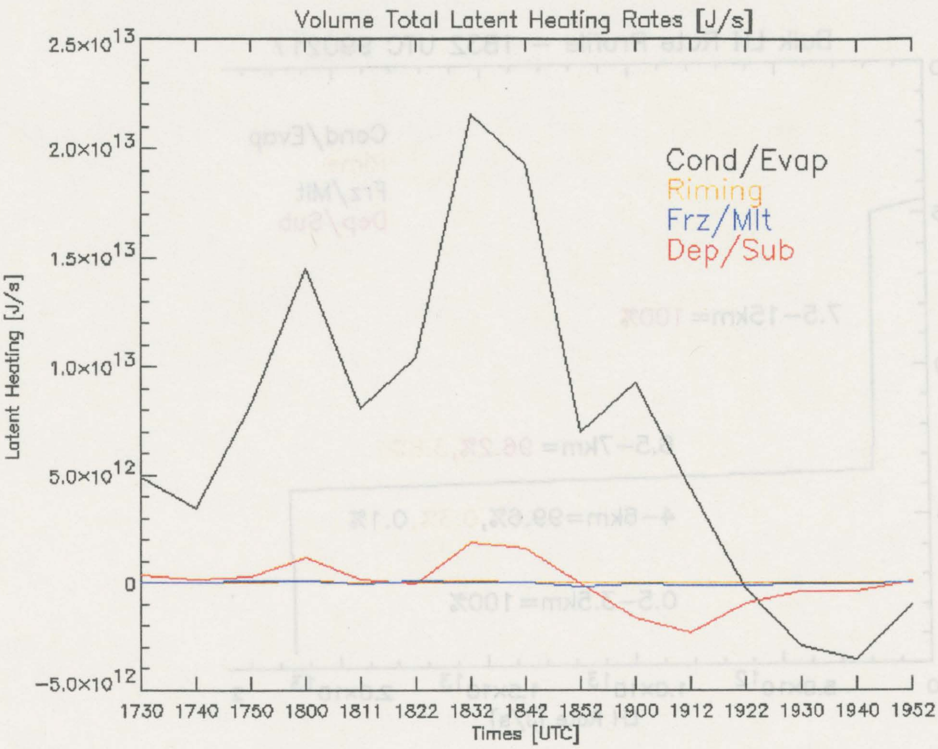

Figure 3.8: Latent heating rates estimated over time on 990217.

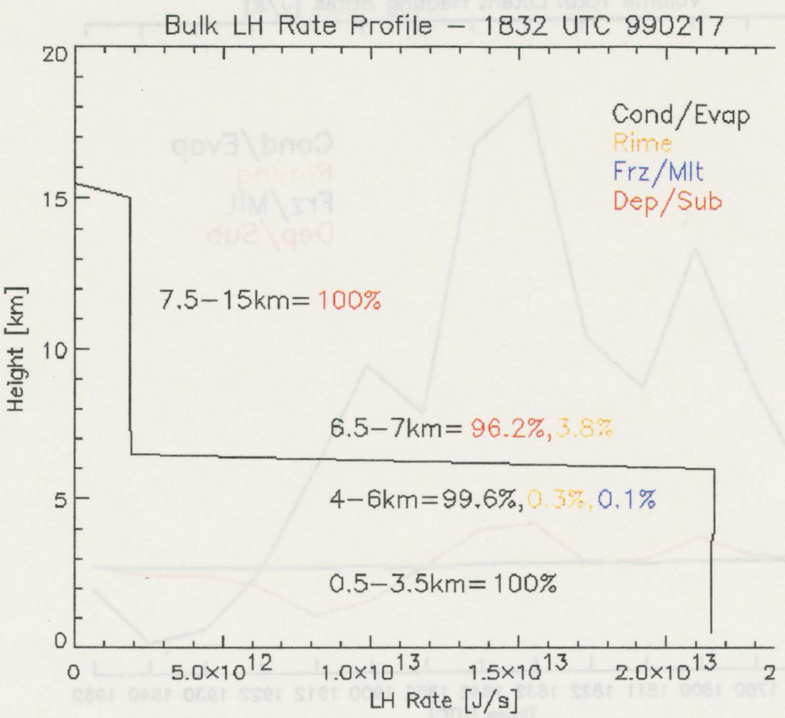

Figure 3.9: Bulk profile of latent heating rates at 1832 UTC, growth stage in the storm. Percentages correlate with colored phase change denoted at top-right of figure. Layers at 0.5 km resolution begin at level mentioned in figure.

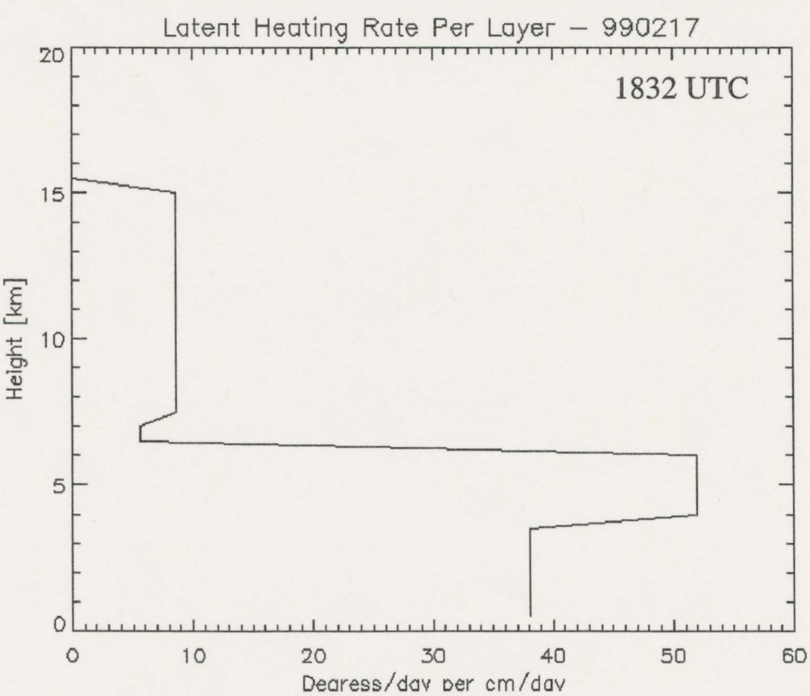

Figure 3.10: Bulk profile of latent heating rate per layer at 1832 UTC normalized by an instantaneous rain rate of 22 cm day^{-1} and rain rate area of 2384 km^2. Average densities were used for each bulk layer denoted in Figure 3.9.

(a)

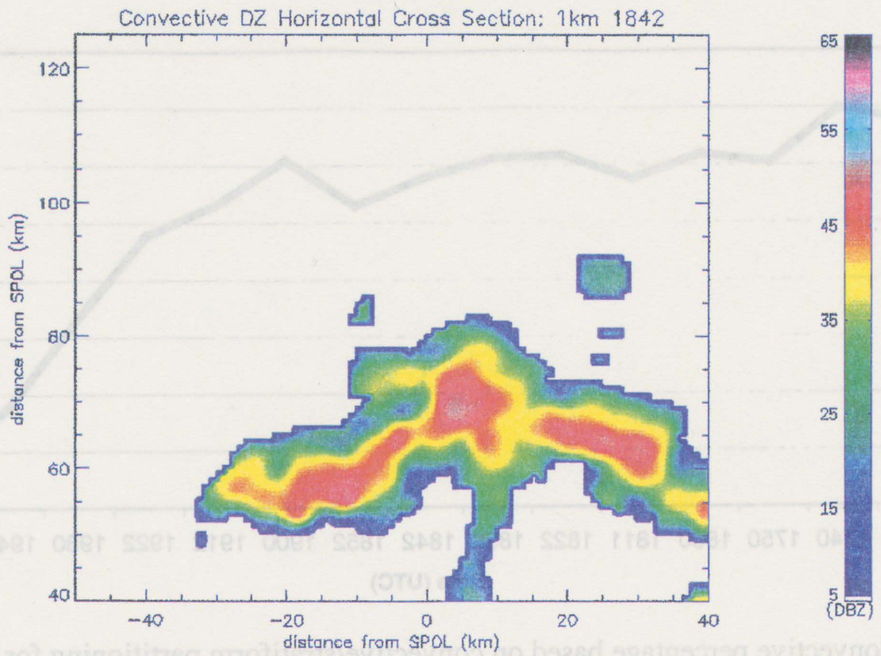

(b)

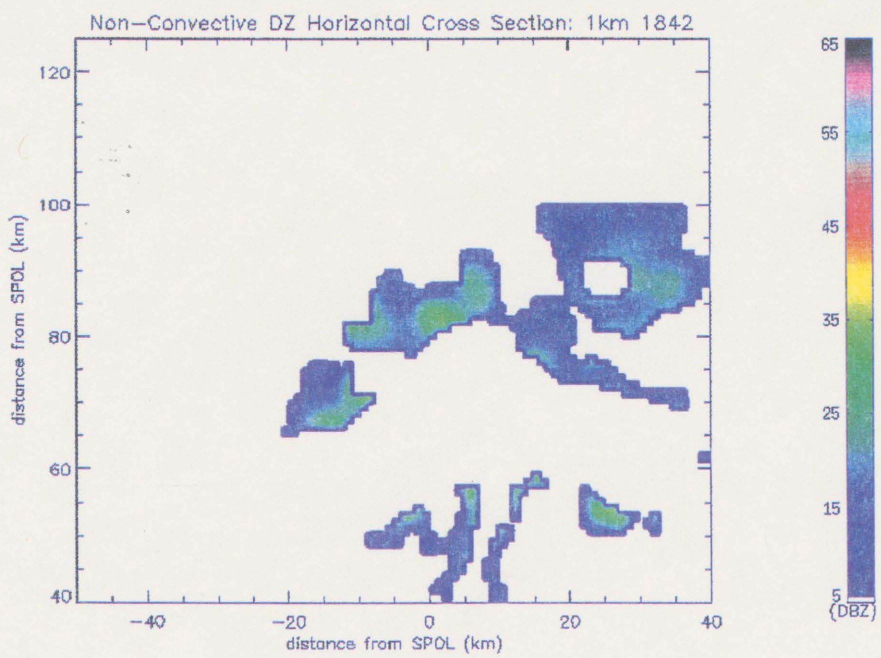

Figure 3.11: Example of convective/stratiform partitioning for reflectivity at 1km AGL and 1842 UTC for (a) convective reflectivities and (b) stratiform reflectivities.

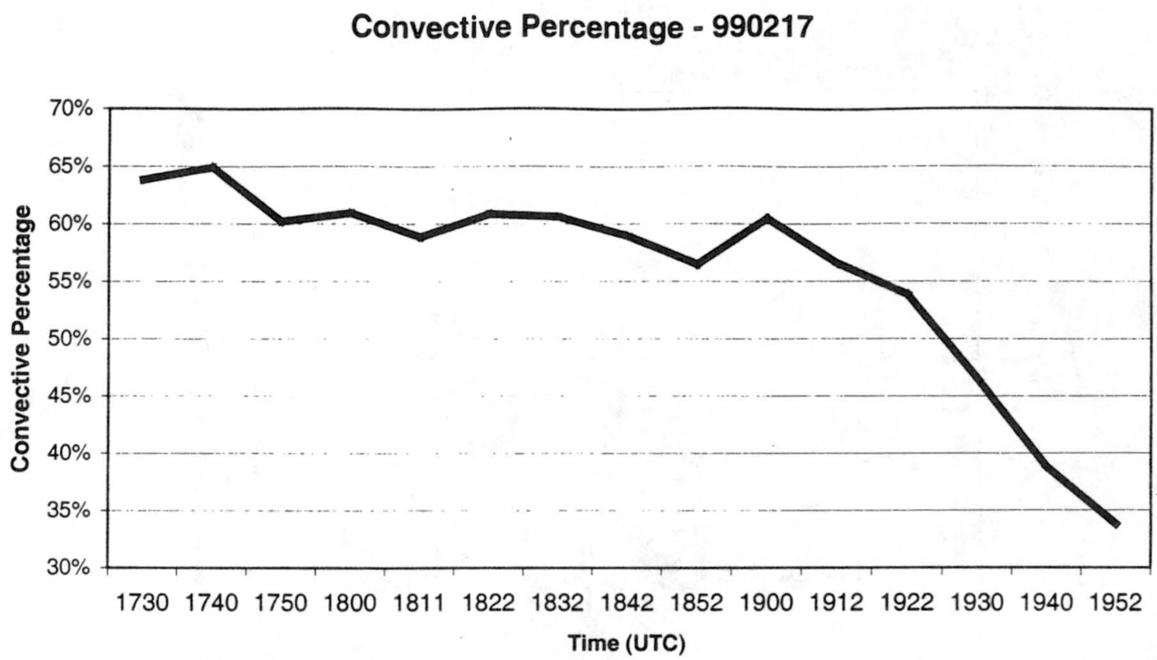

Figure 3.12: Convective percentage based on convective/stratiform partitioning for 990217.

(a)

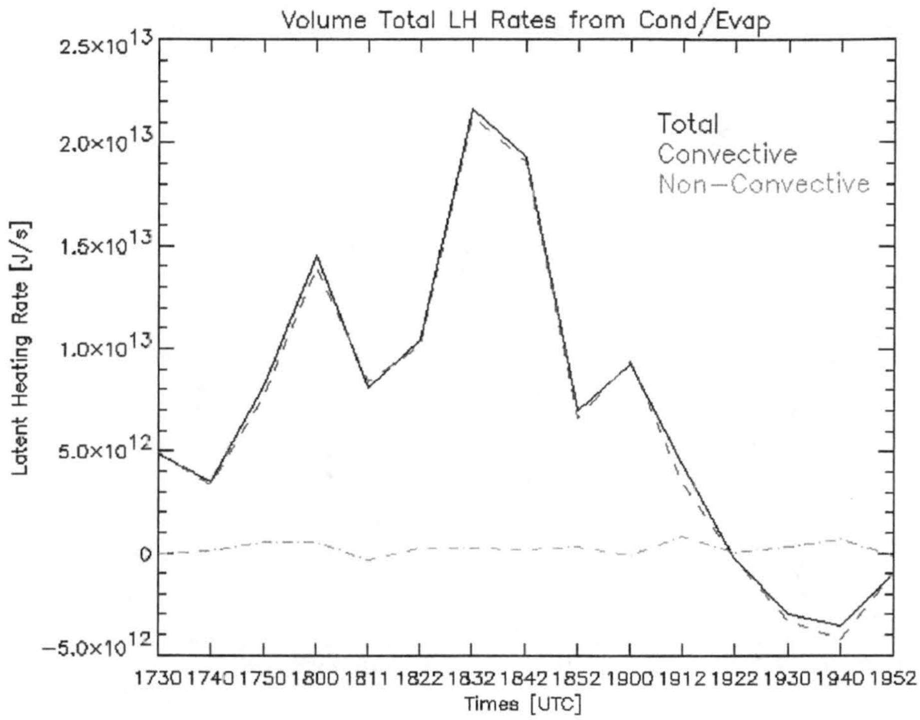

(b)

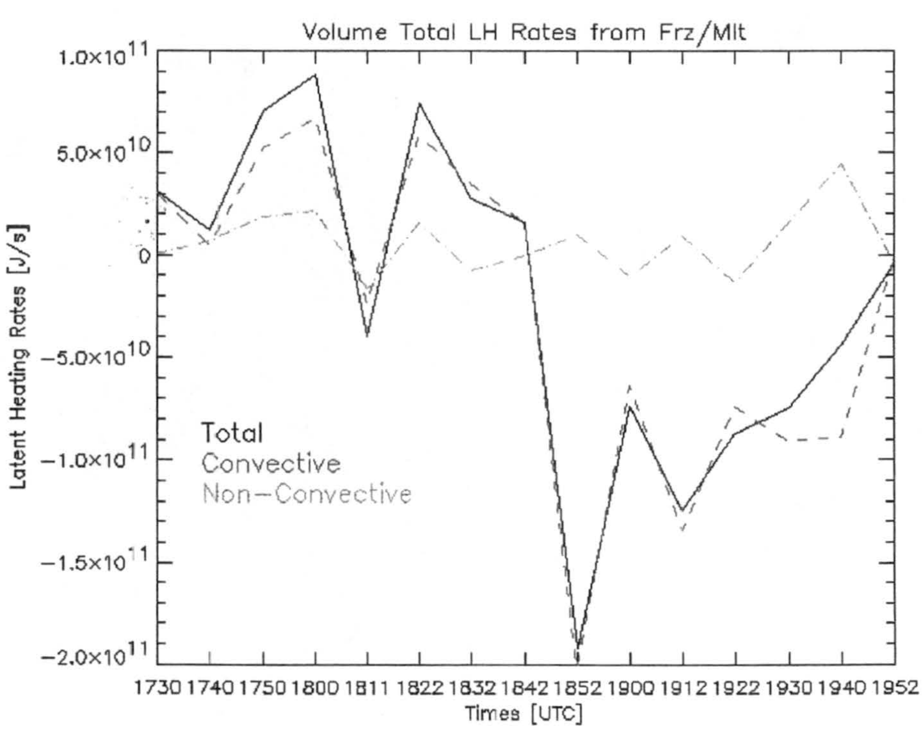

Figure 3.13: Latent heating rates vs. time, partitioned for convective and stratiform components due to (a) condensation and evaporation and (b) freezing and melting.

(c)

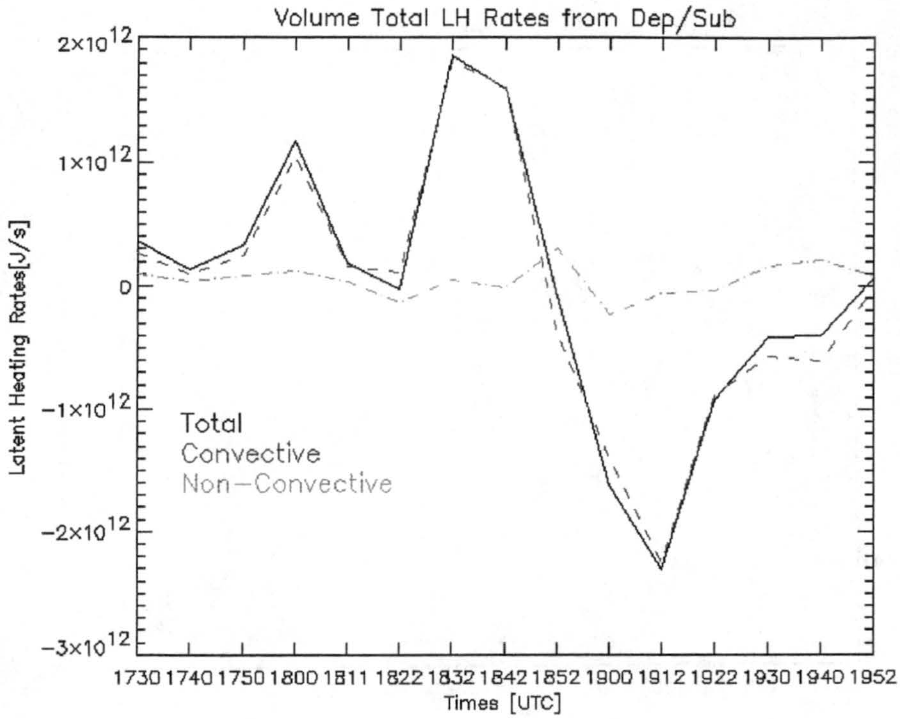

Figure 3.13: Results for (c) deposition and sublimation.

CHAPTER FOUR

23 February 1999 case study

The 23 February 1999 case study was a strong convective event that occurred at the beginning of a westerly phase period. Widespread convection began relatively early in the day (1500 UTC or 100 local time) across most of the coverage area. A different set of convective cells developed to the east of the dual-Doppler domain and decayed just before the convection studied in this chapter began. This prior convection may have played a role in the quick demise of this MCS. This study's cellular convection emerged from a line of cumulus clouds oriented 120 km north-northwest to about 40 km north of the S-Pol radar at 1918 UTC (1318 local time). The individual cells continued along their southeastward track until their cold pools merged to form a solid line of convection that extended almost 100 km at 2002 UTC. This is approximately when full volume coverage began by both the S-Pol and TOGA radars. S-Pol had previously been sampling the decaying convection to its east. This coverage remained throughout the decline of the system by 2130 UTC. Instantaneous rain rates near 70 mm hr^{-1} were found in regions of this convective line. A study of the atmospheric conditions, storm evolution, kinematics, microphysics and latent heating rates for this case follows.

4.1 Atmospheric Conditions

Figure 4.1 shows a Skew-T/Log-P diagram at 1500 UTC for this case. Note the northwesterly winds from the surface to 600 hPa with moderate wind speeds of 5 to 10 kts. Above that, the winds are measured at calm until 525 hPa when they switch direction to southeasterly. From that level to 275 hPa, the winds are extremely light ranging from 3-5 kts. The winds maximize at 25 kts at 160 hPa (~14 km). This is near the maximum level the convection will reach at 2000 UTC. There is abundant moisture from the surface up to 450 hPa (significantly higher than the easterly case), with smaller relative humidities above that. This moisture profile difference is commonly seen in TRMM-LBA case studies (Halverson et al., 2001).

The CAPE is 1589 J kg^{-1}, which is higher than the average CAPE (1165 J kg^{-1}) for this westerly period (Halverson et al., 2001). The CIN (or CINE as in Figure 4.1) was non-existent at this time, which means the troposphere did not need much triggering for convective initiation. The bulk Richardson number, R_i (or RB as in Figure 4.1), is 752. This value is too high to compare with mid-latitude case studies. It is too high because the shear in the 0.5 to 6 km layer is minimal for this case. So the CAPE dominates the bulk Richardson number. For tropical studies, it may prove more useful to use a larger depth to calculate this index or simply note that the R_i is non-representable of these tropical conditions.

4.2 Storm Evolution

4.2.1 Dual-Doppler Analysis

Figure 4.2 shows horizontal reflectivity cross-sections at 1km from the S-Pol radar. Recall that full volume coverage did not begin until 2002 when the storm was already mature. Reflectivities exceeded 45 dBZ at this time (Figure 4.2-a). This line of cells moved as a group at 8 m s^{-1} (20 kts) from 280 degrees. This was the environmental wind speed at 800 hPa, yielding the apparent storm steering level (Figure 4.1). By 2019 UTC, the maximum reflectivity has increased to 52 dBZ (Figure 4.2-b). The southern most part of the line broke off by 2039 UTC (Figure 4.2-c) and began to show notable signs of decay by 2100 UTC (Figure 4.2-d). These two figures also show an increase in low reflectivity area coverage at this height of 1 km AGL. Finally, Figure 4.2-e shows the decline of most of the northern component as well by 2130 UTC. By this time the MCS had moved into the area associated with the previous convection. Hence, the environment may not have been as favorable to sustain convection. More stratiform echo, also associated with this MCS, was observed to the north of the domain observed by the S-Pol radar. The intense updraft regions had echo tops reaching 16 km, but most remained below 12 km.

Mean vertical velocities in the convective region are shown in Figure 4.6. They range from 0.5 cm s^{-1} during the system's decline to nearly 11 cm s^{-1} at its maximum (2019 UTC). Most updrafts contained maximum vertical velocities of 5-10 m s^{-1}, but a few exceeding 15 m s^{-1} were diagnosed. These vertical velocities are similar to values found in the easterly case, and tropical convection in general (LeMone and Zipser, 1980; Jorgensen and LeMone, 1989; Lucas et al., 1994). The probability of finding a 15 m s^{-1} vertical velocity maximum is less than 1% according to Jorgensen and LeMone (1989). The vertical velocity structure was somewhat different than in the easterly case. The more intense, easterly MCS had stronger vertical velocities at lower levels with a local maximum occurring just above the freezing level at times (Figure 3.4-b). In general, the westerly case had a much smoother vertical velocity profile, but the velocity magnitudes were similar (Figure 4.4-b). Since this westerly case was more convective, had stronger vertical velocities and higher CAPE than other westerly cases studied (Rutledge et al., 2000; Cifelli et al., 2001; Halverson et al., 2001), it seems reasonable the vertical velocity structure would somewhat resemble the easterly case. It is likely that convectively stronger westerly events occur in the beginning of westerly phase periods, as in this MCS.

There are some notable differences in the vertical velocity structure of this tropical convective line compared to other tropical studies. Roux et al. (1984) and LeMone (1983) found tropical squall lines to be front-fed from a cold, density current with the maximum vertical velocities along the leading gradient in reflectivity. Even though the dynamics of these more expansive squall lines do not match this case, the magnitude of the velocities did agree well with this study (10-15 m s^{-1}). They also found rear to front flow behind the main updraft below 4 km. This case is almost completely rear fed and has stronger rear to front flow extending up to 5 km. At some locations, the horizontal rear inflow exceeds 5 m s^{-1} (not shown). By 2100 UTC, the strong rear to front flow pushes through most updrafts and continues ahead of the leading convective line. This cut off the updraft from below and forced the system to decay.

4.2.2 Polarimetric Analysis

To calculate rain rates, the Carey et al. (2001) polarimetrically tuned Z-R relationships were used as shown in Table 3.2. The "all rain rates" westerly relationship was used for stratiform precipitation for this case and the westerly $R \geq 10$ mm hr^{-1} relationship was used for convective precipitation. The volume total rain rates for each time period were then calculated using reflectivity at 1 km (Figure 4.3). The rain rates were already strong when coverage began at 2002 UTC valuing 2.6×10^6 kg s^{-1} for the entire grid domain, or 2.7 mm hr^{-1} average for each grid space. The maximum was reached at 2019 UTC with an instantaneous rain rate of 4.1×10^6 kg s^{-1} for the entire grid domain, or 4 mm hr^{-1} average for each grid space. Recall this was the time of maximum convective mean vertical velocity (Figure 4.6). From this point until 2130 UTC, the rain rates steadily declined.

A vertical cross-section through one of the main updrafts at 2029 UTC is shown in Figure 4.4. The cross-section was taken at y = 53 km. The reflectivities and Z_{dr} (differential reflectivity) values are shown in 4.4-a. Reflectivities exceed 40 dBZ up to 6 km in the updraft region. There is a weak Z_{dr} column co-located with the maximum in reflectivity extending just above the freezing level at 5 km AGL. This structure indicates oblate drops being lofted into the storm as described in Sec. 3.2.2. Other westerly regime case studies have observed weak Z_{dr} columns, as the convection was generally not very intense during westerly phase periods (Rutledge et al., 2000; Cifelli et al., 2001). This strong storm has an echo top of 15 km and a significant stratiform region is seen to the west of the initial updraft.

Vertical velocity magnitudes are shown in Figure 4.4-b. The updraft is obviously titled rearward in the vertical as found in several other tropical studies (Roux et al., 1984; Cifelli and Rutledge, 1994; Rutledge et al., 2000; Cifelli et al., 2001; and others). The maximum is centered around 11 km AGL. As seen in the easterly case, this vertical velocity maximum aloft is often observed, as water "unloading" and the latent heat released makes the parcel more buoyant above the freezing level (Petersen et al., 1999).

Figure 4.4-c shows the same vertical cross-section with the linear depolarization ratio (LDR) in colored contours and Z_{dr} in black contours. Recall that the LDR values were too high by approximately 3 dB due to slightly non-orthogonal H, V polarization bases as discussed in Sec. 3.2.2. No LDR cap directly above the Z_{dr} column is present in this cross-section to indicate substantial freezing above the freezing level. Some LDR caps were observed in other areas of this MCS, however (not shown).

Specific Differential Phase (K_{dp}) is shown in Figure 4.4-d. The only real feature is the column of moderate K_{dp} (>1.0 deg km^{-1}) found in the same location as the Z_{dr} column. Since K_{dp} is only sensitive to oblate water drops, this column is indicative of the large drops being lofted into the storm (consistent with the inferences from Z_{dr}). Notice how the K_{dp} column does rise above the freezing level (5 km) very slightly, indicating a small region of supercooled drops. It is likely that some of the water is falling out of the storm as precipitation, as the updraft is only 5 m s^{-1}.

Using the Z_{dp} technique (c.f. Sec. 2.4.1), cross-sections depicting water and ice mixing ratios can also be determined. Figure 4.4-e shows the result along the same cross section described above. An area of mixed phase in Figure 4.4-e can easily be seen by the overlapping contours from 4 to 5 km AGL. This could be due to a combination of factors. As evidenced by the K_{dp} feature, some supercooled drops could be intermixed with ice near 5 km. It is also probable that some precipitation ice is falling through the updraft and melting below 5 km. This is shown by the fact that Z_{dr} is small above 5.5 km, but then becomes large below the freezing level. Also, no LDR cap is present to indicate the substantial freezing aloft that would have to occur if all the drops were being lofted into the storm. In addition, water mixing ratios below the freezing level are larger than in the easterly case. This is more evidence that melting processes are occuring and contributing to the large water mixing ratios. In order to create such large mixing ratios without having coincidently large differential reflectivities (Z_{dr}'s), the diameters of the drops must be small (otherwise they would become oblate and raise Z_{dr}). Smaller drop diameters were more prevalent in westerly regime cases as seen in Figure 1.3-b (Carey et al., 2001).

Bulk hydrometeor classification can also be done using a reference table (Table 3.3). The updraft region from x = 10 to x = 16 km and up to 5 km in the vertical had reflectivities > 40 dBZ, Z_{dr}'s > 1.0 dB, K_{dp}'s > 0.5 deg km^{-1} and LDR's centered around –27 dB (corrected). This corresponds with rain from Table 3.3. Another region of polarimetric interest is between x = -5 and x = 1 and between 5 and 7 km in the vertical. Reflectivities are less than 20 dBZ and LDR is around –27 dB (corrected). There is hardly any K_{dp} signal and Z_{dr}=0 in that area. This corresponds to dry, high-density crystals. These crystals are in a region of mesoscale downdraft and are approaching the melting level. They will likely contribute to the rain rate at that location upon melting.

This polarimetric analysis discussed that the 23 February 1999 westerly case did have strong enough convection to support some weak Z_{dr} columns and LDR caps (not shown). A mixed phase region was also observed along this cross-section although it was probably in transition to a decaying phase.

4.3 Water and Ice Partitioning

4.3.1 Masses of Water and Ice

The water and ice partitioning as described in Sec. 2.4.1 can provide further insights into storm structure and evolution. Figure 4.5 shows the average mass profile for the radar volumes available for this case. Figure 4.5-a shows the masses subdivided into ice and water. Recalling that the data are at 0.5 km resolution in the vertical, it is easily seen that most of the ice is found between 4.5 and 14 km with maximum values near 1.5 x 10^8 kg. Water is found from 0.5 km to 6 km AGL with magnitudes on the order of 10^8 kg. Approximate mixing ratios for ice and water can be seen in Figure 4.4-e. Figure 4.5-b further shows the categorization of masses used to estimate the latent heating rate. The ice mass changes due to deposition and sublimation begin at 6.5 km (location of -10° C isotherm) and continue to the average storm top of 14 km. The ice mass changes due to freezing and melting occur from the layer beginning at 6 km down to 4 km on average. Water is found from the lowest resolution elevation (0.5 km) to 5.5 km and supercooled water available for the riming process is located between 4 and 6 km AGL. Stith et al. (2001) did find significant amounts of supercooled water at temperatures > -7° C (~6 km AGL) with some trace amounts up to –18° C (~8 km AGL) during TRMM-LBA, although the aircraft did not sample the most robust convection.

A depiction of how these masses changed as the storm evolved is shown in Figure 4.6-a. Clearly, the water mass (68%) dominates the ice mass (32%) at 2029 UTC. However, at 2120, the water mass percentage decreases to 62%. This figure also shows the mean convective vertical velocities in m s^{-1} as previously described in Sec. 4.2.1. The vertical velocity curve seems to lead the mass curves. This is reasonable as stronger vertical velocities would allow for more mass to form and remain in the storm and weaker velocities would allow significant mass to fall out of the storm. Figure 4.6-b further shows the categorization of masses used to estimate the latent heating rate. The ice mass used for deposition and sublimation latent heating estimation dominates the other two ice-related curves. It grows throughout the beginning volumes and reaches its maximum of 1.85 x 10^9 kg at 2029 UTC. The "freezing/melting" curve lies just below it, but does not change shape significantly. The "riming" curve reaches a maximum at 2019 UTC, but does exhibit a non-zero value until the very last volume of 2130 UTC. This is a smaller, but much broader curve than in the easterly case. Note this curve's maximum is co-located with the vertical velocity maximum. This is reasonable as a stronger updraft is necessary to loft supercooled drops above the freezing level.

4.3.2 Associated Latent Heating Rates

The latent heating rates, estimated as described in Sec. 2.4.3, are shown in Figure 4.7 for the volumes available for this storm. The condensation term dominates the latent heating rates throughout the times displayed. It reached its maximum at the first volume 2010 UTC and then slowly declined. The latent heating rate due to deposition/sublimation begins positive with deposition dominating sublimation, but switches to negative by 2039 UTC and remains that way until 2130 UTC. The latent heating rates due to freezing/melting and riming are too small to be compared on this graph; they are on the order of 10^{10} J s^{-1}.

A bulk latent heating vertical profile is shown in Figure 4.8 for 2010 UTC, a growth period in the storm. Recall that the latent heating due to changes in ice mass separates into deposition and sublimation above 6.5 km, and freezing and melting below. The levels for supercooled drops, condensation and evaporation were determined by a graph similar to Figure 4.5, but for the specific time of 2010 UTC. The percentages in the figure correspond to the change(s) of phase experienced at that particular level (or series of levels). Note how condensation dominates at low-levels and deposition at upper levels. The riming and freezing/melting processes do not add significantly to the latent heating rate with values never exceeding 0.3% of the total heating rate. Note this is a bulk profile in J s^{-1}, not in J s^{-1} km^{-1}. For example, the 1.22×10^{13} J s^{-1} latent heating rate on Fig. 4.8 is for the entire layer from 0.5 km to 4 km, not for each km within the layer.

Figure 4.9 shows the normalized latent heating rate per layer at 2010 UTC. The values in Figure 4.8 were divided by the specific heat of dry air (C_p), the average density for each layer, and the area associated with the rainfall (3607 km^2) and then converted to the proper units to get degrees of heating day^{-1} per cm day^{-1}. The instantaneous rain rate was 8 cm day^{-1} for this time period, which is considerably smaller than the easterly case (22 cm day^{-1}). The maximum heating occurs between 4.5 and 6.5 km with values exceeding 50 deg day^{-1} per cm day^{-1}. The minimum occurs above 6.5 km where the heating rate is dominated by deposition. This profile looks very similar to the easterly case in Figure 3.10. The magnitudes of the total latent heating rates for this westerly case are smaller than in the easterly case, but normalizing by the larger rain rate "volume" yields similar results. Again, this is a bulk profile for the levels described in Fig. 4.8 and the values are not for each km within the layers.

4.4 Convective / Stratiform Partitioning

4.4.1 Convective Percentages

The data were also partitioned into convective and stratiform components as described in Sec. 2.3.4. An example of how the reflectivity was partitioned is shown in Figure 4.10. At this level of 1 km, the storm appears to be dominated by convection (as in the easterly case), but this is not the case aloft. The convective percentage computed for the entire storm is shown in Figure 4.11. Recall that at the first time period plotted, this MCS is already mature and the convective fraction begins below 45% and climbs to the maximum of 51% at 2029 UTC. Then it gradually declines to 30% by 2130 UTC. These percentages are considerably smaller than in the easterly case, although more similar to findings in Cifelli et al. (2001) for both easterly and westerly cases (Figure 1.2).

4.4.2 Associated Latent Heating Rates

It is possible to gain more insight into the latent heating rates due to condensation, evaporation, freezing, melting, deposition and sublimation, as subdivided into convective and stratiform regions. Riming remained only in the convective components as seen in other TRMM-LBA and Kwajalein cases (Stith et al., 2001) and will not be discussed in this section. It must be noted that the latent heating rates in the stratiform component may be subject to a fair amount of uncertainty. The stratiform region does not contain much in the way of polarimetric signatures necessary to calculate the masses of ice and water. Therefore the estimation of these parameters may be subject to considerable error. However, the results found in both these case studies do seem reasonable as compared to aircraft in situ measurements during TRMM-LBA (Stith et al., 2001). Figure 4.12 shows the latent heating rates subdivided into convective and stratiform components. Recall that these figures allow the reader to visualize latent heating profiles in the vertical. The average levels for each thermodynamic process were shown in Figure 4.5.

Figure 4.12-a shows the latent heating rates from water mass changes due to condensation and evaporation. The convective component is the largest and is positive throughout all the volumes. Hence, the lower layers were heated via convection as shown in Houze (1997). Not having negative values on this curve

shows that evaporation was not as significant as in the easterly MCS. This could be because the troposphere was moister in this westerly case (Figure 4.1). The stratiform portion is smaller in magnitude and changes sign frequently throughout the lifetime of this event. Neither condensation nor evaporation is contributing much to the latent heating rate of this stratiform component compared to the convective component.

The latent heating rates due to freezing and melting are shown in Figure 4.12-b. The convective component again begins positive with freezing dominating the latent heating rate until 2029 UTC. These volumes represent growth stages where updrafts are building, thus allowing appreciable amounts of supercooled drops to be frozen. Therefore, it is reasonable that the latent heating rate due to freezing/melting is dominated by freezing in the convective component. Thus, the midlevels are also heated by convection early in the storm. The latent heating rate becomes negative when the storm starts to decline and melting dominates in the convective regions. The melting remains dominant through two attempts to return positive at 2050 and 2110 UTC. This may be when other convective cells try to become more robust by freezing drops, but it does not continue for long. The stratiform component, which is comparable in size to the convective component, does not exhibit much interpretable signal as it changes sign frequently.

The stratiform component of the latent heating rates due to deposition and sublimation have quite a meaningful interpretation (Figure 4.12-c). Almost throughout the entire event, the stratiform component is positive. This means there is heating aloft (> 6.5 km) in the stratiform regions. This agrees with Houze (1997), as there is a copious amount of deposition occurring behind the leading convective line adding to the growing stratiform region. This feature may arise as this westerly storm is more similar than the easterly storm to the ones used in Houze's study. Houze used events with large trailing stratiform regions and extensive brightbands and this westerly event had notably more stratiform echo than the easterly event. The convective portion is positive during the growth stages of the storm, showing that deposition heated that area aloft. After 2039 UTC, sublimation dominated the convective component during the storm's decline.

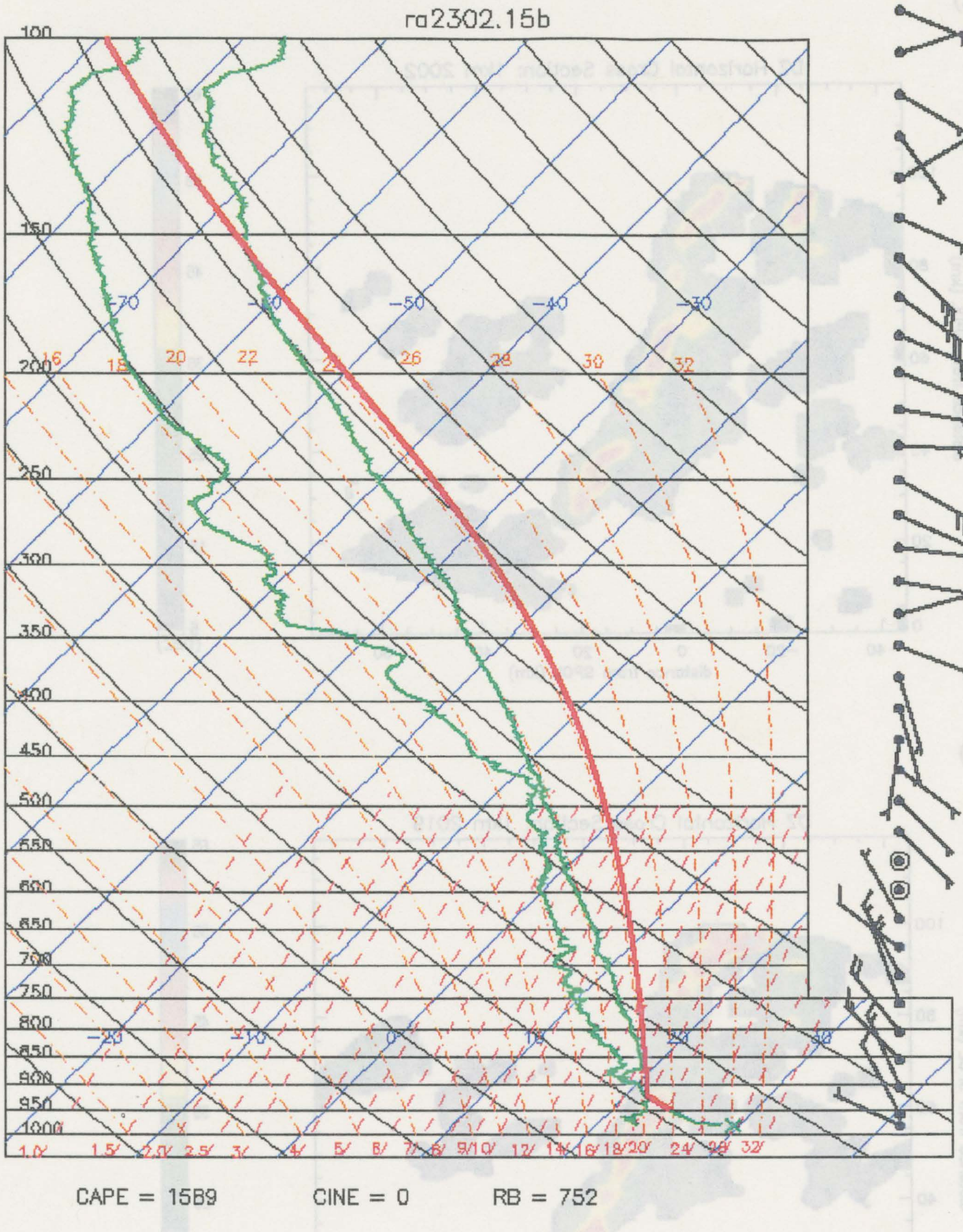

Figure 4.1: Skew-T/Log-P diagram of the troposphere at 15 UTC on 23 February 1999.

(a)

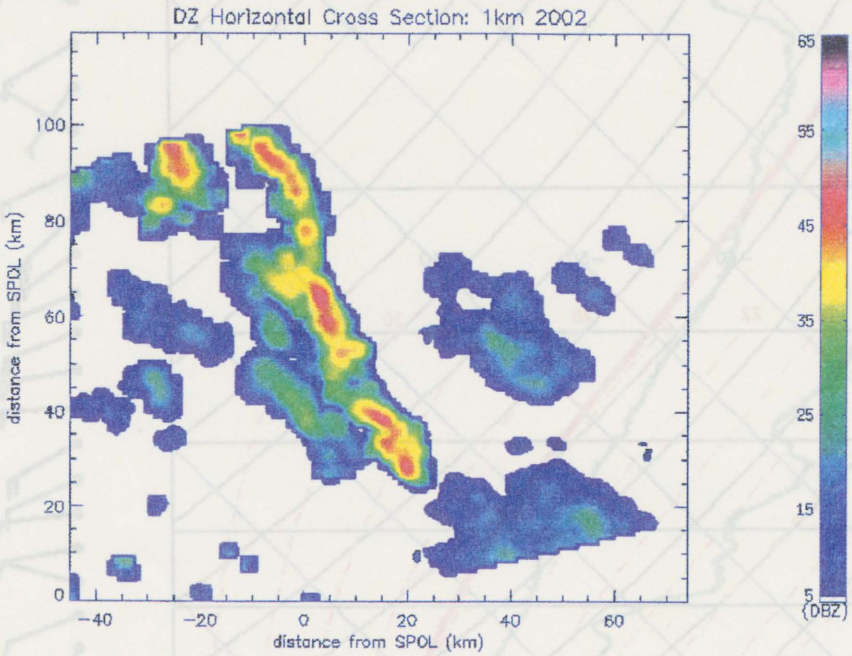

(b)

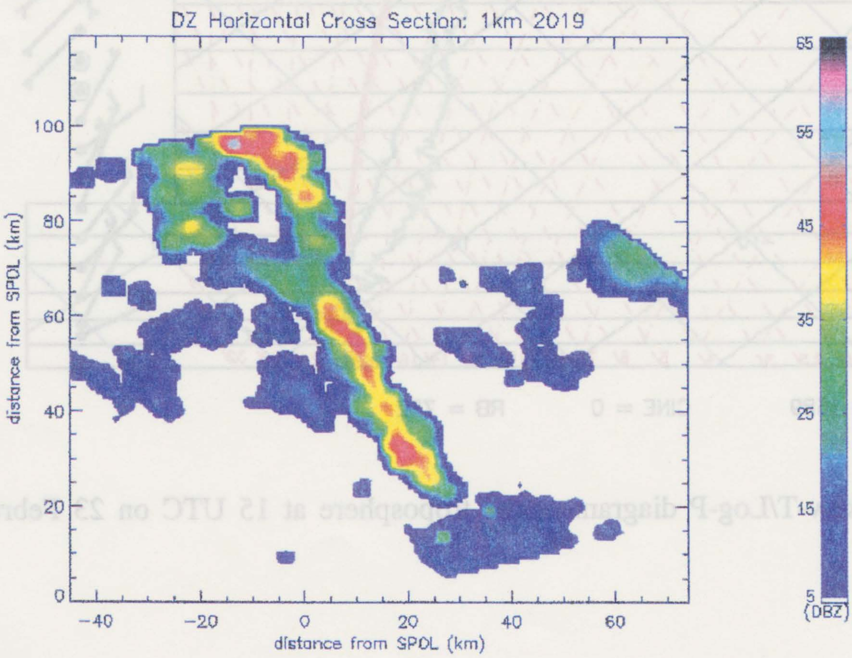

Figure 4.2: Horizontal cross-sections of reflectivity at 1km. (a) 2002 UTC (b) 2019 UTC.

(c)

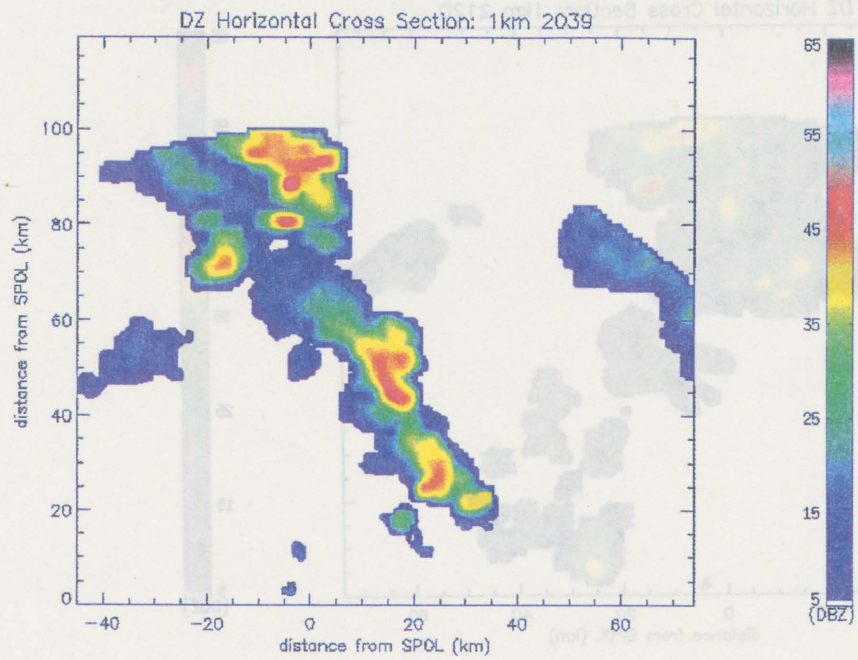

(d)

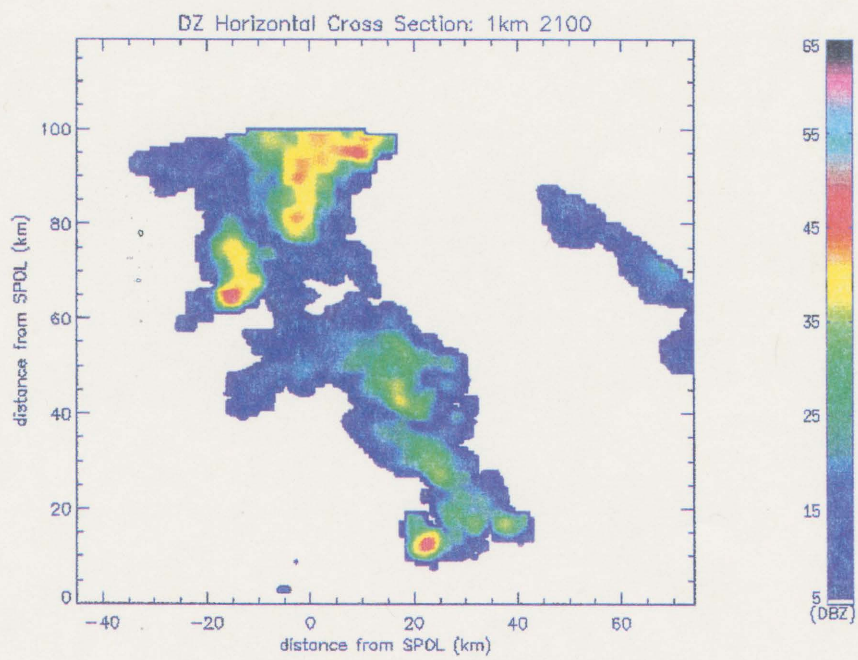

Figure 4.2: Results at (c) 2039 UTC (d) 2100 UTC.

(e)

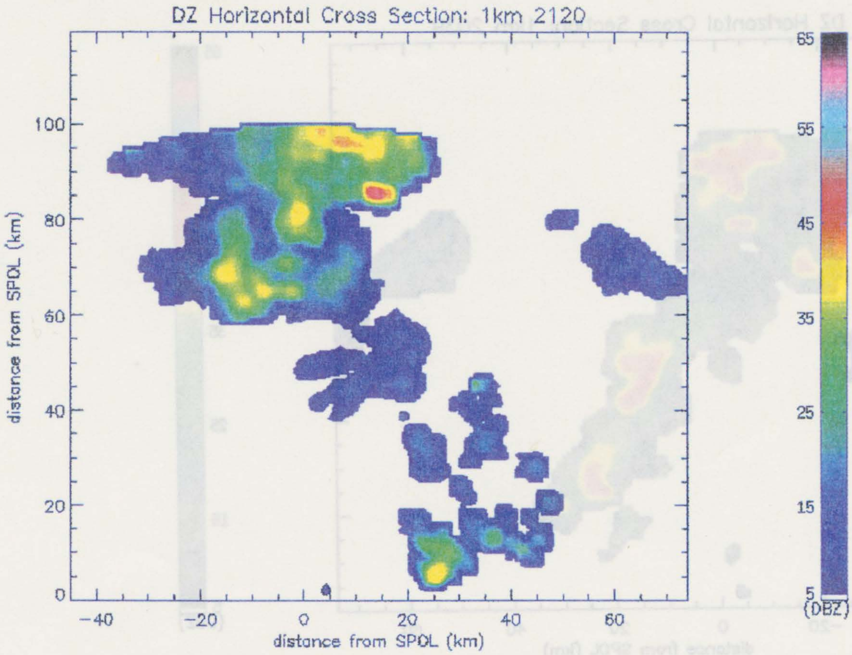

Figure 4.2: Results at (e) 2120 UTC.

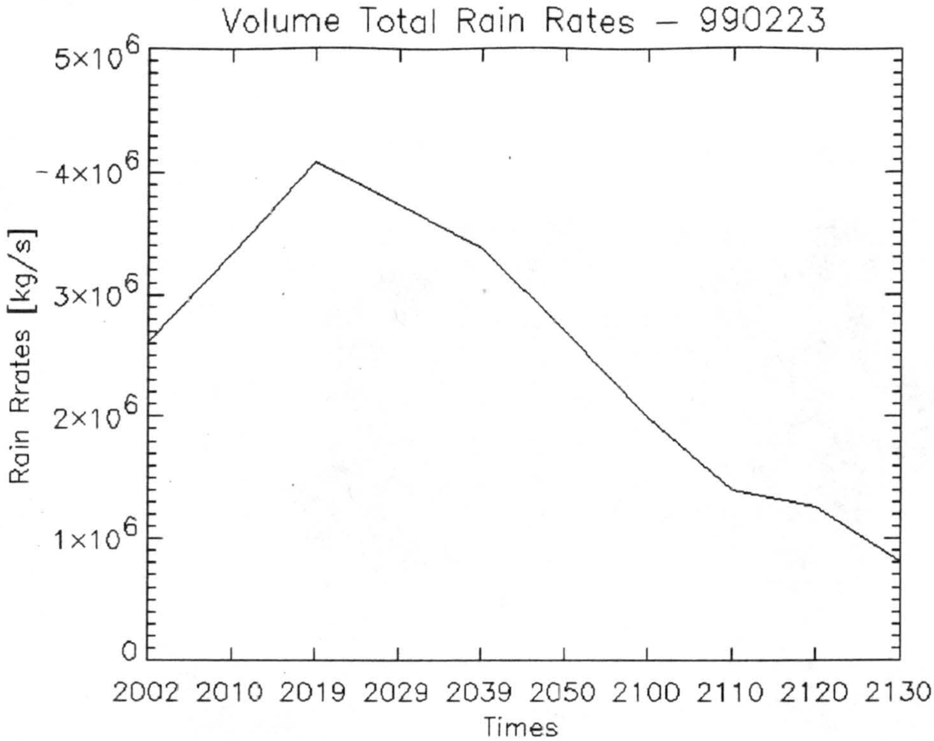

Figure 4.3: Rain rates in kg s^{-1} for each volume of 990223.

(a)

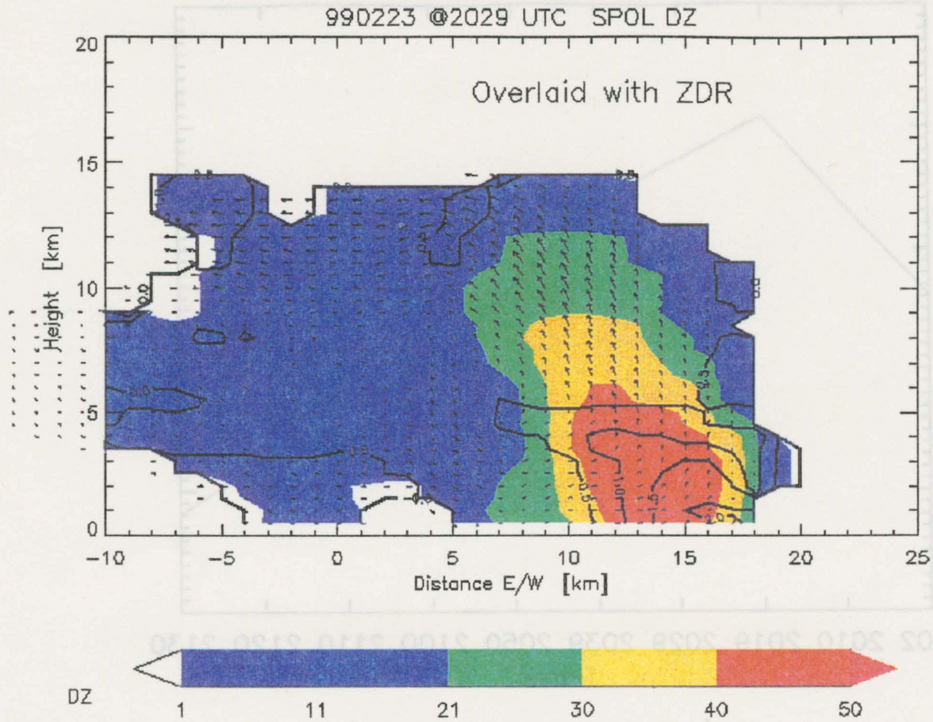

(b)

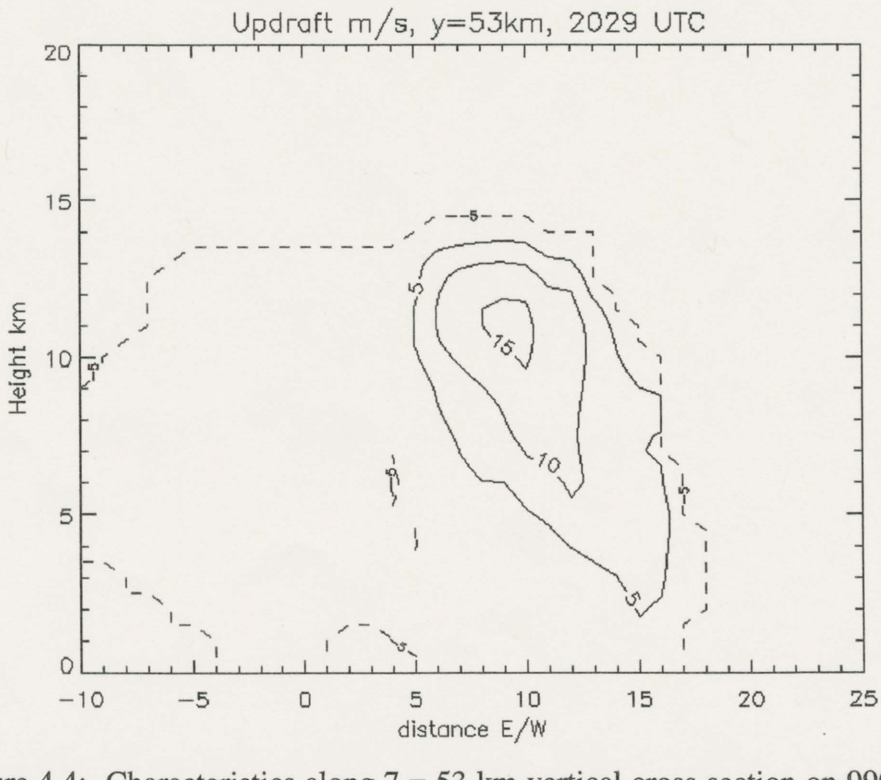

Figure 4.4: Characteristics along 7 = 53 km vertical cross section on 990223 at 2029 UTC. (a) Reflectivity in colored contours overlaid with Z_{dr} in 0.5 dB intervals. Arrows represent vertical velocities. (b) Vertical velocity in m s^{-1}.

(c)

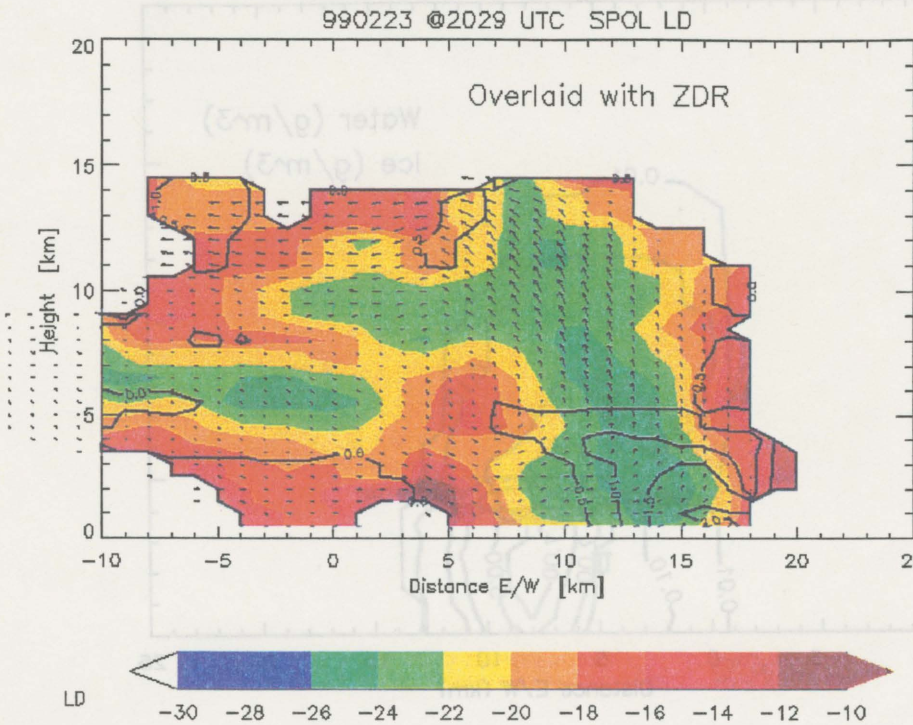

(d)

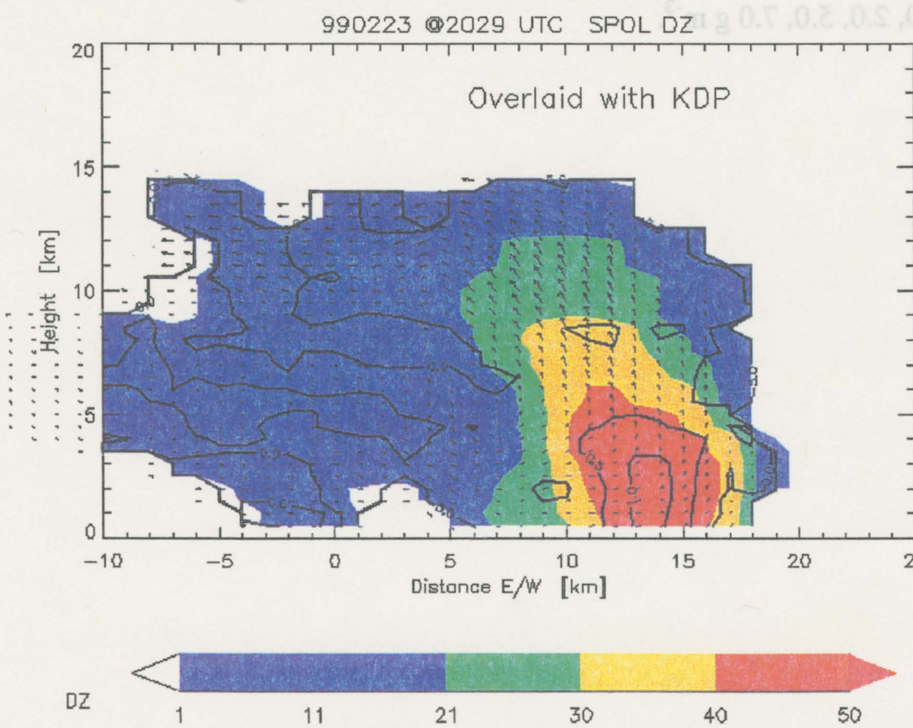

Figure 4.4: Results for (c) LDR in colored contours overlaid with Z_{dr} in 0.5 dB intervals. Arrows represent wind velocities. (d) Reflectivity in colored contours overlaid with K_{dp} in 0.5 deg km^{-1} intervals. Arrows represent wind velocities.

(e)

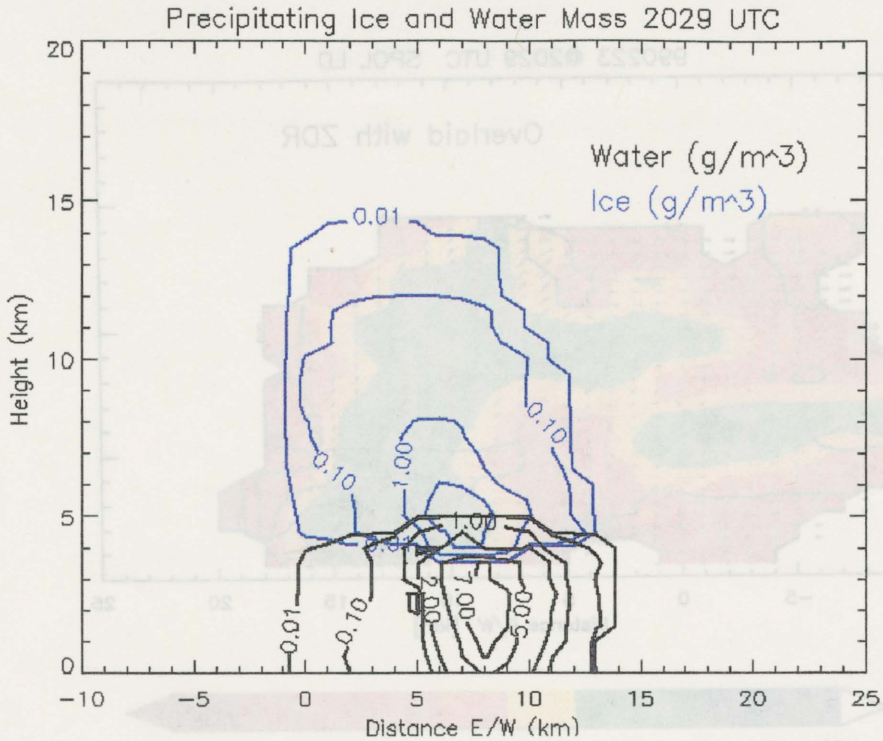

Figure 4.4: Results for (e) Precipitating ice and water masses in g m^{-3}. Contours at 0.01, 0.1, 1.0, 2.0, 5.0, 7.0 g m^{-3}.

(a)

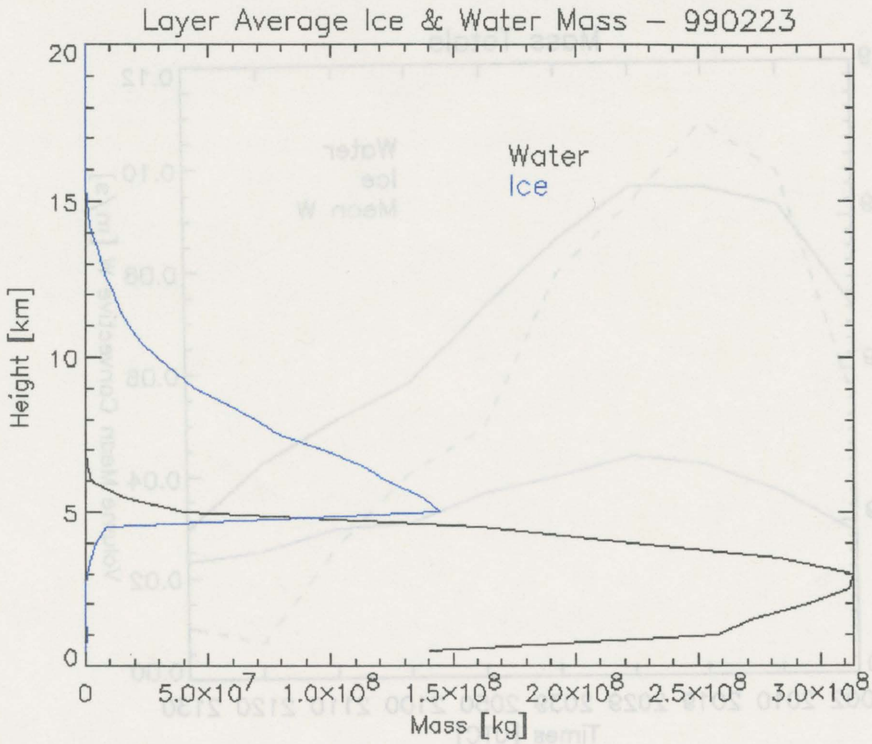

(b)

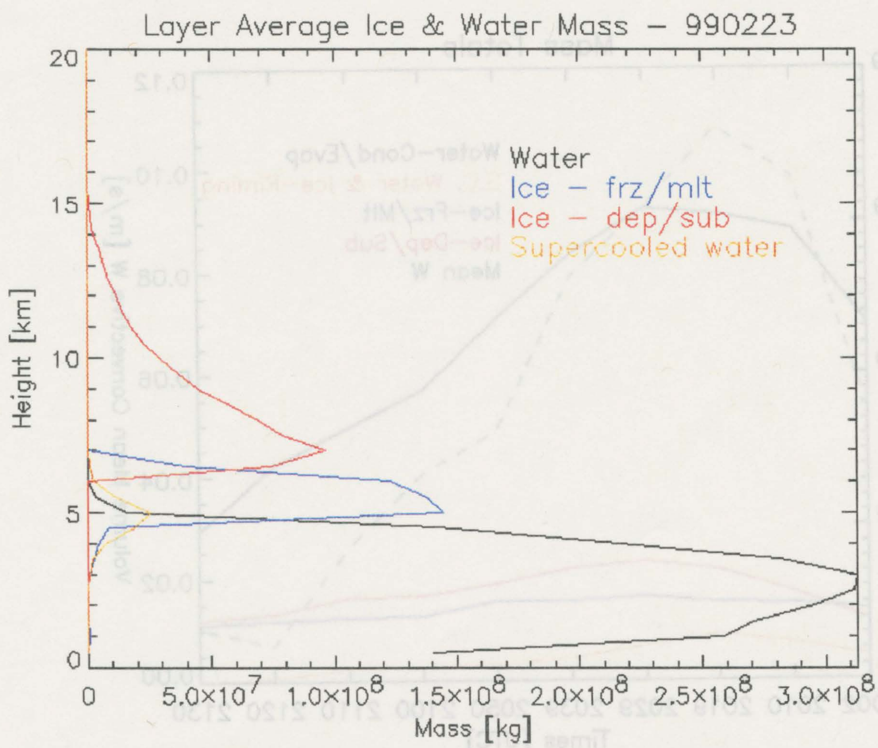

Figure 4.5: Layer average ice and water masses for all volumes of 990223. (a) Subdivided into only ice and water masses. (b) Masses associated with growth regimes previously defined.

(a)

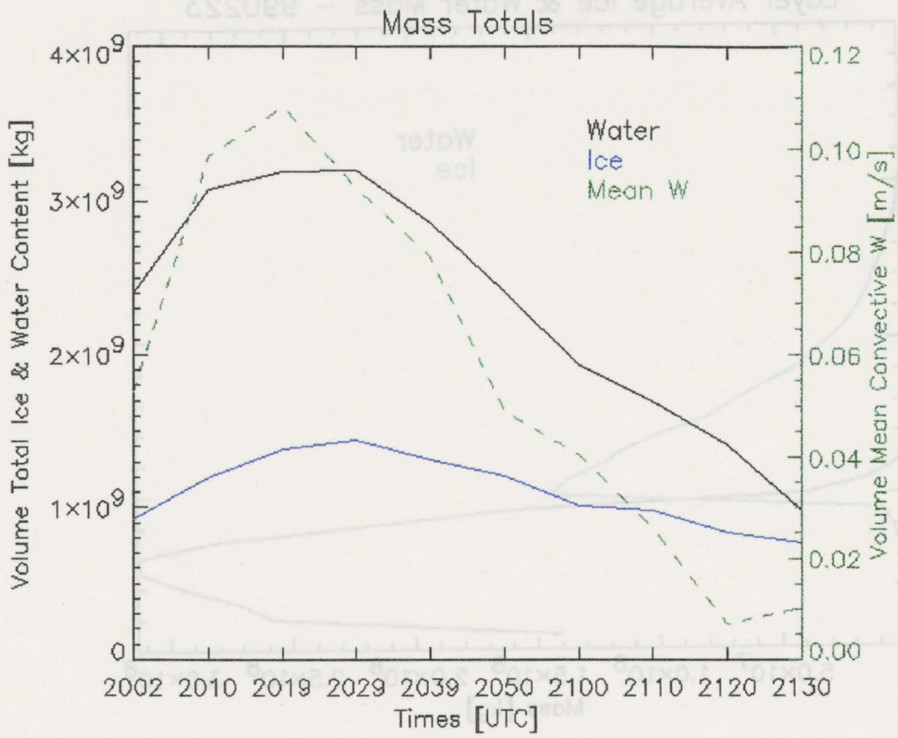

(b)

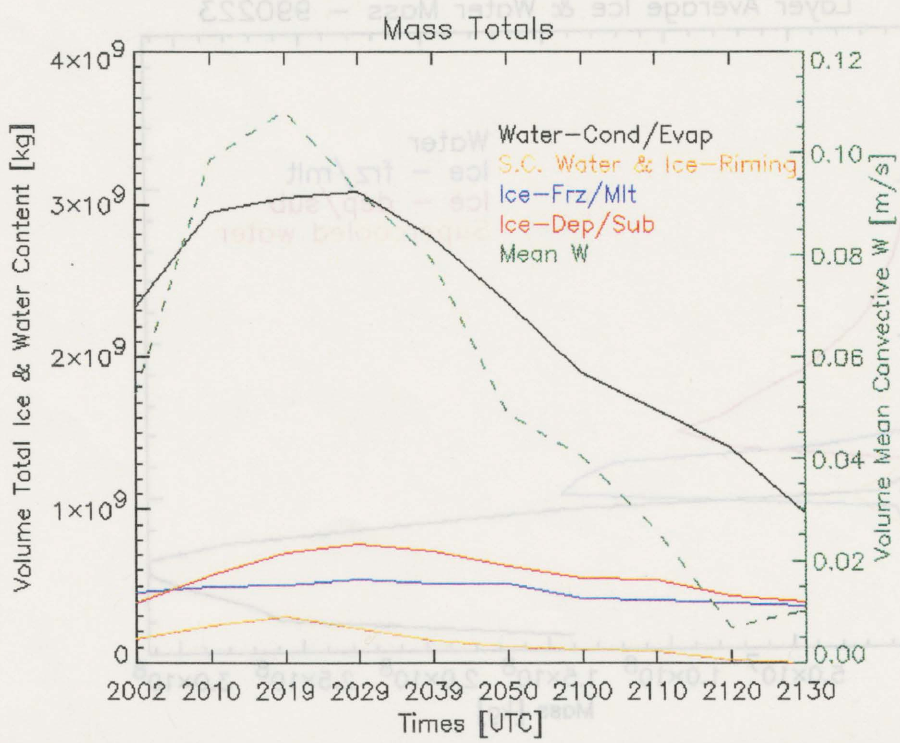

Figure 4.6: Mass totals as a function of time for 990223 overlaid with volume mean convective vertical velocity, w. (a) Subdivided into ice and water masses. (b) Masses associated with growth regimes as previously defined.

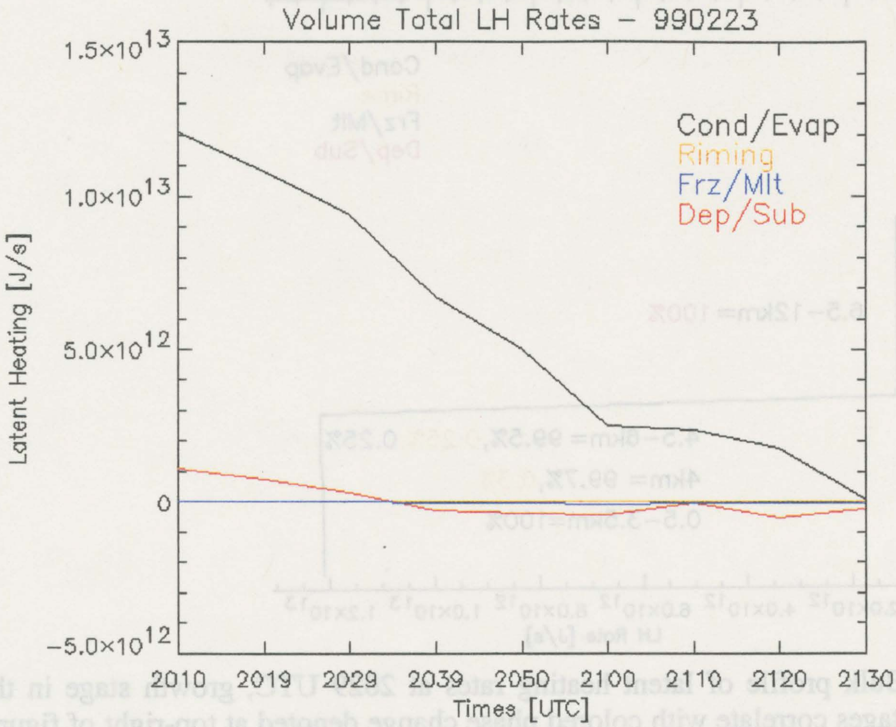

Figure 4.7: Latent heating rates estimated over time on 990223.

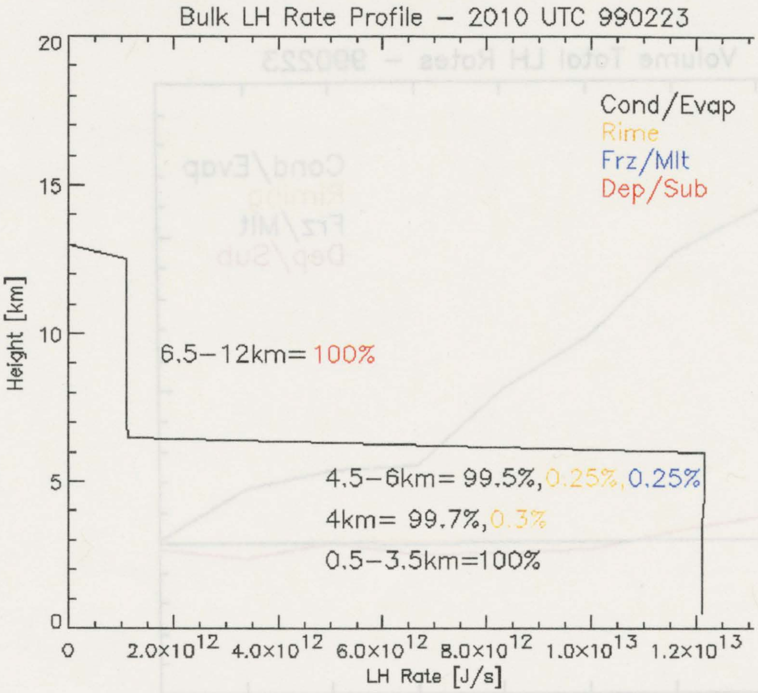

Figure 4.8: Bulk profile of latent heating rates at 2029 UTC, growth stage in the storm. Percentages correlate with colored phase change denoted at top-right of figure. Layers at 0.5 km resolution begin at level mentioned in figure.

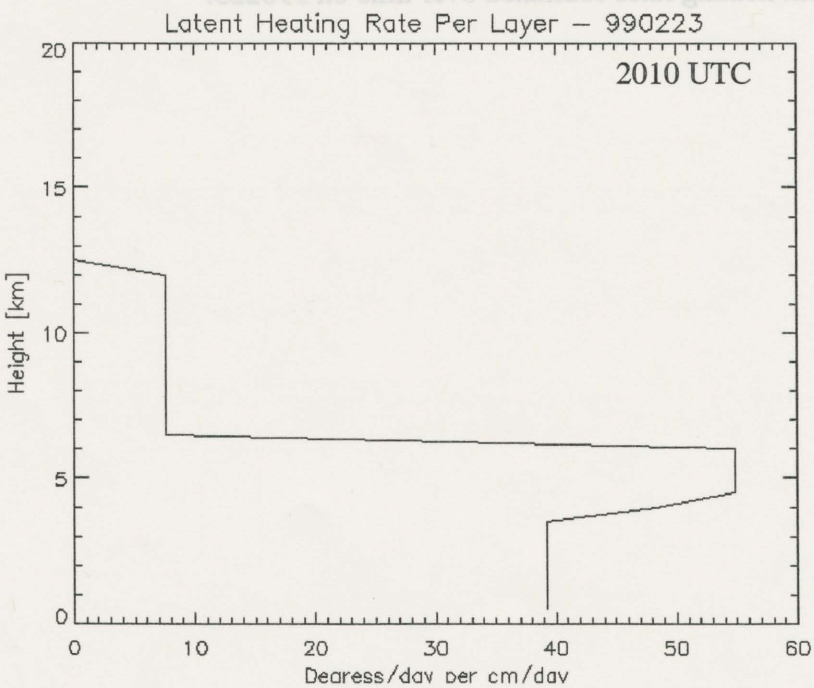

Figure 4.9: Bulk latent heating rate per layer at 2010 UTC normalized by an instantaneous rain rate of 8 cm day^{-1} and rain rate coverage area of 3607 km^2. Average densities were used for each bulk layer as denoted in Figure 4.8.

(a)

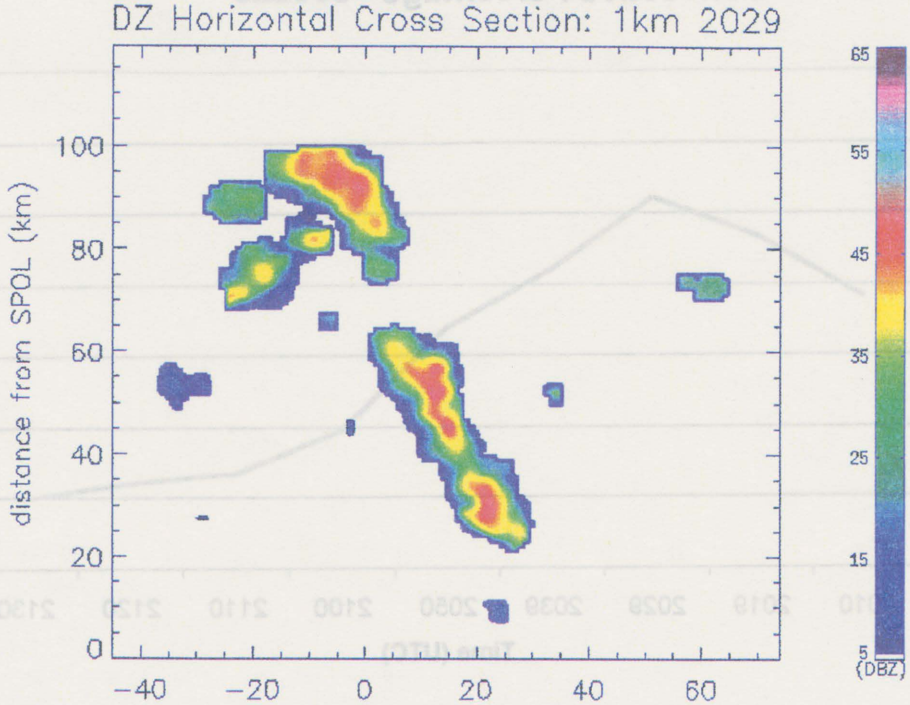

(b)

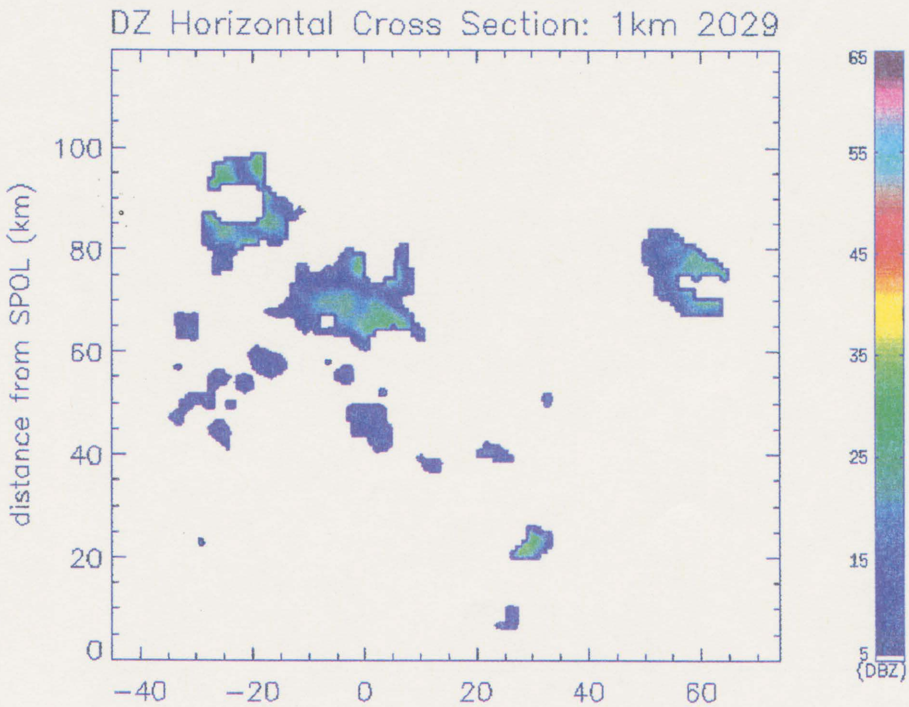

Figure 4.10: Example of convective/stratiform partitioning for reflectivity at 1km AGL and 2029 UTC for (a) convective and (b) stratiform reflectivities.

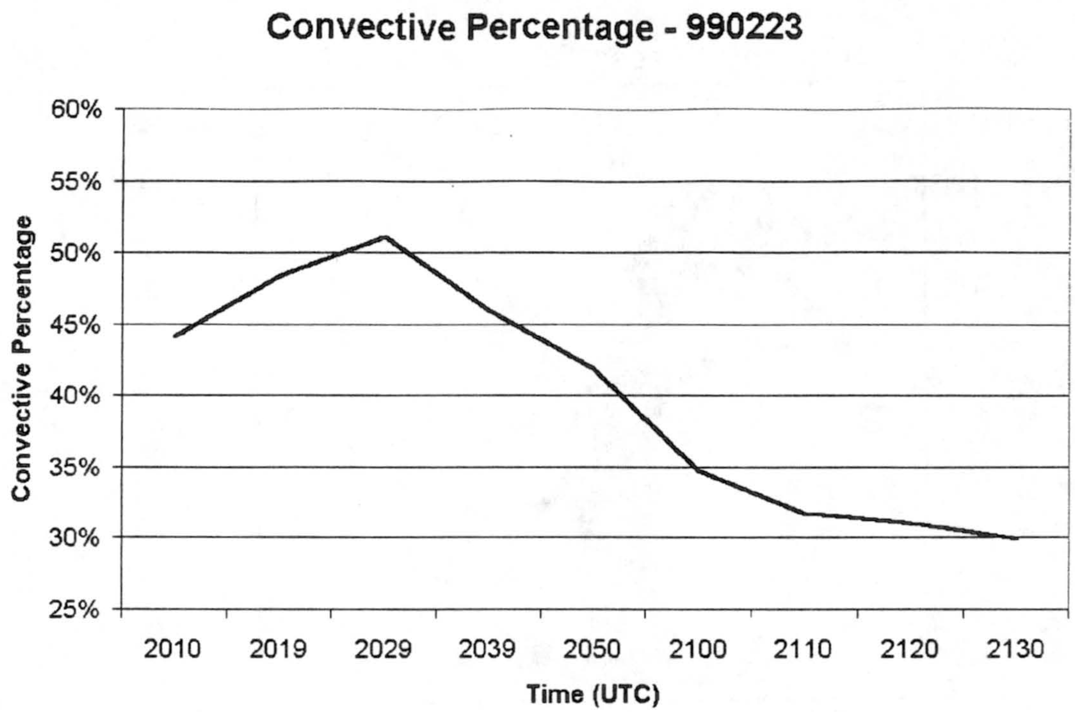

Figure 4.11: Convective percentage based on convective/stratiform partitioning for 990223.

(a)

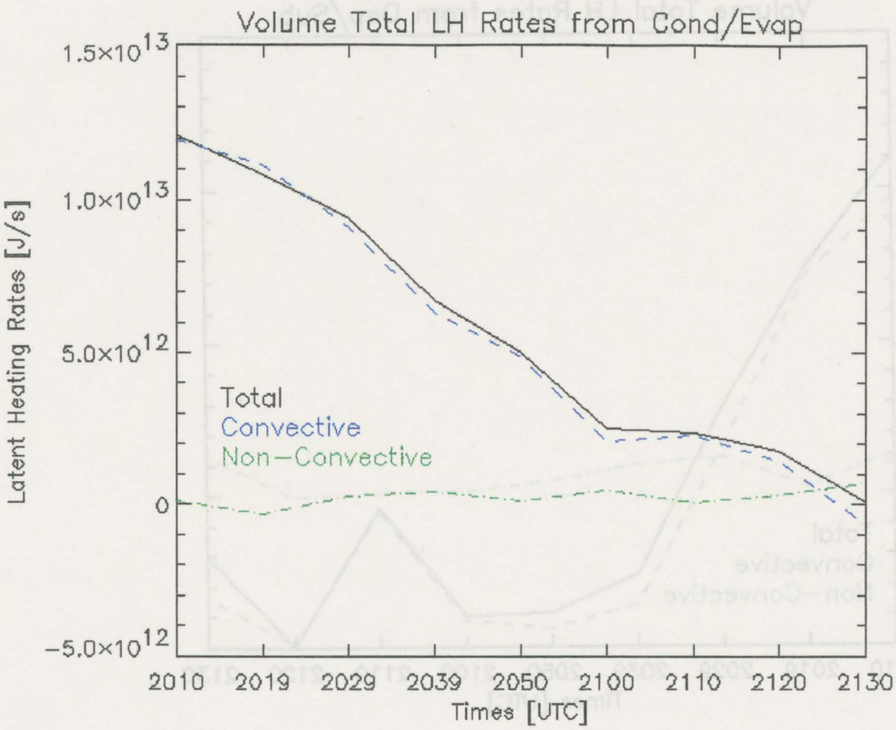

(b)

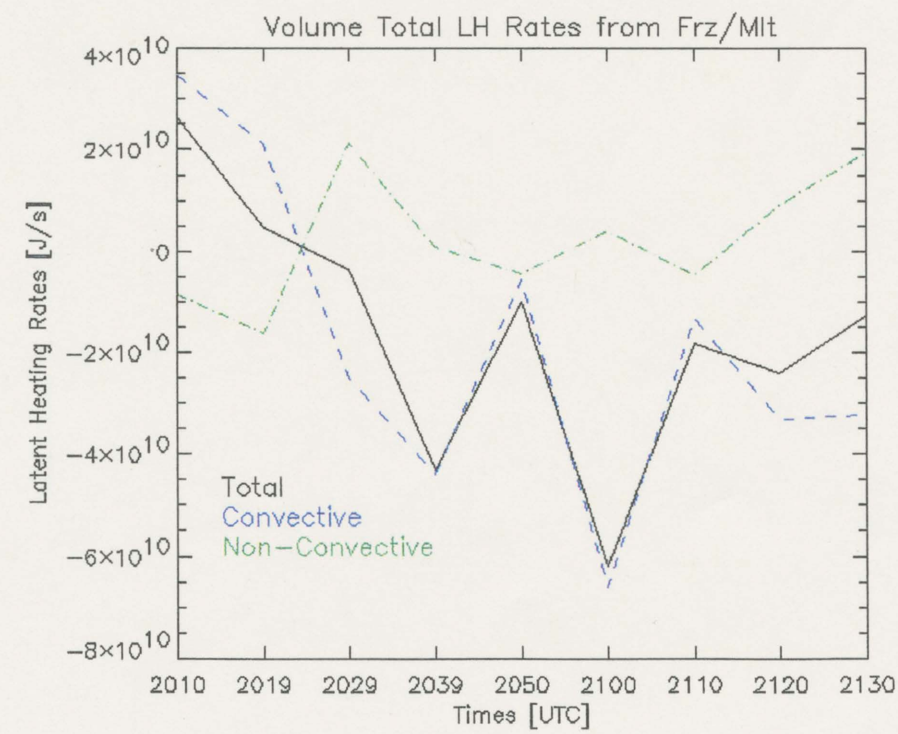

Figure 4.12: Latent heating rates vs. time, partitioned for convective and stratiform components due to (a) condensation and evaporation and (b) freezing and melting.

(c)

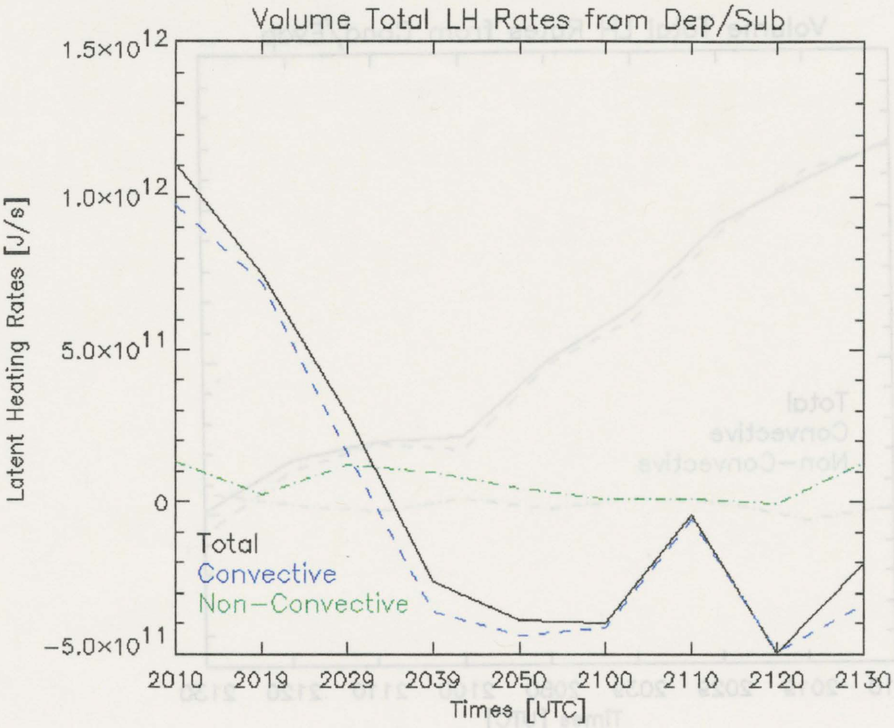

Figure 4.12: Results for (c) deposition and sublimation.

CHAPTER FIVE

Conclusions and Future Research

Dual-Doppler and multiparameter radar data were used to study the environmental atmospheric conditions, storm evolution, kinematics, microphysics and latent heating characteristics for two tropical mesoscale convective systems observed in the Amazon during the TRMM-LBA field campaign. Each MCS occurred in a different meteorological regime as classified by the low-level zonal wind direction (i.e. easterly and westerly). The data were objectively partitioned into convective and stratiform components and the water and ice masses were determined via the Z_{dp} method. Temporal changes in these quantities allowed for an observationally based estimation of each categories' latent heating rates.

The easterly MCS on 17 February 1999 lasted more than 2.5 hours and formed from the merger of several convective cells forced by diurnal heating. The troposphere had moderately high available potential energy (2327 J kg^{-1}) and moisture at the surface. Drier air aloft (relative to the westerly phase conditions) could have contributed to the small amount of stratiform precipitation coverage (Halverson et al., 1999). The westerly MCS on 23 February 1999 lasted approximately 2 hours and formed from the merger of several cold pools along a line of existing cumulus clouds. The troposphere on this day had less available potential energy (1589 J kg^{-1}) and was moister throughout than the easterly case. The greater

CAPE, drier air aloft and stronger shear likely contributed to the more intense and more organized system of 17 February 1999.

Kinematic and microphysical differences occurred between the two storms as well. The easterly case contained strong updrafts (maximums exceeding 20 m s^{-1}), differential reflectivity columns extending 1-2 km above the freezing level, and some linear depolarization ratio "caps" above those columns indicating active mixed phase regions. Similar observations have been found in other intense tropical (Carey and Rutledge, 2000; Ahijevych et al., 2000; Cifelli et al., 2001) and sub-tropical studies (Fulton and Heymsfield, 1991; Herzegh and Jameson, 1992; Bringi et al., 1997). Riming occurred in these mixed phase regions when trends in the mean convective vertical velocities approached local maximums. Approximately twice the amount of total water mass was found in the easterly case compared to the westerly case, in part because there was more convective echo found in this storm. The westerly case also contained intense convection, strong updrafts (maximums exceeding 15 m s^{-1}), differential reflectivity columns extending slightly above the freezing level, and some weak linear depolarization ratio "caps." The updrafts allowed some water to be lofted above the freezing level to participate in riming processes although the volume total masses involved in this westerly case were approximately 75% less than in the easterly case. The largest amount of riming was co-located with the maximum in mean convective vertical velocity. Microphysically, this westerly event was not as robust as the easterly. Previous studies have found the westerly events to be less intense and less microphysically active during TRMM-LBA (Rutledge et al., 2000; Carey et al., 2001; Cifelli et al., 2001; Petersen et al., 2001).

Substantially more liquid water mass compared to ice mass was found for most volumes in both meteorological regimes. This is in contrast to mid-latitude studies (Chandrasekar et al., 1991; Tong et al., 1998), but similar to tropical modeling studies. One example of such model output is Figure 5.1. It shows a mean precipitating ice and water content profile for areas with convective rain within 10% of 20 mm hr^{-1}. The data used in this figure were derived from two tropical cloud resolving model simulations, obtained from the Goddard Cumulus Ensemble (GCE) model, and one month's oceanic data from TRMM's PR (Precipitation Radar; Tao and Simpson, 1993). Each PR pixel's observed reflectivity was compared with the model simulations' reflectivity and the profile with the smallest RMS difference was selected for that pixel. Finally, information about the precipitating ice and water profiles can be obtained from the chosen model simulations. Interestingly, the GCE model oceanic profile looks very similar to both LBA case studies in this thesis. The actual values, once converted to identical units, are of the same order of magnitude. For a single volume with an average rain rate of 22 mm hr^{-1} (1832 UTC on 990217), the values are within a factor of three. This is not validation for work in this thesis, but the results do show consistency between model-diagnosed and radar-diagnosed (this study) contents over the Amazon basin and other oceanic environments in the tropics.

Rain rates were on the order of 10^6 kg s^{-1} and the westerly values ranged from 20-40% less than the easterly ones during the strong stages of the storms. Rickenbach et al. (2001) found that TRMM-LBA's westerly cases had approximately 27% less rainfall than easterly storms because of the weaker convection and lower mean rainfall intensities in the westerly cases. When the rain rates for the storms studied in this thesis are plotted together, it is obvious the easterly rate has a steeper slope in both the growth and decline stages (Figure 5.2). Note that the rain rates are aligned to match volumes of similar life cycle stages in this figure. Actual values for the westerly case begin at volume number 7 on the plot. This more gradual rain rate decline was also observed in Cifelli et al. (2001; Figure 5.3). This likely occurs because the westerly regime MCSs have larger stratiform precipitation areas associated with them (Cifelli et al., 2001; Halverson et al., 2001; Rickenbach et al., 2001).

The latent heating rates for both case studies were dominated by the condensation term throughout most of their life cycles. This agrees with both Chandrasekar et al. (1991) and Tong et al. (1998), although the actual magnitudes of the heating were an order of magnitude larger in this study. These larger heating rates were consistent with the larger water masses diagnosed for these cases. Latent heating rates due to deposition for both cases were of similar magnitude during their growth stages. Latent heating rates due to sublimation were significant during the dissipation stages. Other observationally based studies have not included separate effects due to deposition and sublimation. The heating rates due to freezing, melting and riming were inconsequential as their values were 2-3 orders of magnitude smaller. Chandrasekar et al. (1991) and Tong et al. (1998) did find freezing and melting contributing slightly to the total latent heating rates. However, their studies actually contained more ice mass than water mass; therefore, ice processes should have played a larger role. The convective latent heating rates were positive throughout the troposphere while the systems were robust, agreeing with the findings of Houze (1997). The stratiform components had much smaller values and less interpretable signals. However, the deposition sub-component for the westerly case remained positive showing that stratiform processes did heat the troposphere above 6.5 km AGL throughout the event.

Several modeling and budget studies have examined the apparent heating of tropical large-scale motion systems due to radiation, net condensation and the vertical convergence of eddy transport of sensible heat, or Q_1 (Johnson, 1984; Tao et al., 1993a; Tao et al., 1993b and others). Q_1 is dominated by the latent heating term. Figure 5.4 shows four other studies' normalized apparent heat source profiles. Notice the peak for all studies is between 4 and 7 km AGL. Similar profiles were also found by Tao et al. (1993b) for an EMEX tropical squall line and Tao et al. (1993a) in GATE with total heating maximums near 5 km. The shapes of these profiles are very similar to Figures 3.10 and 4.9 in this study. The values in this study are much smaller than in Fig. 5.4, however. This is primarily due to three reasons. First, the values from Fig. 5.4 are derived from sounding data that cannot resolve the mesoscale updrafts this study observed. Second, the values from Fig. 5.4 are derived from composite soundings averaged over rather large time periods. This study looked at a "snapshot" of one growth stage for each storm. Third, this study focused on bulk layers of heating in the profile as determined by the thermodynamic processes involved. The other studies gave values for each kilometer of the troposphere.

Other studies have compared the easterly (westerly) regime to the "break" ("monsoon") regime in Darwin, Austrailia (Cifelli et al., 2001; Halverson et al., 2001). During the "break" period in Darwin, Cifelli and Rutledge (1994) found echo tops up to 18 km with relatively dry soundings. Convective cells usually merged to a convective complex with an associated trailing stratiform region. They also found mature updrafts with graupel and supercooled water above the 0° C level. The average CAPE for the break cases in Darwin was 951 J kg^{-1} based on 78 cases (Keenan and Carbone, 1992). The 17 February 99 easterly case does fit these descriptions except its CAPE was significantly higher (2327 J kg^{-1}) and it did not have a trailing stratiform component. The monsoon cases in Darwin are described to be moist at all levels in the troposphere. The CAPE was quite variable, but the strongest values were found during this regime. The average was 1192 J kg^{-1} using only 19 cases (Keenan and Carbone, 1992). Echo tops averaged 12 km, reflectivities > 30 dBZ remained below 6 km, and weaker vertical velocities were observed. Large areas of stratiform echo were also seen (Cifelli and Rutledge, 1994). The 23 February 1999 case fits some of these characteristics, but it did exhibit strong convection above the freezing level leading to mixed phase regions in contrast to the Darwin "monsoon" studies.

These results have important implications for TRMM. Key goals of TRMM include characterizing the kinematic, microphysical, and heating profiles of tropical convection. Additionally, ground-based observational validation for space borne retrievals and numerical model simulations is needed. Further work on these specific case studies would include comparing the microphysical subdivisions and latent heating estimates with model output and correlating the masses associated with riming and lightning flash rates. Other case studies are also available for research in TRMM-LBA.

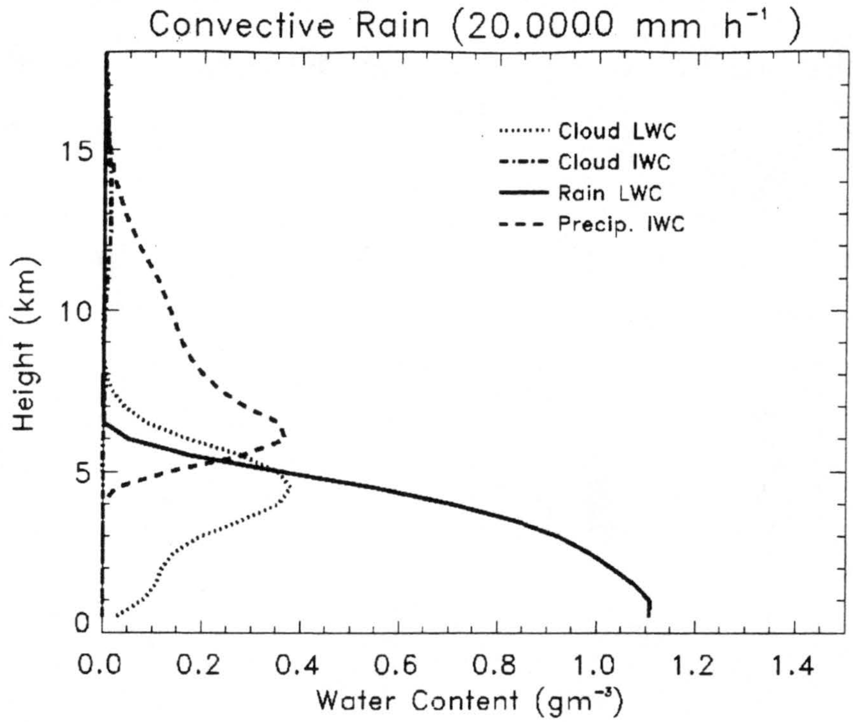

Figure 5.1: The precipitating ice and water content profile found via the GCE model for areas with convective rain within 10% of 20 mm hr^{-1}. The solid line is the precipitating water (rain) mixing ratio in g m^{-3}. The single dashed line is the precipitating ice mixing ratio in g m^{-3}. The cloud mixing ratios are not examined in this study. Figure courtesy of Dr. Tristan S. L'Ecuyer, Colorado State University.

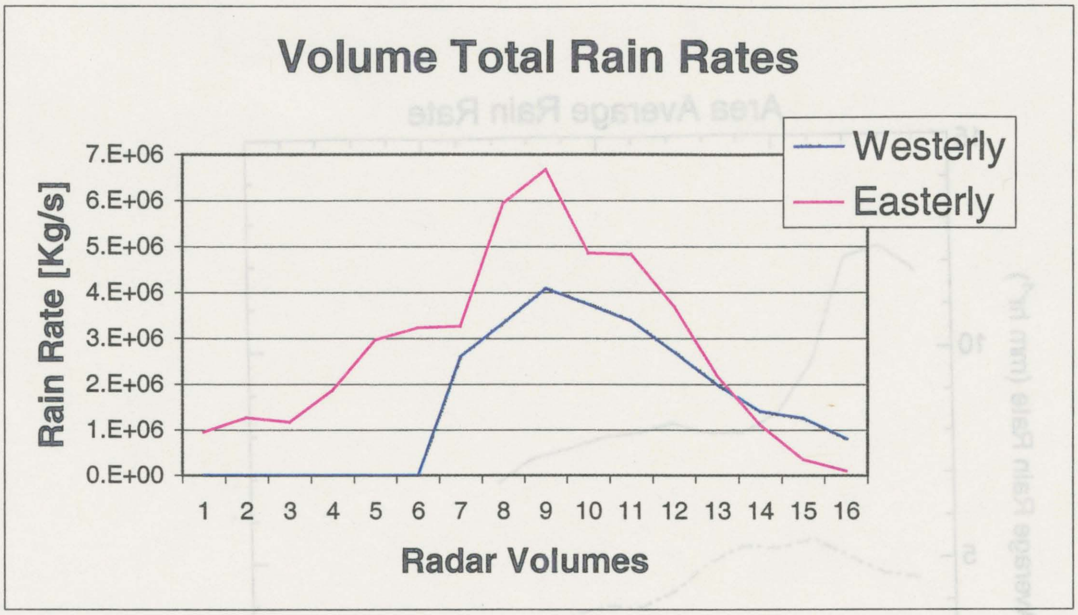

Figure 5.2: Total rain rates in kg s^{-1} for case studies, 990217 (easterly) and 990223 (westerly). Volumes were aligned to match similar stages in lifecycle. Data recovered for 990223 actually begins for volume number 7.

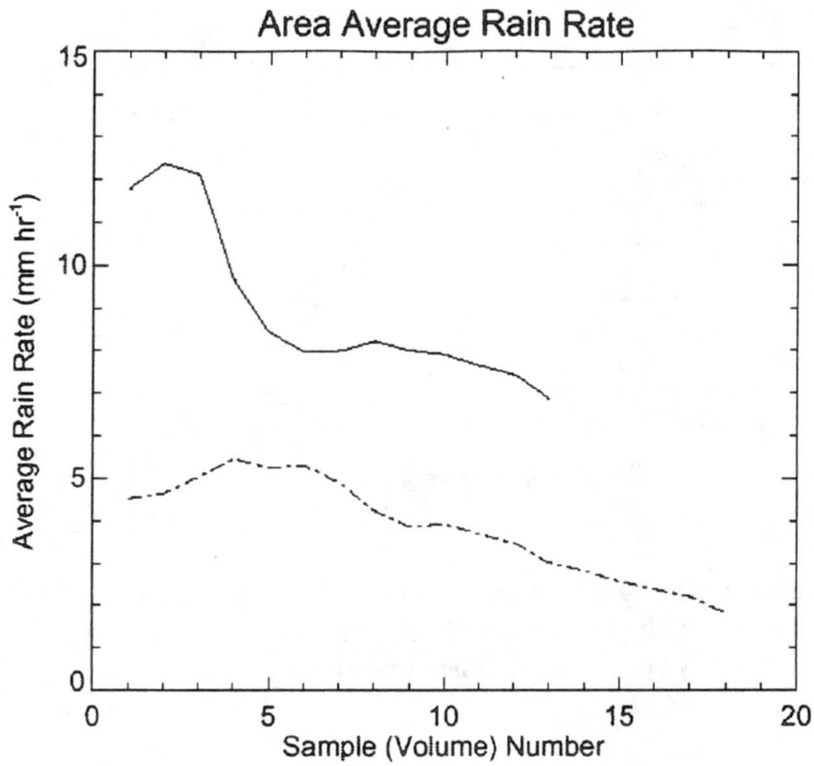

Figure 5.3: Time series of average rain rate for 26 January 1999 (easterly) and 25 February 1999 (westerly). The easterly values form a solid line and the westerly form a dashed line. The abscissa represents the radar volume number instead of time so the two cases can be overlaid (from Cifelli et al., 2001).

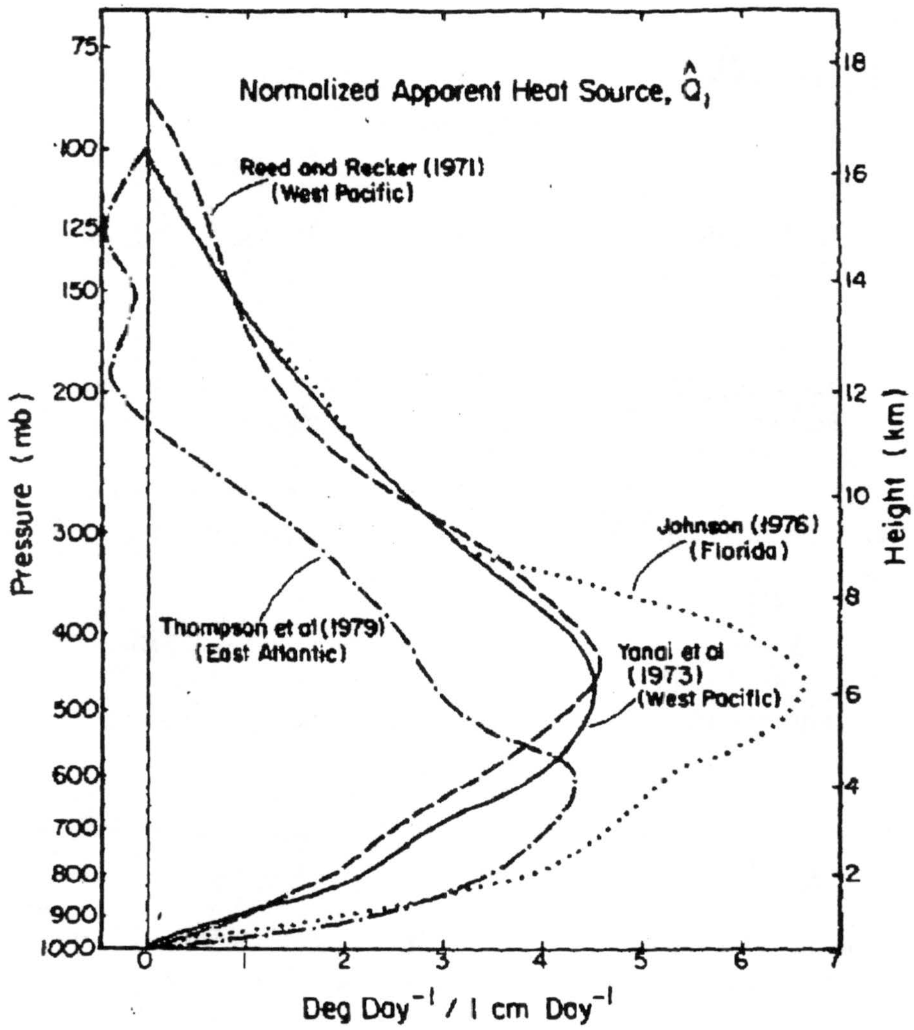

Figure 5.4: Normalized apparent heat source Q_1 for West Pacific, East Atlantic and Florida regions (From Johnson, 1984).

REFERENCES

Ahijevych, D. A., Rutledge, S. A. and L. D. Carey, 2000: Radar and electrical characteristics of convection observed during MCTEX. *Aust. Met. Mag.*, **49**, 165-180.

Aydin, K., Seliga, T. A. and V. N. Bringi, 1984: Differential radar scattering properties of model hail and mixed phase hydrometeors. *Radio Sci.*, **19**, 58-66.

Aydin, K., and Y. Zhao, 1990: A computational study of polarimetric radar observables in hail. *IEEE Trans. On Geo Sci. and Remote Sensing*, **28**, 412-422.

Bringi, V. N., K. Knupp, A. Detwiler, L. Liu, I. J. Caylor and R. A. Black, 1997: Evolution of a Florida thunderstorm during the Convection and Precipitation/Electrification Experiment: The case of 9 August 1991. *Mon. Wea. Rev.*, **125**, 2131–2160.

Bringi, V. N. and V. Chandrasekar, 2000: Polarimetric Doppler Weather Radar-Principles and Applications, Cambridge University Press, 656 pp.

Carey, L. D., and S. A. Rutledge, 1996: A multiparameter radar case study of the microphysical and kinematic evolution of a lightning producing storm. *Meteorol. Atmos. Phys.*, **59**, 33-64.

Carey, L. D. and S. A. Rutledge, 1998: Electrical and multiparameter radar observations of a severe hailstorm. *J. Geophys. Res.*, **103**, 13979-14000.

Carey, L. D. and S. A. Rutledge, 2000: The relationship between precipitation and lightning in tropical island convection: A C-band polarimetric radar study, *Mon. Wea. Rev.*, **128**, 2687-2710.

Carey, L. D., R. Cifelli, W. A. Petersen and S. A. Rutledge, 2001: Characteristics of Amazonian rain measured during TRMM-LBA, Preprints, *30th Conference on Radar Meteorology*, Munich, Germany, 3 pp.

Chandrasekar, V., V. N. Bringi, N. Balakrishnan and D. S. Zrnić, 1990: Error structure of multiparameter radar and surface measurements of rainfall. Part III: Specific differential phase. *J. Atmos. Oceanic Tech.*, **7**, 621-629.

Chandrasekar, V., C. A. Atwater and T. H. Vonder Haar, 1991: Convective latent heating estimates from radar data, Preprints, *25th Conference on Radar Meteorology*, Paris, France, 155-158.

Churchill, D. D., R. A. Houze, Jr., 1984: Development and structure of winter monsoon cloud clusters on 10 December 1978. *J. Atmos. Sci.*, **41**, 933–960.

Cifelli, R. and S. A. Rutledge, 1994: Vertical motion structure in Maritime Continent Mesoscale Convective Systems: Results from a 50-MHz profiler. *J. Atmos. Sci.*, **51**, 2631-2652.

Cifelli, R., W. A. Petersen, L. D. Carey and S. A. Rutledge, 2001: Radar observations of the kinematic, microphysical and precipitation characteristics of two MCSs in TRMM-LBA. *J. Geophys. Res.*, In press.

Conway, J. W. and D. S. Zrnić, 1993: A study of embryo production and hail growth using dual-Doppler and multiparameter radars. *Mon. Wea. Rev.*, **121**, 2511–2528.

Cressman, G. P., 1959: An operational objective analysis system. *Mon. Wea. Rev.*, **87**, 367-374.

DeMaria, M., 1985: Linear response of a stratified tropical atmosphere to convective forcing. *J. Atmos. Sci.*, **42**, 1944–1959.

Doviak, R. J. and D. S. Zrnić, 1993: *Doppler Radar and Weather Observations*, 2nd ed., Academic Press, 562 pp.

Fulton, R. and G. M. Heymsfield, 1991: Microphysical and radiative characteristics of convective clouds during COHMEX. *J. Appl. Meteor.*, **30**, 98-116.

Gandú, A. W. and P. L. Silva Dias, 1998: Impact of tropical heat sources on the South American tropospheric upper circulation and subsidence. *J. Geophys. Res.*, **103** , 6001-6015.

Golestani, Y., V. Chandrasekar and V. N. Bringi, 1989: Intercomparison of multiparameter radar measurements. *Proc. 24th Conf. Radar Meteorology.*, Tallahassee, FL, Amer. Meteor. Soc., 309-314.

Hartmann, D. L., Hendon, H. H. and Houze, R. A., Jr., 1984: Some implications of the mesoscale circulations in tropical cloud clusters for large-scale dynamics and climate. *J. Atmos. Sci.*, **41**, 113-121.

Houze, R. A. Jr., 1982: Cloud clusters and large-scale vertical motions in the tropics. *J. Meteorol. Soc. Jap.*, **60**, 396-410.

Houze, R.A. Jr., 1989: Observed structure of mesoscale convective systems and implications for large-scale heating. *Quart. J. Roy. Meteor. Soc.*, **115**, 425-461.

Houze, R. A., Jr., 1997: Stratiform precipitation in regions of convection: A meteorological paradox? *Bull. Amer. Meteor. Soc.*, **78**, 2179-2196.

Hubbert, J. H., Bringi, V. N., Carey, L. D. and S. Bolen, 1998: CSU-CHILL polarimetric radar measurements from a severe hailstorm in eastern Colorado. *J. Appl. Meteor.*, **37**, 749-775.

Hudlow, M. D., 1979: Mean rainfall patterns for the three phases of GATE. *J. Appl. Meteor.*, **18**, 1656–1669.

Jameson, A. R., 1985: Microphysical interpretation of multiparameter radar measurements in rain. Part III: interpretation and measurement of propagation differential phase shift between orthogonal linear polarizations. *J. Atmos. Sci.*, **42**, 607- 614.

Johnson, R. H., 1984: Partitioning tropical heat and moisture budgets into cumulus and mesoscale components: Implications for cumulus parameterization. *Mon. Wea. Rev.*, **112**, 1590-1601.

Jorgensen, J. and M. LeMone, 1989: Vertical velocity characteristics of oceanic convection. *J. Atmos. Sci.*, **46**, 621-640.

Keenan, T. D. and R. E. Carbone, 1992: A preliminary morphology of precipitation systems in tropical northern Australia. *Quart. J. Roy. Meteor. Soc.*, **118**, 283-326.

Keenan, T. D. and Coauthors, 1994: Science Plan-Maritime Continent Thunderstorm Experiment. BMRC, Research Report 44, 61 pp. [Available from BMRC, P.O. Box 1289K, Melbourne, Victoria 3001, Australia.]

Knight, C. A. and N. C. Knight, 1970: The falling behavior of hailstones. *J. Atmos. Sci.*, **27**, 672-681.

Lau, K. M., Y. Ding, J. Wang, R. Johnson, T. Keenan, R. Cifelli, J. Gerlach, O. Thiele, T. Rickenbach, S. Tsay and P. Lin, 2000: A report of the field operations and early results of the South China Sea Monoon Experiment (SCSMEX). *Bull. Amer. Met. Soc.*, **81**, 1261-1270.

LeMone, M. and E. Zipser, 1980: Cumulonimbus vertical velocity events in GATE. Part I: Diameter, intensity and mass flux. *J. Atmos. Sci.*, **37**, 2444-2457.

LeMone, M., 1983: Momentum transport by a line of cumulonimbus. *J. Atmos. Sci.*, **40**, 1815-1834.

Lucas, C., E. Zipser and M. LeMone, 1994: Vertical velocities in oceanic convection off tropical Australia. *J. Atmos. Sci.*, **51**, 3183-3193.

Petersen, W. A., 1997: Multi-scale process studies in the tropics: Results from lightning observations. Ph.D. dissertation, Colorado State University, 354 pp.

Petersen, W. A., S. A. Rutledge, R. Cifelli, B. S. Ferrier and B. F. Smull, 1999: Shipborne dual-Doppler operations during TOGA COARE: Integrated observations of storm kinematics and electrification. *Bull. Amer. Met. Soc.*, **80**, 81–96.

Petersen, W. A., S. W. Nesbitt, R. J. Blakeslee, R. Cifelli, P. Hein and S. A. Rutledge, 2001: TRMM observations of intraseasonal variability in convective regimes over the Amazon. *J. Climate*, In press.

Pruppacher, H. R. and K. V. Beard, 1970: A wind tunnel investigation of the internal circulation and shape of water drops falling at terminal velocity in air. *Quart. J. Roy. Meteor. Soc.*, **96**, 247-256.

Pruppacher, H. R. and J. D. Klett, 1997: Microphysics of Clouds and Precipitation. 2nd Ed. Kluwer Academic, 954 pp.

Rickenbach, T. M., R. N. Ferriera, J. Halverson, D. L. Herdies and M. A. F. Silva Dias, 2001: Modulation of convection in the southwestern Amazon basin by extratropical stationary fronts. *J. Geophys. Res., Special Issue on TRMM-LBA*, In press.

Riehl, H. and J. S. Malkus, 1958: On the heat balance in the equatorial trough zone. *Geophysics*, **6**, 503-538.

Rogers, R. R. and M. K. Yau, 1989: A Short Course in Cloud Physics. Butterworth Heinemann Press, 3rd ed., 290 pp.

Roux, F., J. Testud, M. Payen and B. Pinty, 1984: West African squall-line thermodynamic structure retrieved from dual-Doppler observations. *J. Atmos. Sci.*, **41**, 3104-3121.

Rutledge, S. A. and R. A. Houze, Jr., 1987: A diagnostic modeling study of the trailing stratiform region of a midlatitude squall line. *J. Atmos. Sci.*, **44**, 2640-2658.

Rutledge, S. A., E. R. Williams and T. D. Keenan, 1992: The Down Under Doppler and Electricity Experiment (DUNDEE): Overview and preliminary results. *Bull. Amer. Met. Soc.*, **73**, 3-16.

Rutledge, S. A., R. Avissar, V. Bringi, L. Carey, W. Petersen, E. Williams, J. Wilson and E. Zipser, 1998: TRMM-LBA Brazil implementation plan, A science overveiw for the NSF component of TRMM-LBA/Brazil. http://radarmet.atmos.colostate.edu/lba_trmm/overview.html

Rutledge, S. A., W. A. Petersen, R. Cifelli and L. D. Carey, 2000: Early results from TRMM-LBA: Kinematic and microphysical characteristics of convection in distinct meteorological regimes. *Proc., 24th Conf. on Hurricanes and Tropical Meteorology*, 29 May – 2 June, Fort Lauderdale, FL, Amer. Meteor. Soc., 137-138.

Simpson, J., R. F. Adler and G. R. North, 1988: A proposed Tropical Rainfall Measuring Mission (TRMM) satellite. *Bull. Amer. Meteor. Soc.*, **69**, 278-295.

Smith, P. L., D. J. Musil, A. G. Detwiler and R. Ramachandran, 1999: Observations of mixed-phase precipitation within a CaPE thunderstorm. *J. Appl. Meteor.*, **38**, 145–155.

Steiner, M., R. A. Houze and S. E. Yuter, 1995: Climatological characteristics of three-dimensional storm structure from operational radar and raingauge data. *J. Appl. Meteor.*, 34, 1978-2007.

Stith, J. L., J. E. Dye, A. Bansemer, A. J. Heymsfield, C. A. Grainger, W. A. Petersen and R. Cifelli, 2001: Microphysical Observations of Tropical Clouds. *J. Appl. Meteor.*, In press.

Tao, W. –K., S. Lang, J. Simpson and R. Adler, 1993a: Retrieval algorithms for estimating the vertical profiles of latent heat release: Their applications for TRMM. *J. Meteor. Soc. Jap.*, **71**, 685-700.

Tao, W. –K. and J. Simpson, 1993: Goddard Cumulus Ensemble Model. Part I: Model description. Terr. Atmos. Oceanic Sci., **4**, 35-72.

Tao, W. –K., J. Simpson, C. H. Sui, B. Ferrier, S. Lang, J. Scala, M.D. Chou and K. Pickering, 1993b: Heating, moisture, and water budgets of tropical and middle latitiude squall lines: Comparisons and sensitivity to longwave radiation. *J. Atmos. Sci.*, **50**, 673-690.

Tong, H., V. Chandrasekar, K. R. Knupp and J. Stalker, 1998: Multiparameter radar observations of time evolution of convective storms: Evaluation of water budgets and latent heating rates, *J. Atmos. and Oceanic Tech.*, **15**, 1097-1109.

Ulbrich, C. W., 1983: Natural variations in the analytical form of the raindrop size distribution. *J. Appl. Meteor.*, **22**, 1764–1775.

Wallace, J. M. and P. V. Hobbs, 1977: Atmospheric Science: An Introductory Survey. Academic Press, 467 pp.

Webster, P. J. and R. A. Houze, Jr., 1991: The Equatorial Mesoscale Experiment (EMEX): An overview. *Bull. Amer. Met. Soc.*, **72**, 1481–1506.

Weisman, M. L. and J. B. Klemp, 1982: The dependence of numerically simulated convective storms on vertical wind shear and buoyancy. *Mon. Wea. Rev.*, **110**, 504-520.

Williams, E. R., S. A. Rutledge, S. G. Geotis, N. Renno, E. Rasmussen and T. Rickenbach, 1992: A radar and electrical study of tropical "hot towers". *J. Atmos. Sci.*, **49,** 1386–1396.

Zrnić, D. S., V. N. Bringi, N. Balakrishnan, K. Aydin, V. Chandrasekar and J. Hubbert, 1993: Polarimetric measurements in a severe hailstorm. *Mon. Wea. Rev.*, **121**, 2223- 2238.